

# Synthesis and Characterization of Magnetic Iron Oxide Nanoparticles

by

**Nkanyiso Linda Ndlovu**

*Dissertation submitted in partial-fulfilment of the  
academic requirements for the degree of  
Master of Physics in the  
School of Chemistry and Physics,  
University of KwaZulu-Natal.*

Department of Physics  
University of KwaZulu-Natal  
Private Bag X111, Scottsville 4000, South Africa.

Supervisor: Dr CJ Masina

**2022**



# Abstract

Three high-purity cubic spinel-type crystalline magnetic iron oxides i.e.  $\text{Fe}_3\text{O}_4$ ,  $\text{CoFe}_2\text{O}_4$ , and  $\text{NiFe}_2\text{O}_4$  nanoparticles were successfully synthesized by co-precipitation method. X-ray diffraction (XRD) showed the formation of stoichiometric phases with average particle size of 11.7 nm, 23.6 nm, and 16.4 nm for the as-prepared  $\text{Fe}_3\text{O}_4$ ,  $\text{CoFe}_2\text{O}_4$ , and  $\text{NiFe}_2\text{O}_4$  nanoparticles, respectively. Transmission electron microscopy (TEM) observation for all three samples revealed spherical morphology with single magnetic domain structure. From high resolution TEM (HR-TEM) imaging, lattice fringes with  $d$ -spacing of 0.473 nm and 0.248 nm corresponding to (111) and (311) reflections planes, were observed for both the Co-doped and Ni-doped samples. Energy-dispersive x-ray spectroscopy (EDX) analysis showed the presence and homogeneous distribution of main elements Fe, O, Co, and Ni in the samples. Quantitative EDX results confirmed the formation of stoichiometric  $\text{CoFe}_2\text{O}_4$  and  $\text{NiFe}_2\text{O}_4$  phases with the experimentally measured weight wt% of the samples closely equal to the theoretical calculated wt% values i.e. Fe = 46.35 wt%, O = 26.79 wt%, and Co = 26.87 wt% for  $\text{CoFe}_2\text{O}_4$ , and Fe = 47.02 wt%, O = 27.27 wt%, and Ni = 24.75 wt% for  $\text{NiFe}_2\text{O}_4$ .

The magnetic properties of these nanoparticles were investigated by 57-Fe Mössbauer spectroscopy (MS) and Vibrating Sample Magnetometer (VSM) techniques. Room temperature MS spectrum for the pure  $\text{Fe}_3\text{O}_4$  phase consist of two superimposed sextets with isomer shifts (0.321, 0.463) mm/s and hyperfine field (57.3, 43.4) T attributed to tetrahedral (A-sites) and octahedral (B-sites). The  $\text{CoFe}_2\text{O}_4$  and  $\text{NiFe}_2\text{O}_4$  samples both showed room temperature MS spectra consisting of two sextets and a single central paramagnetic doublet. The two sextets in each sample had almost equal isomer shifts for both A- and B-sites i.e. 0.2956 & 0.3247 mm/s and 0.3784 & 0.2761 mm/s for each of the sites of the  $\text{CoFe}_2\text{O}_4$  and  $\text{NiFe}_2\text{O}_4$  sample, respectively. The paramagnetic doublet was fitted with isomer shift of 0.3272 mm/s for the  $\text{CoFe}_2\text{O}_4$  sample and 0.3249 mm/s for the  $\text{NiFe}_2\text{O}_4$  sample.

Temperature dependence M-T magnetization curves measured at  $H = 500$  Oe in the zero-field-cooled (ZFC) and field-cooled (FC) conditions showed the superparamagnetic nature of all three particles. The  $M_{ZFC}$  magnetization curve showed a maximum (cusp) at 225 K, 300 K, and 228 K corresponding to blocking temperature ( $T_B$ ), for  $\text{Fe}_3\text{O}_4$ ,  $\text{CoFe}_2\text{O}_4$ , and  $\text{NiFe}_2\text{O}_4$ , respectively. For the  $\text{CoFe}_2\text{O}_4$  sample the irreversibility temperature ( $T_{irr}$ ) was equal to the blocking temperature ( $T_B$ ). While measured  $T_{irr}$  for  $\text{Fe}_3\text{O}_4$  and  $\text{NiFe}_2\text{O}_4$  was  $\sim 300$  K for both samples.

The M-H magnetization curves at 300 K for all three samples revealed the coexistence of ferrimagnetic and superparamagnetic behaviour of the nanoparticles. At 300 K all three samples exhibit symmetrical and almost "closed" hysteresis loops with coercivity approximately 36, 70, and 117 Oe and remanence magnetization of approximately 5, 3, and 4 emu/g, for  $\text{Fe}_3\text{O}_4$ ,  $\text{NiFe}_2\text{O}_4$ , and  $\text{CoFe}_2\text{O}_4$ , respectively. Furthermore, M-H measurements at 300 K showed a high saturation magnetization of 89 emu/g for the  $\text{Fe}_3\text{O}_4$  sample compared to 37 emu/g and 26 emu/g for the  $\text{CoFe}_2\text{O}_4$ , and  $\text{NiFe}_2\text{O}_4$ , respectively.

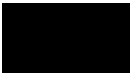
M-H measurements recorded at low temperatures showed rather "opened" hysteresis loops compared to loops measured at 300 K. In contrast to saturated magnetization M-H curves for the  $\text{Fe}_3\text{O}_4$  and  $\text{NiFe}_2\text{O}_4$  nanoparticles, unsaturated M-H loops were observed for  $\text{CoFe}_2\text{O}_4$  sample in the temperature range 10 - 100 K. A significant increase in coercivity to 102 Oe, 391 Oe, and 2.4 kOe was observed for  $\text{Fe}_3\text{O}_4$ ,  $\text{NiFe}_2\text{O}_4$ , and  $\text{CoFe}_2\text{O}_4$ , respectively, when the temperature was reduced from 300 K to 10 K. For the  $\text{CoFe}_2\text{O}_4$  sample, a highest coercivity of  $\sim 2.7$  kOe was measured at 100 K. And finally, M-H data at 10 K showed high saturation magnetization of 100 emu/g, 51 emu/g, and 31 emu/g, for the pure magnetite,  $\text{CoFe}_2\text{O}_4$ , and  $\text{NiFe}_2\text{O}_4$  samples, respectively.



# Declaration

I, Nkanyiso Linda Ndlovu, declare that

1. The research reported in this thesis, except where otherwise indicated, is my original research.
2. This thesis has not been submitted for any degree or examination at any other university.
3. This thesis does not contain other persons' data, pictures, graphs or other information, unless specifically acknowledged as being sourced from other persons.
4. This thesis does not contain any other persons' writing, unless specifically acknowledged as being sourced from other researchers. Where other written sources have been quoted, then:
  - (a) their words have been rewritten but the general information attributed to them has been referenced;
  - (b) where their exact words have been used, their writing has been placed inside quotation marks, and referenced.
5. Where I have reproduced a publication of which I am author, co-author or editor, I have indicated in detail which part of the publication was actually written by myself alone and have fully referenced such publications.
6. This thesis does not contain text, graphics or tables copied and pasted from the internet, unless specifically acknowledged, and the source being detailed in the thesis and in the References sections.

Signed by Student...  ..... and Supervisor.....  .....

# Contents

<b>1</b>	<b>Introduction</b>	<b>1</b>
<b>2</b>	<b>Magnetism in Magnetic Materials</b>	<b>3</b>
2.1	The origin of Magnetism . . . . .	3
2.1.1	Magnetization . . . . .	5
2.1.2	The Curie Law . . . . .	5
2.2	Magnetic Order in Solids . . . . .	6
2.2.1	Ferromagnetism . . . . .	6
2.2.2	Antiferromagnetism . . . . .	7
2.2.3	Ferrimagnetism . . . . .	9
2.2.4	Superparamagnetism . . . . .	9
<b>3</b>	<b>Ferrites Structure and Their Properties</b>	<b>12</b>
3.1	Introduction . . . . .	12
3.2	Magnetite ( $\text{Fe}_3\text{O}_4$ ) nanoparticles . . . . .	12
3.3	Cobalt-Ferrites ( $\text{CoFe}_2\text{O}_4$ ) nanoparticles . . . . .	16
3.4	Nickel-Ferrites ( $\text{NiFe}_2\text{O}_4$ ) nanoparticles . . . . .	19
<b>4</b>	<b>Methodology</b>	<b>22</b>
4.1	Introduction . . . . .	22
4.2	Experimental Techniques . . . . .	22
4.2.1	X-Ray Diffraction . . . . .	22
4.2.2	Transmission Electron Microscope . . . . .	24
4.2.3	Mössbauer Spectroscopy . . . . .	27
4.2.4	Quadrupole Hyperfine Splitting (QS) . . . . .	30
4.2.5	Mössbauer Experimental Set-up . . . . .	31
4.2.6	Vibrating-Sample Magnetometer . . . . .	33
4.3	Experimental Procedure . . . . .	34
4.3.1	Materials Synthesis . . . . .	34
4.3.2	Characterization . . . . .	35
<b>5</b>	<b>Results and Discussion</b>	<b>37</b>
5.1	Magnetite Nanoparticles . . . . .	37
5.1.1	X-ray Diffraction . . . . .	37
5.1.2	Transmission Electron Microscope . . . . .	39
5.1.3	Mössbauer Spectroscopy . . . . .	41
5.1.4	Vibrating-Sample Magnetometer . . . . .	42

5.2	Cobalt-ferrite Nanoparticles . . . . .	46
5.2.1	X-ray Diffraction . . . . .	46
5.2.2	Transmission Electron Microscope . . . . .	47
5.2.3	Mössbauer Spectroscopy . . . . .	53
5.2.4	Vibrating Sample Magnetometer . . . . .	54
5.3	Nickel-ferrite Nanoparticles . . . . .	58
5.3.1	X-ray Diffraction . . . . .	58
5.3.2	Transmission Electron Microscope . . . . .	59
5.3.3	Mössbauer Spectroscopy . . . . .	65
5.3.4	Vibrating Sample Magnetometer . . . . .	66
6	General Conclusion & Recommendations	70
	Bibliography	73

# List of Figures

2.1	Schematic representation of the unpaired electron around the nucleus. (a) orbital motion, and (b) spin motion . . . . .	3
2.2	Temperature dependence of the magnetic susceptibility for (a) paramagnetic and (b) ferromagnetic . . . . .	6
2.3	Types of magnetic ordering in solids (a) Paramagnetism, (b) Ferromagnetism, (c) Anti-ferromagnetism, and (d) Ferrimagnetism . . . . .	7
2.4	$2p$ orbital of oxygen ion overlapping orbitals of metal ions $M_1$ and $M_2$ in a super-exchange interaction . . . . .	8
2.5	Schematic showing super-exchange interaction (a) high energy state and (b) high energy state . . . . .	9
2.6	Transition from multi-domain and to single-domain structure for nanoparticles . . . . .	10
2.7	Schematic showing thermal fluctuations in superparamagnetic nanoparticles . . . . .	11
3.1	Crystal structure of magnetite . . . . .	13
3.2	Magnetite XRD pattern . . . . .	13
3.3	Diagram showing spin arrangement in magnetite . . . . .	14
3.4	$M$ - $H$ magnetization curves for magnetite at 4 K and 295 K . . . . .	15
3.5	Crystal structures of cobalt-ferrite nanoparticles . . . . .	16
3.6	Powder X-ray diffraction pattern for $\text{CoFe}_2\text{O}_4$ nanoparticles . . . . .	17
3.7	$M$ - $H$ hysteresis curves for a cobalt-ferrite nanoparticles recorded at 10 K and 300 K . . . . .	18
3.8	Inverse spinel cubic structure for Ni-doped ferrite . . . . .	19
3.9	X-ray diffraction pattern of nickel-ferrite . . . . .	20
3.10	$M$ - $H$ hysteresis loops of Ni-doped ferrite measured at 77 K and 300 K . . . . .	21
4.1	Image of a Bruker Advance D8 X-ray diffractometer . . . . .	23
4.2	Schematic diagram illustrating Bragg's law . . . . .	23
4.3	A diagram showing the internal structure of a transmission electron microscope . . . . .	25
4.4	Bright-field (A) and Dark-field image formation in a TEM . . . . .	26
4.5	Diagram showing the creation of characteristic x-rays (a) and EDS spectrum (b) . . . . .	27
4.6	Diagram showing emission spectrum (brown) and absorption spectrum (red) of $\gamma$ -ray process . . . . .	28
4.7	Schematic representation of the isomer shift ( $\delta$ ) . . . . .	29

4.8	Schematic representation of quadrupole splitting . . . . .	30
4.9	Energy levels transition to show a sextet hyperfine splitting of an MS spectra . . . . .	31
4.10	Schematic of the apparatus used in a Mössbauer spectroscopy (ref. Dyar). . . . .	32
4.11	Schematic showing the recording of a Mössbauer spectrum using Doppler effect: emission spectrum (brown), absorption spectrum (red), and transmitted spectrum (blue) . . . . .	32
4.12	(a)System diagram of a Vibrating Sample Magnetometer. (b) External close up view of the alignment sample with the magnetic field . . . . .	33
4.13	Schematic assembly of experimental synthesis in the laboratory . . . . .	34
4.14	Synthesized powdered samples (a) Magnetite, (b) Cobalt-ferrite, and (c) Nickel-ferrite . . . . .	35
5.1	XRD pattern of a powdered $\text{Fe}_3\text{O}_4$ sample . . . . .	37
5.2	Williamson-Hall plot for Magnetite nanoparticles for mean crystallite size and micro-strain determination. . . . .	38
5.3	(a) Magnetite nanoparticles from TEM and (b) the mean diameter distribution. . . . .	40
5.4	$\text{Fe}_3\text{O}_4$ nanoparticles MS spectrum at room temperature. . . . .	41
5.5	ZFC/FC magnetization curves measured in an applied field $H = 500$ Oe for $\text{Fe}_3\text{O}_4$ nanoparticles. . . . .	43
5.6	Hysteresis loops measured at 10 K - 300 K for $\text{Fe}_3\text{O}_4$ nanoparticles. . . . .	44
5.7	Derivatives of the respective ascending (blue arrow) and descending (red arrow) branches for negative fields for the $\text{Fe}_3\text{O}_4$ ( $M-H$ ) curves measured at 10 K - 300 K. . . . .	45
5.8	XRD pattern of a $\text{CoFe}_2\text{O}_4$ powdered sample. . . . .	46
5.9	(W-H) plot of the $\text{CoFe}_2\text{O}_4$ sample. . . . .	47
5.10	(a) $\text{CoFe}_2\text{O}_4$ TEM nanoparticles and (b) mean diameter distribution. . . . .	48
5.11	Bright field $\text{CoFe}_2\text{O}_4$ TEM images with inset, showing the SAED. . . . .	49
5.12	(a) HR-TEM micrograph of cobalt-ferrite nanoparticles showing lattice fringes, (b) enlarged image of the lattice fringes marked with a red rectangle, (c) re-constructed lattice fringes from (b), and (d) profile of the lattice fringes in (c). . . . .	50
5.13	EDX spectrum of the $\text{CoFe}_2\text{O}_4$ sample. . . . .	51
5.14	Surface elemental mapping for $\text{CoFe}_2\text{O}_4$ nanoparticles. (a) STEM image, (b) elemental map showing distribution of all the elements in the specimen, (c)-(e) individual elemental maps for Fe, Co, and O, respectively. . . . .	52
5.15	Mössbauer spectrum of the $\text{CoFe}_2\text{O}_4$ sample recorded at room temperature. . . . .	53
5.16	Magnetization FC and ZFC curves as function of temperature in an applied field ( $H$ ) for $\text{CoFe}_2\text{O}_4$ nanoparticles. . . . .	54
5.17	$\text{CoFe}_2\text{O}_4$ hysteresis loop, showing the behaviour of magnetization and coercivity at lower and higher temperatures (10 - 300)K . . . . .	56

5.18	Derivatives of the respective descending and ascending branches for negative fields for the $\text{CoFe}_2\text{O}_4$ $M$ - $H$ curves at 10 K - 300 K. . . . .	57
5.19	XRD pattern of $\text{NiFe}_2\text{O}_4$ nanoparticles. . . . .	58
5.20	Williamson-Hall plot for the $\text{NiFe}_2\text{O}_4$ nanoparticles. . . . .	59
5.21	(a) Bright field TEM image of $\text{NiFe}_2\text{O}_4$ nanoparticles, (b) Histogram of particle size distribution. . . . .	60
5.22	Bright field TEM image and indexed SAED pattern (inset) of the $\text{NiFe}_2\text{O}_4$ sample. . . . .	61
5.23	(a) HR-TEM micrograph of $\text{NiFe}_2\text{O}_4$ nanoparticles, (b) enlarged image of the lattice fringes marked with a red rectangle in (a), (c) inverse FFT, and (d) profile plot of the inverse FFT. . . . .	62
5.24	EDX spectrum of the $\text{NiFe}_2\text{O}_4$ sample for elemental composition analysis. . . . .	63
5.25	STEM image and EDX maps for the $\text{NiFe}_2\text{O}_4$ nanoparticles. . . . .	64
5.26	MS spectrum of the $\text{NiFe}_2\text{O}_4$ nanoparticles recorded at room temperature. . . . .	65
5.27	FC and ZFC magnetization curves as a function of temperature in an applied field ( $H$ ) for $\text{NiFe}_2\text{O}_4$ nanoparticles. . . . .	67
5.28	$\text{NiFe}_2\text{O}_4$ hysteresis loop showing the magnetization and coercivity behaviour at low and high temperatures (10 - 300)K . . . . .	68
5.29	Derivatives of the respective descending and ascending branches for negative fields for the $\text{NiFe}_2\text{O}_4$ $M$ - $H$ curves at 10 K - 300 K. . . . .	69

# List of Tables

5.1	Mössbauer parameters obtained from the fit of the $\text{Fe}_3\text{O}_4$ MS spectrum.	42
5.2	The hysteresis loop data for $\text{Fe}_3\text{O}_4$ nanoparticles. . . . .	45
5.3	The EDX data for $\text{CoFe}_2\text{O}_4$ nanoparticles. . . . .	52
5.4	Room temperature Mössbauer hyperfine parameters of the $\text{CoFe}_2\text{O}_4$ sample. . . . .	54
5.5	The hysteresis loop data for $\text{CoFe}_2\text{O}_4$ nanoparticles. . . . .	57
5.6	The EDX data for $\text{NiFe}_2\text{O}_4$ nanoparticles. . . . .	64
5.7	Room temperature Mössbauer hyperfine parameters of the $\text{NiFe}_2\text{O}_4$ sample. . . . .	66
5.8	The hysteresis loop data for $\text{NiFe}_2\text{O}_4$ nanoparticles. . . . .	69

# Acknowledgements

The satisfaction and euphoria that accompany the successful completion of any task would be incomplete without the mention of the people, who made it possible, and whose constant guidance and encouragement aided in completing the master's dissertation.

I consider it a privilege to express gratitude and respect to all those who guided and inspired me throughout the course. I thank Dr. CJ Masina in the Physics Dept. under the school of Chemistry and Physics of the college Agriculture, Engineering and Science for his guidance and invaluable feedback on my analysis and framing. At times responding to emails at night and early in the morning, his patience with all the trials and tribulations we encountered as seatbacks for the past two years. His contribution will not go unnoticed and unappreciated, as it formed part of the reasons behind the completion of this dissert. It has been a great honor being under his supervision.

I would like to express my gratitude to the National Research Foundation (NRF) for their continued financial award support to keep myself clean and prepared for what comes my way academically and personally.

Also, thank Dr. Remy Bucher and Dr. Zakhele Khumalo from iThemba LABS for their relentless efforts in ensuring the numerous samples they received. I got all the XRD data quantifications possible. Prof Daniel Wamwangi and Prof Deena Naidoo from the University of the Witwatersrand for the magnetic measurements.

The Microscopy and Microanalysis Unit staff members, especially Miss Cynthia N. Matyumza at UKZN, for her support and exposure to the quantification techniques of HR-TEM and SEM measurements, I gained much practical experience under her guidance and personal life advice.

To the chemistry department (PMB), I would like to extend my appreciation for their patience and support with synthesis types of equipment. To Miss PN Mjwara, I thank you for your devoted time in ensuring I completed the experimental and other parts of the dissertation.

To the physics department (PMB), I am forever indebted to the staff and colleagues who have been an inspiration throughout this journey. To the in-house office members, Miss L. Ngwane, Mr. N Memela, Mr. N Jili, Mr. L Bahige, and my co-supervisee colleague Mr. A Chithwayo, you have paved a path for me full of options to carve my path and have been there to assist and show me some of the crucial things I needed to be aware of, for that, and more y'all are highly appreciated.

I thank my family for being there through my highs and lows; without the motivation and late-night tearful calls of encouragement, your role did not go unnoticed.

Last but not least, I thank myself for the resilience I grew with every day to get



through all the tough times I encountered in completing the dissertation. Everything set out has a conclusion, but it depends on how and when you want it to be.

# Chapter 1

## Introduction

Recently[1, 2], there has been great scientific interest in the preparation and the study of magnetic nanoparticles due to their unique magnetic properties. More interestingly, is the change of the magnetic structure from multi-domain to single-domain when decreasing the size of these magnetic particles. If the size of the single-domain particles is sufficiently small, these magnetic nanoparticles exhibit a unique magnetic property called superparamagnetism i.e. the random fluctuation of magnetic moment in the domain due to thermal agitation [2–4]. Superparamagnetism is a consequence of particle size in magnetic nanoparticles, and this demonstrate that magnetic properties are not only related to the composition of nanomaterials but are also particle size-dependent.

Amongst these mostly studied magnetic nanoparticles are the spinel-type ferrites. They have wide range of applications such as magnetic data storage, magnetic fluids, and magnetic separation [5]. Furthermore, superparamagnetic ferrite nanoparticles are unique as they are able to induce heat under the application of an alternating magnetic field, and so magnetic nanoparticles may be applied in various application of interest, e.g. drug delivery, targeting magnetic hyperthermia, magnetic resonance imaging, and thermochemotherapy [5–7]. Many ferrites adopt the spinel structure with formula  $(AB_2O_4)$  where (A) and (B) represents divalent cations in tetrahedral sites and trivalent cations in octahedral, respectively. However,  $Fe_3O_4$  based ferrites adopt the inverse spinel structure  $((B)^{tet}(AB)^{oct}O_4)$ , where the divalent ions swap with half of the trivalent ions. In this structure  $\frac{1}{8}^{th}$  tetrahedral holes are occupied by (B) cations,  $\frac{1}{4}^{th}$  of the octahedral sites are occupied by the (A) cations, and the other  $\frac{1}{4}^{th}$  are occupied by (B) cations [8, 9].

Interest in the ferrite nanoparticles currently focuses on control of their magnetic properties. The magnetic properties of  $Fe_3O_4$  based ferrites can therefore be tuned by partially replacing the divalent  $Fe^{2+}$  ions with cations like  $Zn^{2+}$ ,  $Mn^{2+}$ ,  $Co^{2+}$ , and  $Ni^{2+}$  [10–12] e.g. cobalt-ferrites ( $CoFe_2O_4$ ) shows a significant increase in coercivity compared to pure magnetite, which is a base requirement for its use in high density recording. Besides its high coercivity, cobalt-ferrites provide improved stability with respect to temperature and stress [13, 14]. The substitution of  $Fe^{2+}$  with either  $Co^{2+}$  or  $Ni^{2+}$  should result in  $Co^{2+}$  or  $Ni^{2+}$  occupying the octahedral sites.

However, the distribution can be altered depending on the synthesis conditions, and this results in a partially-inverted spinel structure for the  $\text{Co}^{2+}$  or  $\text{Ni}^{2+}$  substituted nanoparticles, where the divalent cations are found to be present in both tetrahedral and octahedral sites [15, 16].

The aim of this work was therefore to synthesize and study the effect of nickel and cobalt substitution on the magnetic properties of magnetite nanoparticles. For this reason, three samples were synthesized ( $\text{Fe}_3\text{O}_4$ ,  $\text{CoFe}_2\text{O}_4$ , and  $\text{NiFe}_2\text{O}_4$ ) by coprecipitation method and their structure and magnetic properties were investigated by X-ray diffraction, Transmission electron microscopy, Energy-Dispersive X-ray spectroscopy, Mössbauer Spectroscopy, and Vibrating Sample Magnetometer.

The dissertation is structured into six main chapters: **Chapter 1** is the introduction chapter which gives the aim of the work and introduces the reader to the magnetic ferrites and their applications, **Chapter 2** and **Chapter 3** gives detailed literature review on magnetism, the structure, and magnetic properties of the ferrites, respectively. **Chapter 4** is the methodology chapter which gives synthesis methods and experimental techniques used in this study, **Chapter 5** results and discussion, this is the main chapter that contains the results and analysis on the three samples ( $\text{Fe}_3\text{O}_4$ ,  $\text{CoFe}_2\text{O}_4$ , and  $\text{NiFe}_2\text{O}_4$ ) considered in this project, and finally **Chapter 6** gives the general conclusion and recommendations.

## Chapter 2

# Magnetism in Magnetic Materials

### 2.1 The origin of Magnetism

Magnetism is a phenomenon associated with magnetic field that arise from the motion of electric charges [17]. This chapter discusses the origin of magnetic moments in matter as well as the different types of magnetic order in solids which are based on the arrangements of the magnetic moments.

A free atom's magnetic moment arises from three sources i.e. the electron's orbital motion around the nucleus, spin angular momentum, and the change in the orbital moment induced by an applied magnetic field [18]. Depicted in Figure 2.1 is the orbital (a) and spin motion (b) of an electron in an atom. The orbital moment can be understood using Bohr's model. An electron mass  $m$  moving in an orbit is equivalent to a current in a closed current loop where the current direction is opposite to the sense of circulation [19]. The period it takes the electron of mass  $m$

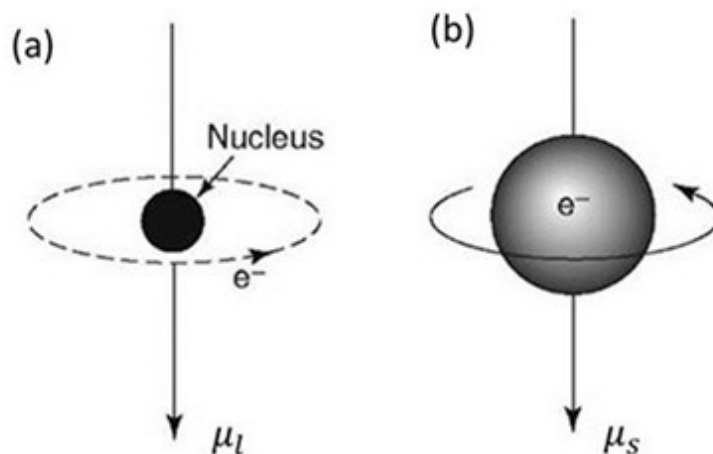


**Figure 2.1:** Schematic representation of the unpaired electron around the nucleus. (a) orbital motion, and (b) spin motion [20].

to make an orbit is given by the equation 2.1.

$$T = \frac{2\pi r}{v} \quad (2.1)$$

Where  $v$  is the velocity of the electron, therefore the current due to motion of the electron during that period is given by;

$$I = \frac{\text{charge}}{\text{period}} = -\frac{ev}{2\pi r}. \quad (2.2)$$

Langevin's theory of diamagnetism and paramagnetism states that this current will produce at a given distance a magnetic field with the same intensity as a permanent magnet with a magnetic moment that can be expressed as;

$$\boldsymbol{\mu}_l = I\mathbf{A} = -\frac{ev}{2\pi r}\pi r^2 = -\frac{1}{2}e(\mathbf{r} \times \mathbf{v}) \quad (2.3)$$

Where  $\mathbf{A}$  is the area vector with a magnitude  $\pi r^2$  [19, 21]. In terms of angular momentum  $\mathbf{l} = m_e \mathbf{r} \times \mathbf{v}$ , the magnetic moment becomes;

$$\boldsymbol{\mu}_\ell = -\frac{e}{2m_e}\ell = g_\ell \mu_B \ell \quad (2.4)$$

Where  $\mu_B = \frac{eh}{4\pi m_e}$  is the Bohr magneton and the intrinsic spin motion of the electron is associated with spin magnetic dipole moment given by;

$$\boldsymbol{\mu}_s = -\frac{e}{m_e}\mathbf{s} = g_s \mu_B \mathbf{s} \quad (2.5)$$

When the electron spin and orbital motion are simultaneously taken into account this results in the total angular momentum of the atom  $J$  given by the spin-orbit coupling  $J = S + L$ . Finally one obtains the magnetic moment of the atom given by [19];

$$\boldsymbol{\mu} = -\mu_B(2\mathbf{S} + \mathbf{L}) = -\mu_B(\mathbf{S} + \mathbf{J}) \quad (2.6)$$

Where  $g_l = 1$ ,  $g_s = 2$ , and the lower case  $s$  and  $l$  has been replaced by upper case  $S$  and  $L$ , according to the Russell-Saunders coupling, the spin momenta couples to form a total spin  $\mathbf{S} = \sum_{i=1}^n \mathbf{s}_i$ , and orbital momenta couple to form  $\mathbf{L} = \sum_{i=1}^n \mathbf{l}_i$  in a many electron atom. The total magnetic moment of the atom can finally be written as;

$$\boldsymbol{\mu}_j = -g\mu_B \mathbf{J}. \quad (2.7)$$

Where  $g$  is known as the Landé factor and may be expressed as;

$$g = 1 + \frac{J(J+1) + S(S+1) - L(L+1)}{2J(J+1)}, \quad (2.8)$$

### 2.1.1 Magnetization

The resultant magnetization in a material is therefore defined as the sum of all magnetic moments per unit volume given by;

$$M = \frac{1}{V} \sum_{i=1}^n \mu_i. \quad (2.9)$$

However, the magnetization of the sample is often reported in terms of the mass  $m$  due to temperature effects on the volume:

$$M = \frac{1}{m} \sum_{i=1}^n \mu_i. \quad (2.10)$$

Finally, the degree of magnetization of a material in response to an external applied magnetic field  $H = B/\mu_0$  is known as the susceptibility defined by [22, 23]

$$\chi = \frac{M}{H} \quad (2.11)$$

where  $B$  is the magnetic flux density,  $B$  established within the material, and  $\mu_0$  is the permeability of free space. It is well known that magnetic response to an applied field of materials which do not order magnetically may be either paramagnetic ( $\chi > 0$ ) or diamagnetic ( $\chi < 0$ ). Diamagnetism is observed in materials containing no atomic magnetic moments i.e. in atoms where all the orbital shells are filled and there are no unpaired electrons [24, 25]. While paramagnetism occurs in materials which possess a permanent magnetic moment. In the absence of an external applied magnetic field, magnetic moments in paramagnetic materials are randomly oriented and there is no net spontaneous magnetisation (see Figure 2.3). If a field is applied a torque is induced to the magnetic moments which aligns them in the same direction to the field [26].

### 2.1.2 The Curie Law

Ferro- and ferri magnetic materials are known to undergo a magnetic transition to paramagnetic state above a certain temperature called Curie temperature,  $T_C$ . This is a temperature named after the French physicist Pierre Curie, who in 1895 discovered the laws that relate some magnetic properties to change around the temperature  $T_C$  [27]. According to Curie's law for paramagnets the magnetic susceptibility of a paramagnet is inversely proportional to the absolute temperature [19].

$$\chi = \frac{C}{T} \quad (2.12)$$

where  $C$  is known as the Curie constant. On the other hand, ferromagnets possess spontaneous magnetisation in the absence of an external field below  $T_C$ . Taking into account the presence of the molecular field ( $\lambda M$ ) responsible for aligning the moments in the absence of an applied field in ferromagnets, the total field becomes:

$$H_t = H + \lambda M \quad (2.13)$$

If  $H_t$  is substituted in equation 2.12 for paramagnets we obtain

$$M = \frac{C(H + \lambda M)}{T} \quad (2.14)$$

which can be re-arranged to obtain the more general Curie-Weiss law for ferromagnets above  $T_C$  [19, 28]:

$$\chi = \frac{C}{T - T_C} \quad (2.15)$$

where  $T_C = \lambda C$ . Figure 2.2 shows temperature dependence of the magnetic susceptibility for paramagnets and ferromagnets. The Curie temperature  $T_C$  indicates the point at which ferromagnetic material are considered to exhibit a paramagnetic behaviour. It can be clearly seen that the susceptibility of ferromagnets is similar to that of paramagnets above  $T_C$ . It is observed that the susceptibility (Fig. 2.2 (b)) diverges as  $T \rightarrow T_C$ .

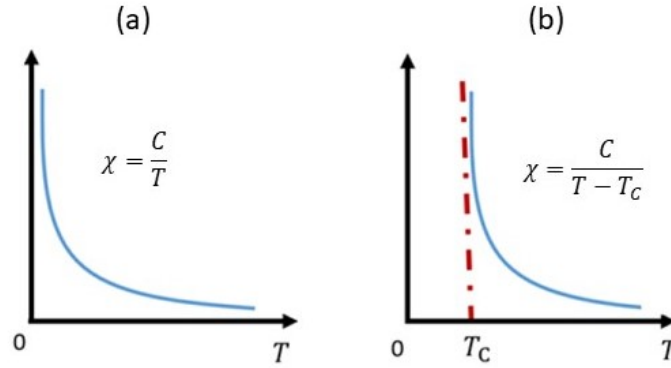


**Figure 2.2:** Temperature dependence of the magnetic susceptibility for (a) paramagnetic and (b) ferromagnetic [28].

## 2.2 Magnetic Order in Solids

In section 2.1.1 it was discussed that some materials do not have any order of magnetic moments, hence orientation of magnetic moments are random [29, 30]. Thus, no spontaneous magnetization appear, these are known to be paramagnetic materials. In this section, materials with ordered magnetic moments are discussed, these include ferromagnetism, antiferromagnetism, ferrimagnetism and superparamagnetism. Figure 2.3 shows the magnetic ordering of (a) paramagnetic, (b) ferromagnetic, (c) anti-ferromagnetic, and (d) ferrimagnetic materials in the absence of an external applied field.

### 2.2.1 Ferromagnetism

Ferromagnetic materials have ordered magnetic moments and the molecular field is responsible for the strong interactions results to ordering of the moments. A

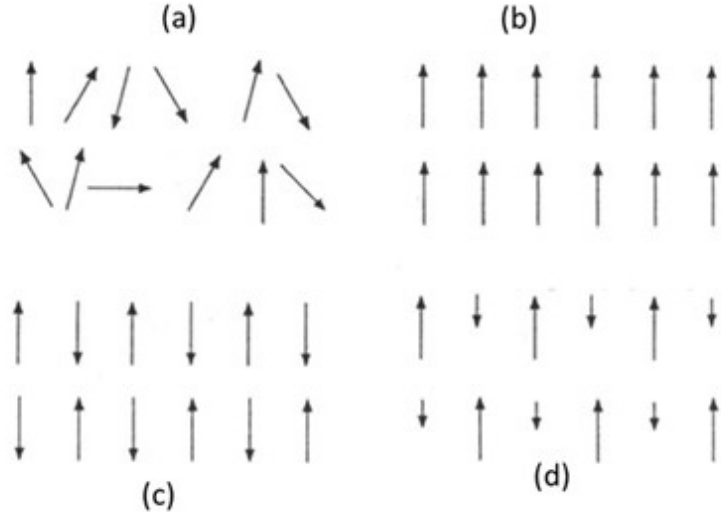


**Figure 2.3:** Types of magnetic ordering in solids (a) Paramagnetism, (b) Ferromagnetism, (c) Anti-ferromagnetism, and (d) Ferrimagnetism [26, 31].

strong interaction between magnetic moments aligns the moments when the material experiences an intense internal magnetic field known as molecular field that is proportional to the magnetization of the ferromagnet. The field is expressed as:

$$H^i = \lambda M \quad (2.16)$$

where  $\lambda$  is known as the molecular field coefficient. The physical origin of the molecular field in eq. 2.16 is exchange interaction which originates from the electrostatic Coulomb repulsion, overlap of the wave functions and the Pauli exclusion principle. Therefore, the wave functions of nearest neighbour magnetic moments overlap and interact through **direct** exchange interaction. The short-range interaction between two electrons with spins  $\vec{S}_1$  and  $\vec{S}_2$  is expressed by the Heisenberg Hamiltonian given by [32]

$$\mathcal{H}_{Heis} = \mathcal{J}_{ij} \vec{S}_1 \cdot \vec{S}_2 \quad (2.17)$$

where  $\mathcal{J}_{ij}$  is an exchange integral.  $\mathcal{J}_{ij}$  is positive for parallel spin arrangement (ferromagnetic ordering) and is negative for antiparallel spin arrangement (antiferromagnetic ordering). Since the exchange interaction is short-range, the value of  $\mathcal{J}_{ij}$  is largest for magnetic moments that are so close to each other [33]. Exchange interaction between magnetic moments aligns the magnetic moments, materials with magnetic moments which are in a parallel alignment are known as ferromagnetic materials (see Fig. 2.3 (b)).

### 2.2.2 Antiferromagnetism

If the magnetic moments align in an antiparallel orientation, this is known as antiferromagnetic behaviour as demonstrated in Figure 2.3 (c). The overall magnetization



for anti-ferromagnets is zero and  $\mathcal{J}_{ij}$  is negative for this magnetic spin configuration. Anti-ferromagnets have a critical temperature called Néel temperature,  $T_N$ , above which they become paramagnetic [30, 34, 35]. Anti-ferromagnetism materials crystal lattice is subdivided into two atomic sublattices (A and B) which order in such a way that their net magnetization is zero. The molecular field acting on each sublattice spins is given by

$$\begin{aligned} H_A^i &= \lambda_{AA}M_A + \lambda_{AB}M_B + H \\ H_B^i &= \lambda_{BA}M_A + \lambda_{BB}M_B + H \end{aligned} \quad (2.18)$$

where  $\lambda_{AB} = \lambda_{BA}$  is the inter-sublattice coupling,  $\lambda_{AA} = \lambda_{BB}$  is the intra-sublattice coupling and  $M_A = -M_B$  [19].

Sometimes direct exchange interaction between magnetic ions is weakened by the presence of non-magnetic interstitial ions. In this case, indirect interaction of magnetic moments occurs through an intermediary in a process called **super-exchange** interaction [33]. Figure 2.4 shows super-exchange interaction between  $M_1$  and  $M_2$  through oxygen ions in an anti-ferromagnetically ordered MnO oxide.

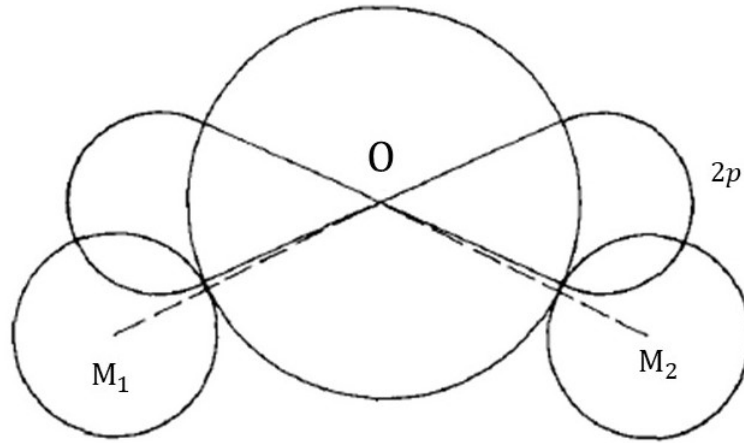


**Figure 2.4:**  $2p$  orbital of oxygen ion overlapping orbitals of metal ions  $M_1$  and  $M_2$  in a super-exchange interaction [33].

Figure 2.5 further illustrates the super-exchange interaction in MnO showing the rotation of an electron on the  $M_1$  ion to be antiparallel to the other electron on the  $M_2$  ion. Initially, the two electrons on  $M_1$  and  $M_2$  are parallel to each other. Then the oxygen bridge transmit a super-exchange interaction which flips the electron on  $M_1$  to be antiparallel to the electron on  $M_2$  resulting in an anti-ferromagnetic arrangement [19, 33]. Therefore, super-exchange interaction can be used to explain the antiparallel spin configuration in both ferrimagnetic and anti-ferromagnetic materials. Ferrites, which is a subject of the current investigation, are ferrimagnetically ordered and the super-exchange interactions between neighbouring magnetic moments take place through the oxygen ions.

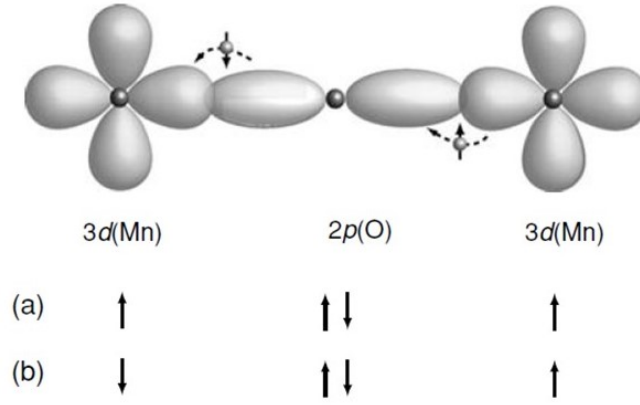


**Figure 2.5:** Schematic showing super-exchange interaction (a) high energy state and (b) high energy state [19].

### 2.2.3 Ferrimagnetism

In a case of two antiparallel aligned dipole moments on two sublattices (A and B) that have unequal magnitudes, a net non-zero magnetization is produced, and such materials are known as ferrimagnetic. The magnetic ordering in ferrimagnets is illustrated in Figure 2.3 (d). The most famous ferrimagnet is magnetite, which is the subject of the present investigation. The total field on each sublattice is similar to the one for anti-ferromagnetic materials with  $\lambda_{AA} \neq \lambda_{BB}$  and  $M_A \neq M_B$  [19].

$$\begin{aligned} H_A^i &= \lambda_{AA}M_A + \lambda_{AB}M_B + H \\ H_B^i &= \lambda_{BA}M_A + \lambda_{BB}M_B + H \end{aligned} \quad (2.19)$$

### 2.2.4 Superparamagnetism

Single-domain ferromagnetic and ferrimagnetic nanoparticles with sufficiently small crystallite size exhibit a unique magnetic property known as superparamagnetism. This magnetic behaviour was made by Néel's theoretical prediction that coercivity approaches zero for sufficiently small nanoparticles as a consequence of spin thermal agitation induced by thermal energy which prevent the existence of a stable magnetization [36]. Superparamagnetic behaviour induces a spontaneous reversal of magnetization i.e. magnetic moments randomly flips direction and the average time to perform such flip is known as the Néel relaxation time given by [37];

$$\tau = \tau_0 \exp\left(\frac{\Delta E}{k_B T}\right) \quad (2.20)$$

where  $\tau_0$  is called the characteristic time,  $T$  is temperature, and  $k_B$  is Boltzmann constant.  $\Delta E$  is the energy barrier between the two orientations which can be expressed as [37]:

$$\Delta E = KV \sin^2 \theta \quad (2.21)$$

where  $V$  is the volume of the nanoparticles,  $K$  is the anisotropy constant, and  $\theta$  is the angle between the magnetic moments and the easy axis. In sufficiently

small nanoparticles, the thermal energy ( $KT$ ) overcomes the barrier energy i.e.  $\Delta E \leq KT$ , and magnetization starts to randomly flip direction under influence of temperature [38].

When the Néel relaxation is smaller than the time scale of the measurement i.e.  $\tau \ll \tau_m$  the magnetization maintains one direction during measurement and therefore the magnetic moments are in an ordered state. However, when  $\tau \gg \tau_m$ , a superparamagnetic state is observed, magnetic moments randomly flips direction [39, 40]. The transition temperature at which  $\tau = \tau_m$  is known as superparamagnetic blocking temperature ( $T_B$ ) given by:

$$T_B = \frac{KV}{k_B \ln\left(\frac{\tau_m}{\tau_0}\right)} \quad (2.22)$$

Superparamagnetism occurs in nanoparticles which are single domain. A domain is a region of a ferromagnetic material in which positive interactions between the magnetic dipole moments favours parallel alignment. Frenkel and Dorfman [41] initially predicted that when the size of ferromagnetic or ferrimagnetic becomes less than a critical size, the amount of energy required to create domain walls outweighs the decrease in magnetostatic energy. Therefore, the formation of a single-domain is preferred. This process is illustrated in Figure 2.6. If the particle size of the nanoparticles is reduced from tens of nanometers to a few nanometers, a change in magnetic structure from multi-domain to single-domain is observed when  $d < d_{SD}$ , where  $d_{SD}$  is a critical diameter. A further reduction in particle size to  $d < d_{SPM}$ , results in superparamagnetic behaviour. The  $M$ - $H$  curves of these nanostructures will show hysteresis ( $d > d_{SPM}$ ) and anhysteretic ( $d < d_{SPM}$ ) behaviour [41].

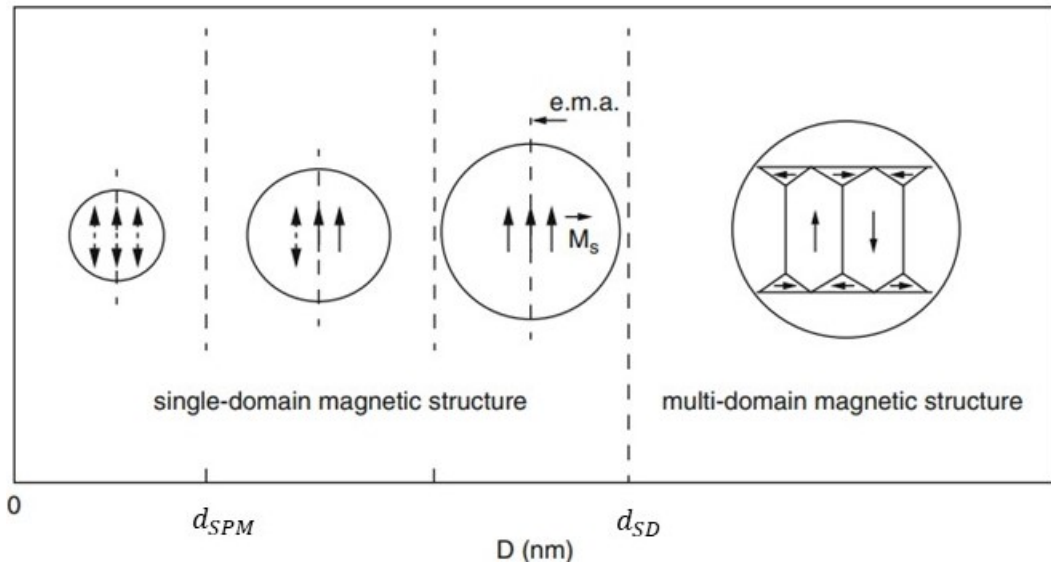


**Figure 2.6:** Transition from multi-domain and to single-domain structure for nanoparticles [41].

In ferro- or ferrimagnetic materials, the spontaneous magnetization has an easy axis, along which the magnetization prefers to lie [33]. Magnetization reversal can occur via rotation of the magnetization from one magnetic easy axis to another. In the case of uni-axial anisotropy the energy barrier takes the general form [42]:

$$\Delta E_a = K_1 V \sin^2 \theta + K_2 V \sin^4 \theta \quad (2.23)$$

where  $K_1$  and  $K_2$  are the magnetic anisotropy constants, and  $\theta$  is the angle between the easy axis. The secondary term is often neglected due to its small contribution [42] and equation 2.23 is similar to equation 2.21.

Figure 2.7 demonstrate the thermal fluctuation of a magnetic moment along the uni-axial easy axis i.e.  $a$ -axis in this case. The magnetic moment flip up and down between the two positions  $\theta = 0^\circ$  and  $180^\circ$  when thermal energy overcomes the anisotropy energy barrier  $\Delta E_a$ . The typical time between the two flips is known as Néel relaxation time given by equation 2.20.

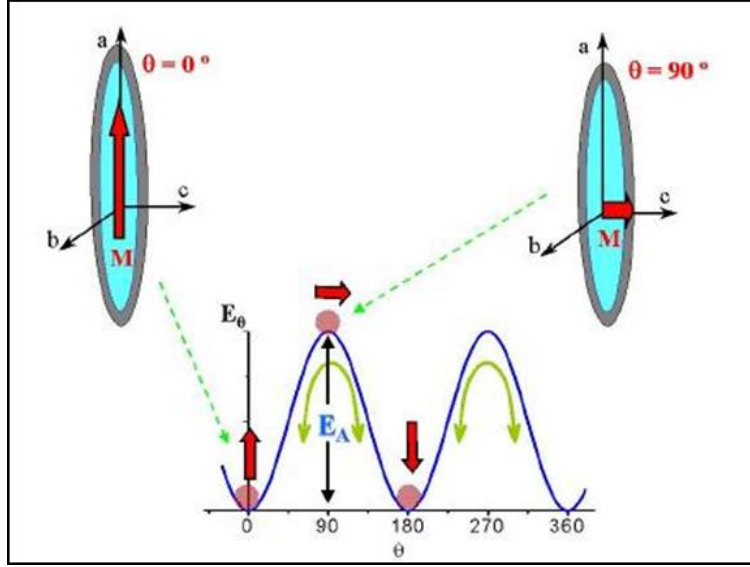


**Figure 2.7:** Schematic showing thermal fluctuations in superparamagnetic nanoparticles [43].

# Chapter 3

## Ferrites Structure and Their Properties

### 3.1 Introduction

Magnetite  $\text{Fe}_3\text{O}_4$  based nanoparticles exhibit unique and tunable fundamental size and shape-dependent magnetic properties. These magnetic nanosized iron oxides are used in various applications in different areas such as ferrofluids [44], magnetic drug delivery, high-density information storage, photo-catalysis, gas sensors, biosensors and magnetic hyperthermia for cancer treatment [45, 46]. Magnetite nanoparticles are preferred in biomedical field, because of their biocompatibility and variable toxicity.

For applications such as biomedical, particle sizes in the superparamagnetic regime is preferred. In superparamagnetic materials, the net magnetization averages to zero once the external field has been removed which reduces particle's magnetic interaction and hence particle's resistance to aggregation is increased [47]. Another important requirement for these magnetic nanoparticles in the biomedical field is high magnetic saturation so that the particles can be controlled with a moderate external magnetic field [47].

Amongst the known iron oxides, magnetite is unique in that it contains both  $\text{Fe}^{2+}$  and  $\text{Fe}^{3+}$  ions and its magnetic properties can be tuned by partly or fully replacing the  $\text{Fe}^{2+}$  ions by other divalent ions ( $\text{Co}^{2+}$ ,  $\text{Ni}^{2+}$ ,  $\text{Mn}^{2+}$ ,  $\text{Zn}^{2+}$ , etc). The substitution of  $\text{Fe}^{2+}$  cations in magnetic iron oxide (i.e magnetite) with cobalt  $\text{Co}^{2+}$  and/or nickel  $\text{Ni}^{2+}$  cations, has significant effect on the magnetic properties of the ferrites [47].

### 3.2 Magnetite ( $\text{Fe}_3\text{O}_4$ ) nanoparticles

#### Crystal Structure

Magnetite is the most common black or dark brown naturally occurring iron oxide with the chemical formula  $\text{Fe}_3\text{O}_4$  [48]. In its bulk state, magnetite has a cubic inverse spinel structure with chemical formula  $(\text{Fe}^{3+})_A[\text{Fe}^{2+}, \text{Fe}^{3+}]_B\text{O}_4$ , and crystal-

lizes in the  $F\bar{d}3m$  space group with a lattice parameter  $a = 8.39 \text{ \AA}$  [49, 50]. The crystal structure of magnetite is shown in Figure 3.1. In the structure, all the  $\text{Fe}^{2+}$  ions occupy octahedral sites and  $\text{Fe}^{3+}$  ions are equally distributed into octahedral and tetrahedral sites [49]. The blue spheres shows  $\text{Fe}^{3+}$  ions in tetrahedral (A-sites) coordination, black spheres represents the  $\text{Fe}^{2+}/\text{Fe}^{3+}$  ions occupying the octahedral (B-sites), and the orange spheres are oxygen  $\text{O}^{2-}$  ions [51, 52].

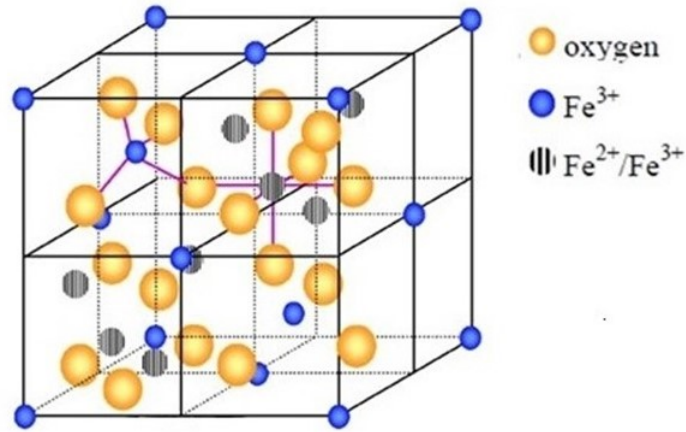


**Figure 3.1:** Crystal structure of magnetite [52].

The phase identification of magnetite can be achieved by conventional X-ray diffraction methods. Figure 3.2, shows a typical XRD pattern for magnetite reported by compeán-Jasso et al. [53] indexed according to the spinel structure with  $F\bar{d}3m$  space group.

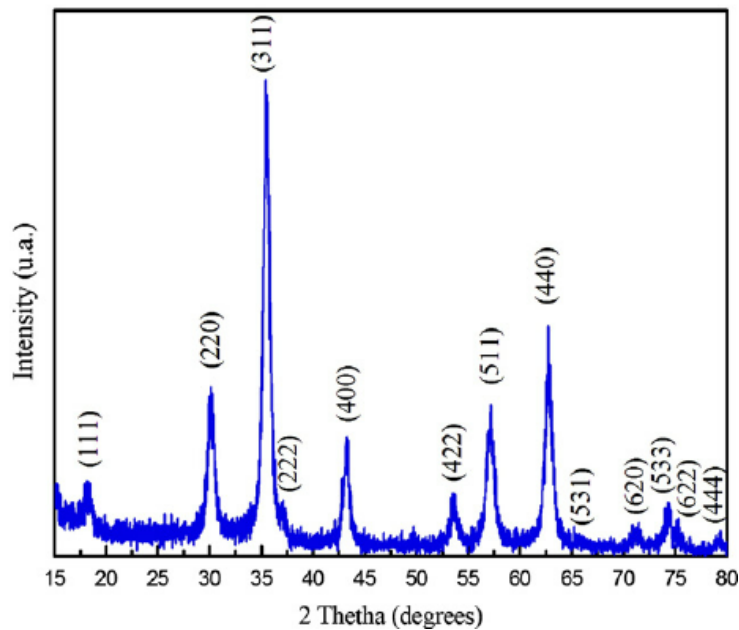


**Figure 3.2:** Magnetite XRD pattern [53].

## Magnetic Properties

Magnetite is ferrimagnetic at room temperature and becomes paramagnetic above  $T_C = 850$  K [54]. The ordering of magnetic moments in ferro-, ferri-, and antiferromagnetic materials decreases with increasing temperature and material become disordered, lose their magnetization above  $T_C$  [55, 56]. In magnetite, the ferrimagnetic behaviour results from super-exchange interaction between the cations in A-sites and B-sites sites which occurs through the oxygen anions [49]. The magnetic moments of  $\text{Fe}^{3+}$  ions (spin =  $5/2$ ) in A-sites and B-sites are antiparallel to each other, and cancels each other out because there is a same number  $\text{Fe}^{3+}$  ions in these two sublattices as demonstrated in Figure 3.3 [57, 58]. Therefore, the net moment in magnetite originates from the uncompensated ( $\text{Fe}^{2+}$ ,  $3d^4$ ) moment with spin 2. The net moment per formula unit is given by [59]:

$$M = M_{oct} - M_{tet} \quad (3.1)$$

where  $M_{oct}$  and  $M_{tet}$  are the magnetic moments of the octahedral and tetrahedral sites, respectively. And for magnetite, the net magnetic moment per  $\text{Fe}_3\text{O}_4$  unit is equal to  $= [(5+4)-5] = 4\mu_B$  at  $T = 0$  K [19, 49, 57]. As stated before, the ordering of magnetic moments in ferrimagnetic magnetite originates from super-exchange interactions between cations through mediation by the oxygen ions where the  $3d$  orbital of Fe overlaps with the  $2p$  orbital of oxygen. For magnetite, the inter-sublattice super-exchange between cations in A- and B-sites has a strength  $\mathcal{J}_{AB} = -28$  K, and intra-sublattice super-exchange interaction between cations in A-sites is antiferromagnetic with strength  $\mathcal{J}_{AA} = -18$  K, and finally the intra-sublattice super-exchange interaction between cations in B-sites has strength  $\mathcal{J}_{BB} = 3$  K [19].

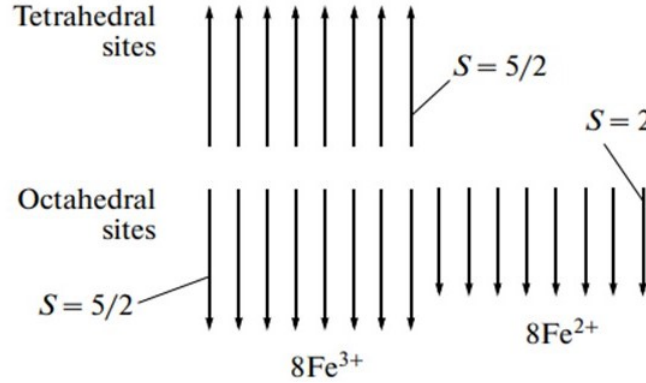


**Figure 3.3:** Diagram showing spin arrangement in magnetite [57].

Magnetite is a soft magnetic material with small magnetic anisotropy at room temperature. Different synthesis routes produces magnetite particles with coercivity ranging from  $\sim 30$  to  $250$  Oe [60], thus,  $\text{Fe}_3\text{O}_4$  is classified as a soft ferrimagnetic material. Materials are classified as soft or hard magnets depending on the field required to reverse their magnetization. If magnetization of a material can be reversed with an externally applied field  $H < 500$  Oe, such material is classified as a soft magnetic material [50]. Single-domain  $\text{Fe}_3\text{O}_4$  nanoparticles with sufficiently small



particle size shows superparamagnetic behaviour at room temperature. The critical diameter ( $d_{SD}$ ) for magnetite particles to form magnetic single-domain structure is reported to be in the range 25 - 80 nm [61]. And different threshold or critical diameter ( $d_{SPM}$ ) values to observe superparamagnetic behaviour in magnetite are reported in literature e.g. Cornell [60] reported that magnetite becomes superparamagnetic for particle sizes smaller than 6 nm, Hah et al. [62] reported a value of ( $d_{SPM} < 11$  nm), and Reichel et al. [61] observed superparamagnetic behaviour for magnetite particles less than 25 nm.

Figure 3.4 shows field dependent magnetization curves for magnetite nanoparticles reported by [63]. The curve recorded at 295 K shows no hysteresis ( $H_c = 0$ , and  $M_r = 0$ ), while the curve recorded at low temperature (4 K) showed hysteresis behaviour.

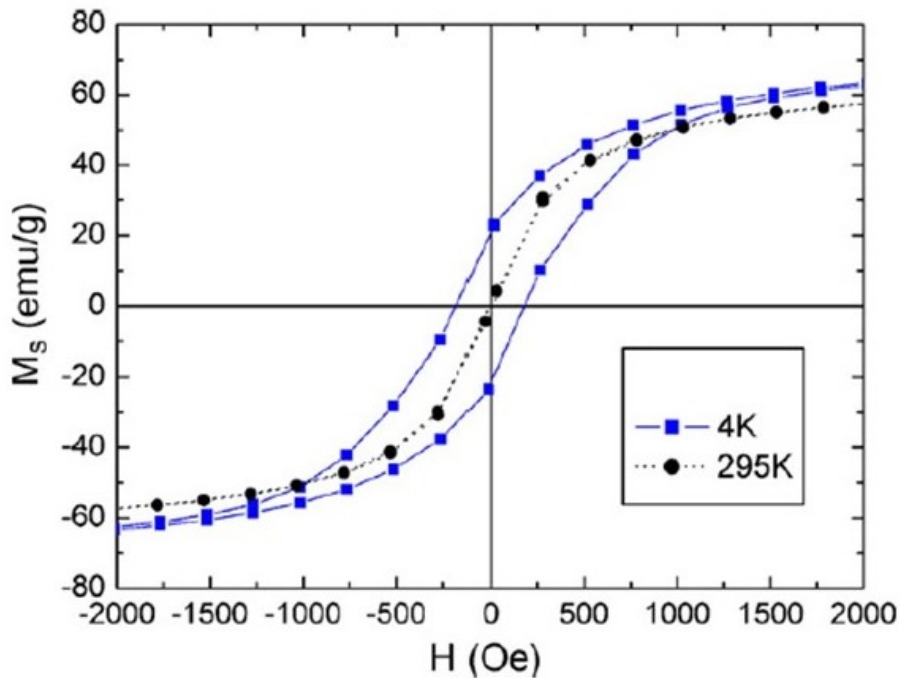


**Figure 3.4:**  $M$ - $H$  magnetization curves for magnetite at 4 K and 295 K [63].

A coercivity ( $H_c$ ) of 160 Oe and saturation magnetization ( $M_s$ ) of 73 emu/g were reported for this sample. However, the reported  $M_s$  value of 73 emu/g is lower than the saturation magnetization value of 92 - 100 emu/g for bulk  $\text{Fe}_3\text{O}_4$  [60] at room temperature. Amongst the iron oxides, magnetite is known to have the highest.

Room temperature Mössbauer spectrum of superparamagnetic magnetite nanoparticles i.e.  $d < d_{SPM}$  shows a central paramagnetic doublet. In contrast, magnetite nanoparticles with particle sizes  $d > d_{SPM}$  shows a magnetically ordered spectrum with two sextets attributed to the iron cations in A- and B-sites. The isomer shifts of the B-sites in pure magnetite is usually larger than the isomer shifts from the A-sites. This is because the B-sites contains mixed valance  $\text{Fe}^{3+}/\text{Fe}^{2+}$  ions and



$\text{Fe}^{2+}$  ions contributes to the increased isomer shifts in B-sites compared to A-sites which contains only  $\text{Fe}^{3+}$  ions. In addition, the magnetic hyperfine field for  $\text{Fe}^{3+}$  in tetrahedral A-sites are larger than octahedral sites due to their different crystalline environment [64].

### 3.3 Cobalt-Ferrites ( $\text{CoFe}_2\text{O}_4$ ) nanoparticles

#### Crystal Structure

Cobalt ferrite ( $\text{CoFe}_2\text{O}_4$ ) with space group  $Fd\bar{3}m$ , has a cubic inverse spinel structure [50]. The crystal structure of  $\text{CoFe}_2\text{O}_4$  is presented in Figure 3.5. The blue spheres represents  $\text{Fe}^{3+}$  ions in tetrahedral coordination (the A-sites), and the yellow/red spheres represents  $\text{Fe}^{3+}/\text{Co}^{2+}$  ions occupying the octahedral coordination (the B-sites), and the dark grey-sphere are oxygen ions [50].

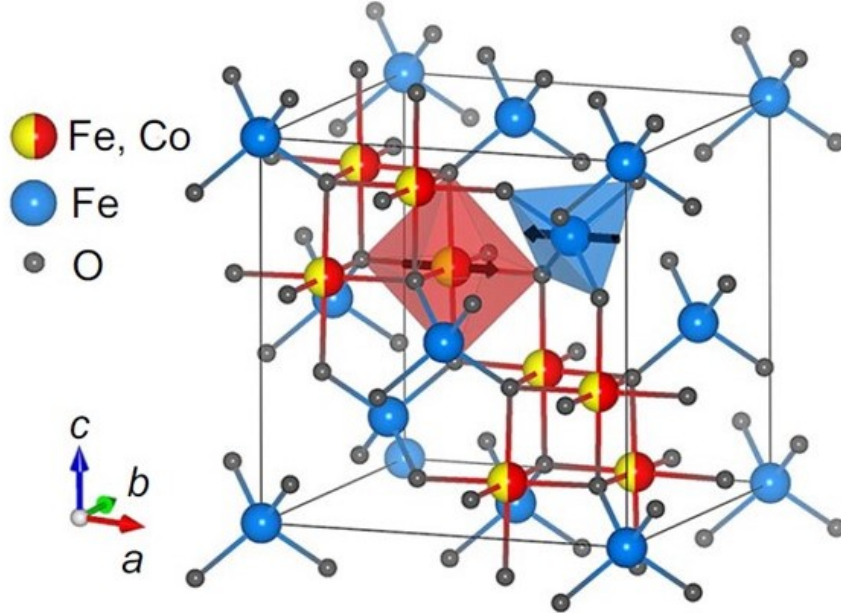


**Figure 3.5:** Crystal structures of cobalt-ferrite nanoparticles [50].

For a well crystallized  $\text{CoFe}_2\text{O}_4$  phase, all the tetrahedral sites are occupied by  $\text{Fe}^{3+}$  ions and the octahedral sites are shared by half of  $\text{Co}^{2+}$  ions and half of  $\text{Fe}^{3+}$  ions and its structure can be described as [50]:



However, it is generally accepted that  $\text{Co}^{2+}$  ions are distributed in both A- and B-sublattices. The cations in the partially inverse structure of  $\text{CoFe}_2\text{O}_4$  are distributed as follows [65]:



where  $\sigma$  is known as the degree of inversion. When  $\sigma$  is equal to 1, we get the normal inverse structure where the tetrahedral sites are occupied by the  $\text{Fe}^{3+}$  ions only. The degree of inversion depends on the synthesis procedure.

The phase identification of  $\text{CoFe}_2\text{O}_4$  by XRD technique shows same XRD reflections to that of pure  $\text{Fe}_3\text{O}_4$ . The resemblance of the XRD patterns of  $\text{CoFe}_2\text{O}_4$  and pure  $\text{Fe}_3\text{O}_4$  indicates that these ferrites have the same inverse cubic spinel structure [5]. Indeed, in the structure of  $\text{CoFe}_2\text{O}_4$ , only the  $\text{Fe}^{2+}$  ions are replaced with  $\text{Co}^{2+}$  ions and therefore  $\text{CoFe}_2\text{O}_4$  retains the cubic inverse structure. Figure 3.6 shows XRD pattern for  $\text{CoFe}_2\text{O}_4$  nanoparticles reported by Zhao and Ma [66]. It can be seen that the XRD pattern for  $\text{CoFe}_2\text{O}_4$  confirms the formation of the cubic inverse spinel structure similar to magnetite, compare XRD patterns in Figure 3.2 and 3.6.

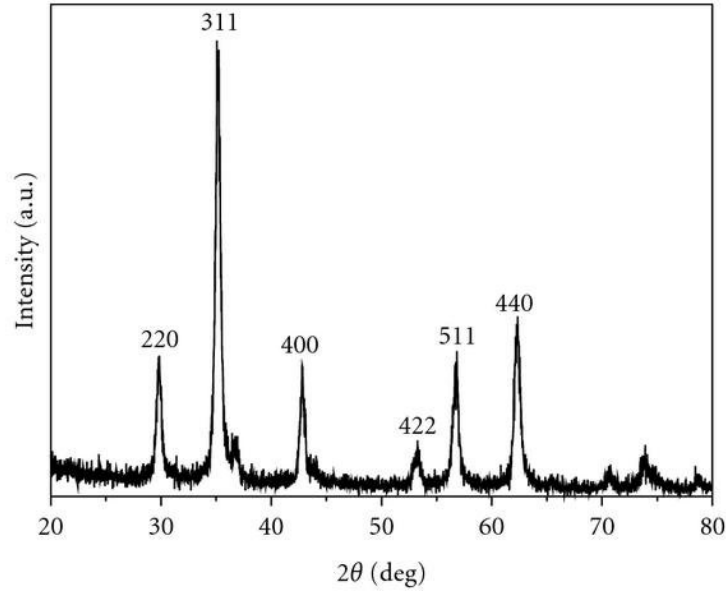


**Figure 3.6:** Powder X-ray diffraction pattern for  $\text{CoFe}_2\text{O}_4$  nanoparticles [66].

## Magnetic Properties

Cobalt-ferrites possess interesting magnetic properties such as high coercivity, moderate saturation magnetization, and high chemical stability [67, 68]. The Co-doped ferrite i.e.  $\text{CoFe}_2\text{O}_4$  is ferrimagnetic below its Curie temperature of  $\sim 789\text{ K}$  [69]. Ferrimagnetism in this compound also originates from super-exchange interactions between magnetic moments of  $\text{Fe}^{3+}$  ions at octahedral and tetrahedral sites, and  $\text{Co}^{2+}$  ions at octahedral sites via  $\text{O}^{2-}$  ions. For  $\text{CoFe}_2\text{O}_4$  system, the inter-sublattice super-exchange has a strength  $\mathcal{J}_{AB} = -25K_B$ , and intra-sublattice super-exchange interactions of strengths  $\mathcal{J}_{AA} = -18K_B$  and  $\mathcal{J}_{BB} = 3.9K_B$  [70]. The overall magnetic moment per  $\text{CoFe}_2\text{O}_4$  formula unit is given by the magnetic moment of the

$\text{Co}^{2+}$  ions which is equal to  $\sim 3\mu_B$ . Therefore the net moments is  $M = [(5 + 3) - 5] = 3\mu_B$  per  $\text{CoFe}_2\text{O}_4$  formula unit [50]. The magnetic properties of  $\text{Fe}_3\text{O}_4$  based ferrites can be tuned by substituting the  $\text{Fe}^{2+}$  ions with higher anisotropic  $\text{Co}^{2+}$  ions which significantly increases the coercivity in  $\text{CoFe}_2\text{O}_4$  nanoparticles [5].

Figure 3.7 shows  $M$ - $H$  magnetization curves for  $\text{CoFe}_2\text{O}_4$  nanoparticles recorded at 10 K and 300 K reported by Mahhouti et al. [71]. The room temperature magnetization curve shows reversible curve typically superparamagnetic behaviour. In contrast, the  $M$ - $H$  recorded at 10 K exhibits hysteresis with a significantly high coercive field ( $H_c$ ) of 18.6 kOe compared to a 315 Oe at 300 K. Because of the superparamagnetic behaviour at room temperature, the  $\text{CoFe}_2\text{O}_4$  nanoparticles behaves as a soft magnet with small coercivity.  $\text{CoFe}_2\text{O}_4$  is generally accepted as a strong magnet [50]. However, it can also be regarded as a semi-hard magnet i.e. exists in between soft and hard magnets [67]. Important to note is the significant increase in the coercivity of the Co-doped ferrite compared to pure magnetite. The two samples reported in Figs. 3.4 and 3.7 have comparable particle sizes but the coercivity of the Co-doped sample at low temperature is more than 100 times higher than the coercivity of the pure magnetite sample. The results demonstrates the effect of  $\text{Co}^{2+}$  substitution in magnetite. The substitution of  $\text{Fe}^{2+}$  with  $\text{Co}^{2+}$  increases the magneto-crystalline anisotropy of the ferrite —hence the high coercivity in  $\text{CoFe}_2\text{O}_4$  nanoparticles.  $\text{CoFe}_2\text{O}_4$  ferrite is known to have moderate  $H_c$  values less than 5.4 kOe, depending on the particle morphology and cobalt to iron ratio [50]. However,  $H_c$  values can go as high as 18.6 kOe for the  $\text{CoFe}_2\text{O}_4$ .  $\text{CoFe}_2\text{O}_4$  system as reported by [71].

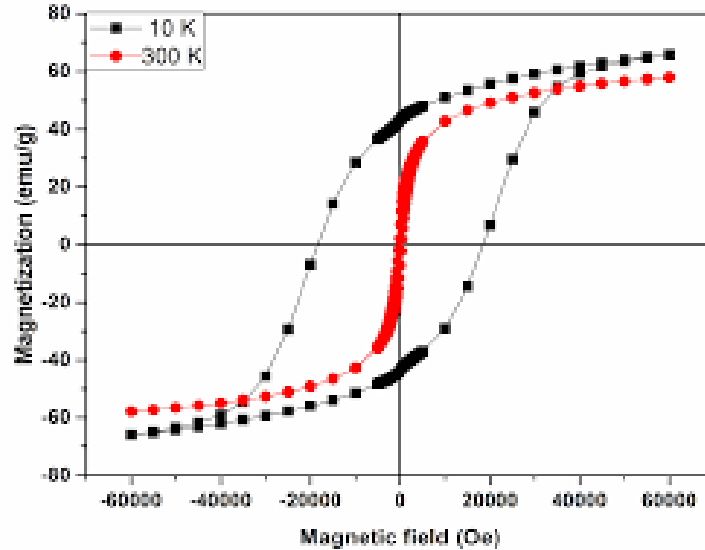


**Figure 3.7:**  $M$ - $H$  hysteresis curves for a cobalt-ferrite nanoparticles recorded at 10 K and 300 K [71].

In its bulk form,  $\text{CoFe}_2\text{O}_4$  has a maximum saturation magnetization ( $M_s$ ) of 80 emu/g [50, 72]. For the sample considered in Figure 3.7, the experimentally ob-

served values of  $M_s$  were in the range of 58 to 65 emu/g. The high values are due to enhanced effective anisotropy constant because of the contribution from the surface anisotropy constant [73].

Similarly to pure  $\text{Fe}_3\text{O}_4$ , the Mössbauer spectrum of a magnetically ordered  $\text{CoFe}_2\text{O}_4$  phase is composed of two superimposed sextets assigned to A- and B-sites and a paramagnetic doublet is observed for a sample in superparamagnetic state. For the  $\text{CoFe}_2\text{O}_4$  ferrite (where all the  $\text{Fe}^{2+}$  ions are substituted by  $\text{Co}^{2+}$ ), the isomer shifts for both the A and B sites are usually similar and are consistent with  $\text{Fe}^{3+}$  in either a high-spin or low-spin state. This is because in both the A- and B-sites, a Mössbauer spectroscopy based on iron will only "see" the iron nuclide in both sites.

### 3.4 Nickel-Ferrites ( $\text{NiFe}_2\text{O}_4$ ) nanoparticles

#### Crystal Structure

Nickel ferrite ( $\text{NiFe}_2\text{O}_4$ ) has got the same cubic inverse spinel structure to the other two ferrites discussed in section 3.2 and 3.3. Figure 3.8 represents the inverse-spinel ferrites of a well crystallized nickel ferrite phase with the chemical formula  $(\text{Fe}^{3+})_A[\text{Ni}^{2+}, \text{Fe}^{3+}]_B\text{O}_4$ . In this structure, 16  $\text{Fe}^{3+}$  ions are evenly distributed across the tetrahedral A-sites and the octahedral B-sites (red spheres), 8  $\text{Ni}^{2+}$  ions occupy half of the octahedral sites (green spheres), and the oxygen ions are denoted by light blue spheres [74].

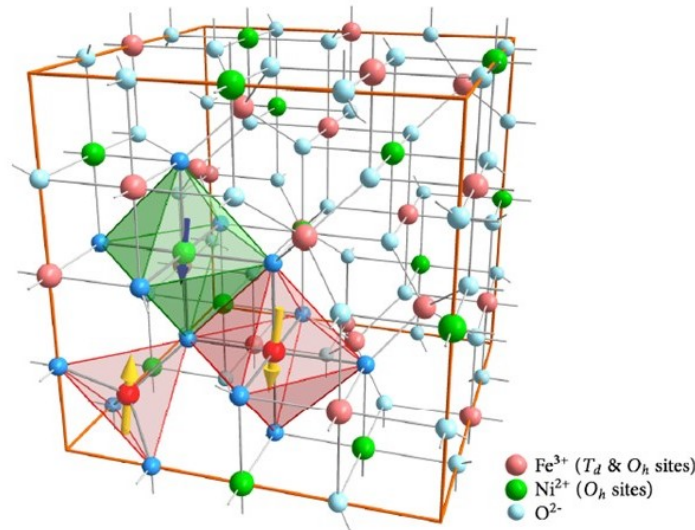


**Figure 3.8:** Inverse spinel cubic structure for Ni-doped ferrite [74].

The structure in Figure 3.8 shows all the  $\text{Ni}^{2+}$  ions in octahedral coordination. However, different preparation processes could lead to distribution of the  $\text{Ni}^{2+}$  ions in both A- and B-sites [16, 58]. And the general structural formula for  $\text{NiFe}_2\text{O}_4$  is

written as [58]:

$$(\text{Ni}_{1-\sigma}^{2+}\text{Fe}_{\sigma}^{3+})_{\text{A}}[\text{Ni}_{\sigma}^{2+}, \text{Fe}_{2-\sigma}^{3+}]_{\text{B}}\text{O}_4 \quad (3.4)$$

where  $\sigma$  is the fraction of the A-sites occupied by  $\text{Fe}^{3+}$  ions and it is known as the degree of inversion. Equation 3.4 represents the structure of **partially** inverse spinel  $\text{NiFe}_2\text{O}_4$ , and when  $\sigma$  is equal to 1, we get the normal inverse structure where the tetrahedral sites are occupied by the  $\text{Fe}^{3+}$  ions only.

$\text{NiFe}_2\text{O}_4$  ferrites also shows same XRD features as  $\text{Fe}_3\text{O}_4$  due to the similarities in their crystal structure. Figure 3.9 shows a powder X-ray diffraction spectrum for  $\text{NiFe}_2\text{O}_4$  as reported by Maaz et al. [75], the observed XRD peaks are indexed to  $F\bar{d}3m$  space group.

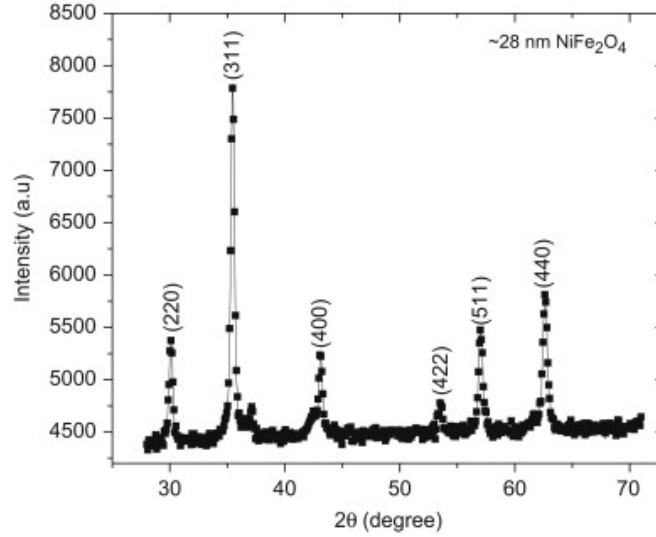


**Figure 3.9:** X-ray diffraction pattern of nickel-ferrite [75].

## Magnetic Properties

The nickel-ferrite is a soft magnetic material with low coercivity and moderate saturation magnetization in contrast to that of cobalt-ferrites [76]. In its bulk form,  $\text{NiFe}_2\text{O}_4$  ferrite shows ferrimagnetism with  $T_C$  865 K [74]. The ferrimagnetic ordering originates from magnetic moment of anti-parallel spins between tetrahedrally coordinated  $\text{Fe}^{3+}$  ions and octahedrally coordinated  $\text{Fe}^{3+}/\text{Ni}^{2+}$  ions [74, 77]. This process happens through super-exchange interactions between the cations in A- and B-sites mediated by the overlap of the Fe 3d orbitals with the intermediate oxygen 2p orbitals as illustrated in section 2.2.4. A strong and antiferromagnetic inter-sublattice super-exchange constant of  $\mathcal{J}_{AB} = -25K_B$ , and intra-sublattice super-exchange interactions constants of  $\mathcal{J}_{AA} = -4K_B$  and  $\mathcal{J}_{BB} = 4K_B$  [78]. The magnetic moments due  $\text{Fe}^{3+}$  ions in the two sublattices compensate each other, and the

magnetic moment due to the  $\text{Fe}^{3+}$  ions in the B-sublattice is not compensated resulting in a net magnetic moment of  $M = [(5 + 2) - 5] = 2\mu_B$  for the bulk  $\text{NiFe}_2\text{O}_4$  spinel structure [74].

Figure 3.10 presents the hysteresis loop of  $\text{NiFe}_2\text{O}_4$  nanoparticles measured at 77 K and 300 K temperatures reported by Maaz et al. [75]. At room temperature, the sample showed some superparamagnetic behaviour with blocking temperature  $T_B \sim 221$  K. The coercivity of the sample increased from 89 Oe at room temperature to 175 Oe when the temperature was reduced to 77 K.  $M$ - $H$  measurements showed saturation magnetization ( $M_s$ ) of 45 emu/g for the sample measured at 77 K, the obtained  $M_s$  value was smaller than the bulk value of 56 emu/g for  $\text{NiFe}_2\text{O}_4$  [75]. The decrease in  $M_s$  for nanoparticles compared to their bulk counterparts is reported to originate from the surface effects, high surface to volume ratio, and canted spins on the particle surface [79]. Sivakumar et al. [80] managed to synthesize  $\text{NiFe}_2\text{O}_4$  nanoparticles with  $H_c$  value of 250.8 Oe and saturation magnetization of 51.3 emu/g, the  $M_s$  for this sample was close to the  $M_s$  value of bulk  $\text{NiFe}_2\text{O}_4$ . The small  $H_c$  values from these two studies [75, 80] confirms that indeed  $\text{NiFe}_2\text{O}_4$  is a soft magnet.

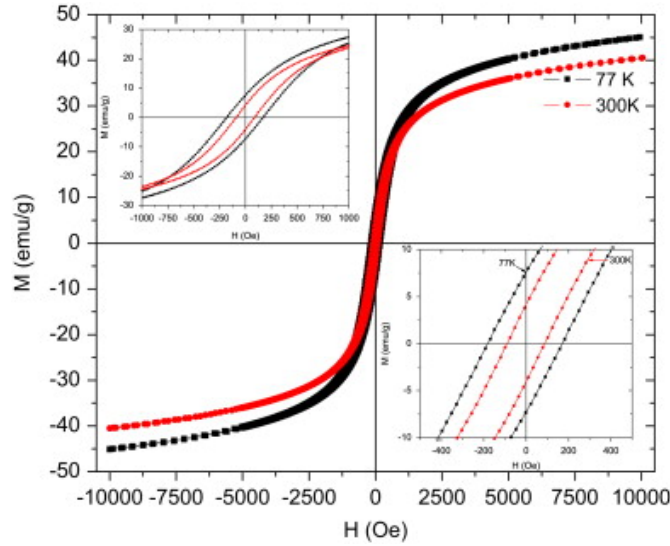


**Figure 3.10:**  $M$ - $H$  hysteresis loops of Ni-doped ferrite measured at 77 K and 300 K [75].

Magnetically ordered  $\text{NiFe}_2\text{O}_4$  shows a Mössbauer spectrum with a magnetically split sextet which can be fitted with two sextets as a linear combination of two Lorentzian lines attributed to the A- and B-sites. The two sextets can be fitted well with similar isomer shifts for both the A- and B-sites e.g. as reported by Lazarova et al. [16]. While the tetrahedral and octahedral sites are represented by different magnetic hyperfine fields.

In this work, three ferrites nanoparticles (i.e.  $\text{Fe}_3\text{O}_4$ ,  $\text{CoFe}_2\text{O}_4$ , and  $\text{NiFe}_2\text{O}_4$ ) will be synthesized using co-precipitation methods and their magnetic properties will be investigated using Mössbauer spectroscopy and vibrating sample magnetometer.

# Chapter 4

## Methodology

### 4.1 Introduction

This chapter gives an outline of the research methods that were employed in the study. The theoretical aspect of the techniques employed in this project is presented in section 4.2. The synthesis procedures for the three ferrite nanoparticles as well as experimental methods and detailed experimental conditions used in this study can be found in section 4.3 of this chapter.

### 4.2 Experimental Techniques

#### 4.2.1 X-Ray Diffraction

X-Ray diffraction (XRD) is a high-tech, non-destructive technique for structure and phase identification of crystalline materials [81]. The technique is based on the interaction of the X-ray beam with the electronic structure of the specimen. X-rays are artificially created in the cathode ray tube when a beam of high energetic electrons collide with a target metal. By using a filter, a monochromatic X-ray beam is produced and collimated before directed to the sample [81]. Presented in Figure 4.1 is a Bruker advanced D8 X-ray diffractometer showing the three main features of a diffractometer i.e. X-ray tube, sample stage, and a detector.

X-ray diffraction pattern is produced by constructive interference of a monochromatic beam of x-rays scattered at specific angles from each set of lattice planes in a sample when Bragg's law condition is satisfied [81, 83]:

$$n\lambda = 2d \sin \theta \quad (4.1)$$

where  $n$  is an integer,  $\lambda$  the wavelength of the x-rays,  $d$  is the interplanar spacing and  $\theta$  is the diffraction angle [83]. Figure 4.2 shows a schematic diagram representation of Bragg's law condition. Constructive wave interference will occur if the extra distance ( $AB+AC$ ) travelled by ray 2 is equal to an integral multiple of the wavelength  $n\lambda$ . The Bragg's law relates wavelength of electromagnetic radiation to the angle of diffraction and the lattice spacing of the crystalline sample. The samples x-rays



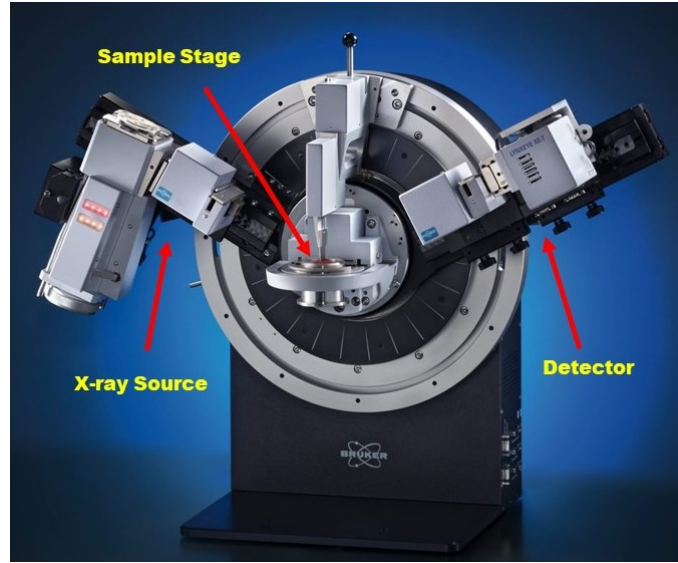


**Figure 4.1:** Image of a Bruker Advance D8 X-ray diffractometer [82].

pattern is obtained by scanning through a range of  $2\theta$  angles. The XRD pattern is a graphical representation of the X-rays intensity versus diffraction angle  $2\theta$ .

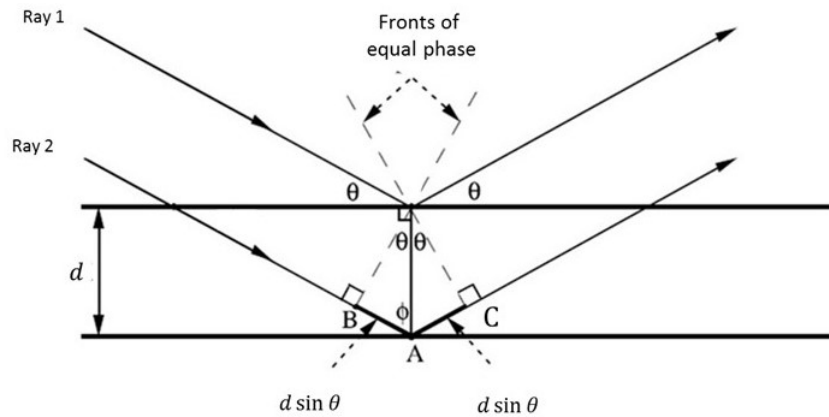


**Figure 4.2:** Schematic diagram illustrating Bragg's law [84].

### Williamson-Hall Plot Method

The Williamson-Hall (W-H) plot can be used to estimate the crystallite size and micro-strain from X-ray diffraction data [85, 86]. Unlike the Scherrer's formula, the (W-H) plot method takes into account the effect of both crystallites size and micro-strain on the broadening of the XRD peaks. It is known that the broadening of the XRD peaks is due to the sample and the instrument according to:

$$\beta_{XRD} = \beta_{instrument} + \beta_{sample} \quad (4.2)$$

If the broadening due to the instrument is corrected using a standard sample with small micro strain and large particle size, then the total broadening of the XRD



peak ( $\beta_t$ ) is only due to the sample and equation 4.2 reduces to:

$$\beta_t = \beta_{XRD} = \beta_{sample} \quad (4.3)$$

In the Scherrer's formula, the broadening of the peak is assumed to be only due to the effect of crystallite size. However, in the (W-H) plot method, the total broadening ( $\beta_t$ ) of the peaks (after instrument broadening is corrected) is due to the combined effect of crystallite size ( $\beta_D$ ) and macro-strain ( $\beta_\epsilon$ ):

$$\beta_t = \beta_\epsilon + \beta_D \quad (4.4)$$

The contribution of the crystallite size to the XRD peak broadening can be expressed using Debye-Scherrer's equation as [85, 87]:

$$\beta_D = \frac{K\lambda}{D \cos \theta} \quad (4.5)$$

Where  $K$  is called the shape factor constant,  $\lambda$  is the wavelength of the incident X-rays,  $D$  the crystallite size, and  $\theta$  is the Bragg angle. On the other hand, the contribution of the micro-strain to the XRD peak broadening is given by [85, 87]:

$$\beta_\epsilon = 4\epsilon \tan \theta \quad (4.6)$$

Taking equation 4.5 and equation 4.6 and substituting them into equation 4.4, we obtain the (W-H) method equation;

$$\beta_t \cos \theta = 4\epsilon \sin \theta + \frac{K\lambda}{D} \quad (4.7)$$

Equation 4.7, expressed in the form of a straight line equation as  $y = mx + c$  where,  $y = \beta_t \cos \theta$ ,  $m = 4\epsilon$ ,  $x = \sin \theta$  and  $c = \frac{K\lambda}{D}$ . From the plot, dimensionless micro-strain ( $\epsilon$ ) was determined from gradient, while the intercept was used to calculate the crystallite size  $D$ .

## 4.2.2 Transmission Electron Microscope

For structural and morphology characterization of the nano-sized ferrites samples, the transmission electron microscopes (TEM) was used. The transmission electron microscope (TEM) has become the premier tool for the characterization of materials [84]. The technique is ideal for a number of different fields such as life sciences, nanotechnology, medical biological and materials research, where it provides topographical, morphological, compositional and crystalline information. The TEM provides researchers/scientist the much needed atomic scale compositional and structural analysis for their materials [88]. TEM works on the same basic principle as light microscopy. However, electrons and magnetic lenses instead of light and glass lenses are used in a TEM to form an image. The technique relies on the transmission of high energetic electron beam through a very thin specimen to form a highly magnified TEM image. The TEM instrument consists mainly of three sets of major electromagnetic lenses: the **condenser lens** which is used to bring focused

electron beam into the specimen, at the heart of the TEM there is the **objective lens** which brings scattered and transmitted beam of electrons into focus and forms the first image of the specimen, (3) the first image and diffraction pattern produced by the objective lens is then magnified and projected into the viewing screen by a set of **projector lens** [84, 88]. This setup is illustrated in Figure 4.3.

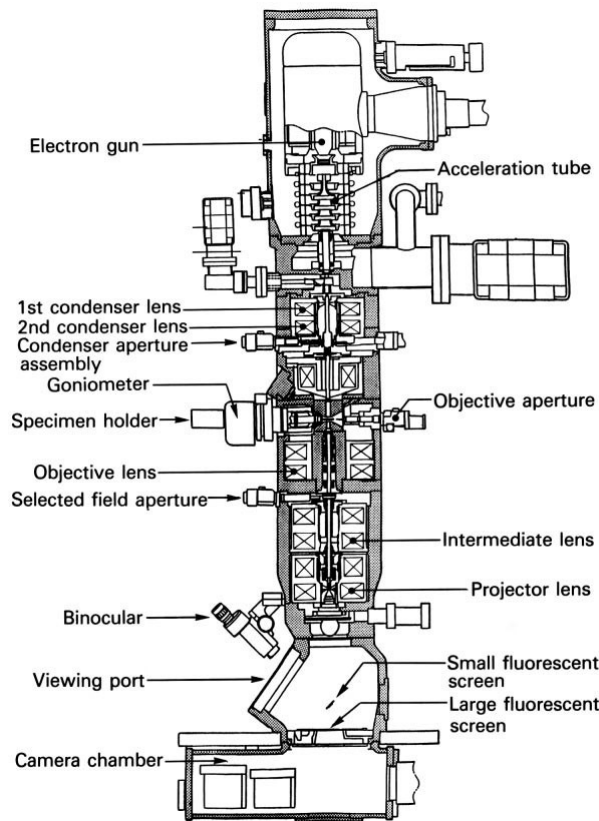


**Figure 4.3:** A diagram showing the internal structure of a transmission electron microscope [84].

### Image Formation in TEM

Image contrast in Transmission Electron Microscopy arises because of the scattering of the incident beam by the specimen. “Contrast” is the distinct appearance of features in an image. Conventional TEM image is obtained using diffraction contrast, which relies on the change of intensity in a TEM image when diffraction conditions changes in the different areas of the specimen [84, 88]. A TEM image based on diffraction contrast depends on the beam selected to form the image, a bright-field (BF) image is formed when the transmitted is selected and a dark-field (DF) image is formed when the diffracted beam is selected as shown in Figure 4.4. A bright-field TEM image is acquired by the objective aperture being placed around the transmitted beam, excluding out the diffracted one (see Fig.4.4 (A)). In a BF image the region that does not diffract would appear bright and the area where diffraction

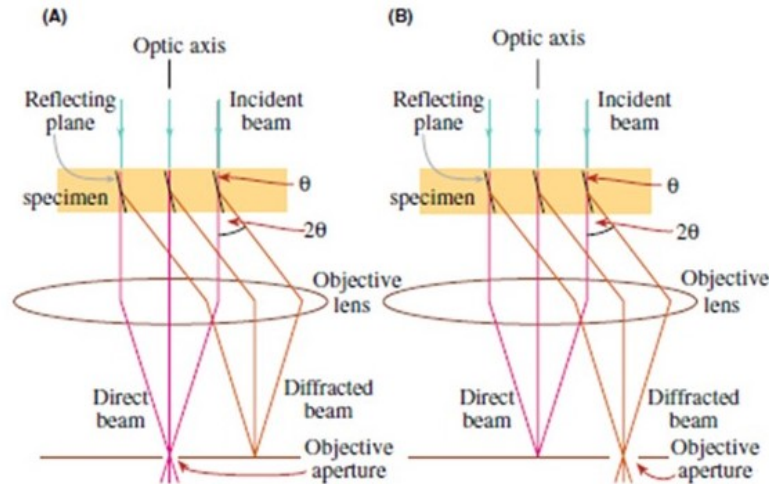


**Figure 4.4:** Bright-field (A) and Dark-field image formation in a TEM [88].

has occurred it will appear darker [84, 88]. On the other hand, a dark-field image is formed by blocking the transmitted beam with an aperture and allowing the diffracted beam to form the image (see Fig. 4.4 (B)). In this case regions that does not diffract will appear dark and regions that diffract will appear bright.

Besides using "diffraction" contrast to form TEM images, "phase-contrast imaging" can be used to form high resolution TEM (HR-TEM) images. In this technique, the phase of the diffracted electron wave is preserved and interferes constructively or destructively with the phase of the transmitted wave [84]. Unlike diffraction contrast where one beam can be selected to form images phase contrast imaging requires the selection of more than one beam collected at the objective aperture to form the HR-TEM image.

### Energy Dispersive X-ray Spectroscopy

The versatility of the TEM equipment allows for the compositional analysis of a given specimen through the energy dispersive x-ray spectroscopy (EDS) technique. An EDS detector is attached to the TEM equipment and its role is to record characteristic x-rays versus their energy and form an EDS spectrum. Typical EDS spectrum is portrayed as a plot of x-ray counts vs energy (keV), with each peak corresponding to the presence of a specific element in the sample [89, 90].

Energy dispersive X-ray spectrum (EDS) is obtained by using the characteristic X-rays signal. Figure 4.5 illustrates the process of generating characteristic x-rays and EDS spectrum. Characteristic x-rays are produced when the primary electron beam collides with an electron in an inner shell of a target atom with sufficient energy to remove the electron from the atom creating a vacancy e.g. in a K-shell as shown in Fig. 4.5 (a). The vacancy created in the shell is filled when an electron from a higher level (e.g. L-shell) drops down into the lower-energy level (K-shell) containing the vacancy creating an x-ray photon in the process [90]. An energy-dispersive spectrometer measures the energy of the created x-ray photon from the

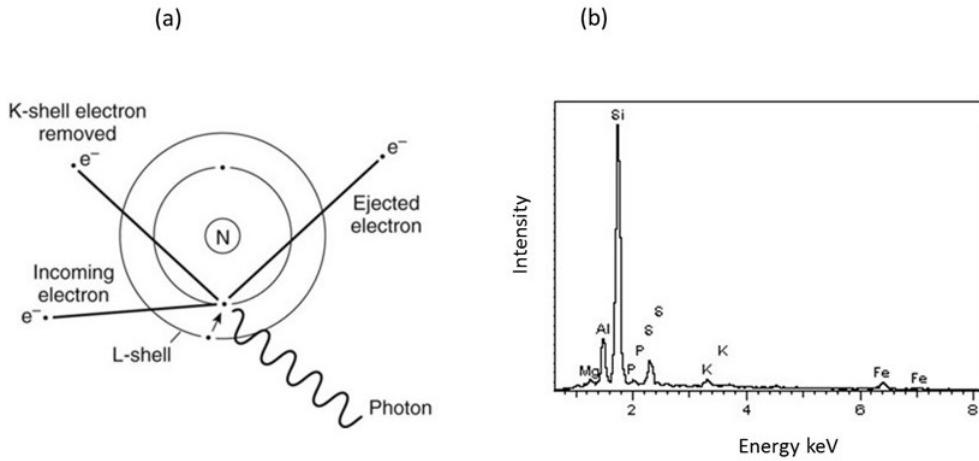


**Figure 4.5:** Diagram showing the creation of characteristic X-rays (a) and EDS spectrum (b) [91].

number of electron-hole pairs generated in a semiconductor and disperses them according to their energies which is then displayed as an energy-dispersive spectrum as shown in Figure 4.5.

### 4.2.3 Mössbauer Spectroscopy

#### Introduction

Mössbauer spectroscopy (MS) is a nuclear technique based on the recoilless emission and resonant absorption of  $\gamma$ -rays by identical nuclei bound to solids [92, 93]. The technique is widely used in mineralogy to provide information such as valence state, cation distribution and coordination environment of iron which occur in nature as  $\text{Fe}^0$ ,  $\text{Fe}^{2+}$  and  $\text{Fe}^{3+}$ . Mössbauer spectroscopy is also a very good technique for identification of Fe oxide phases on the basis of their magnetic properties [92, 94–96].

#### The Mössbauer Effect

Mössbauer spectroscopy is a spectroscopic technique based on the Mössbauer effect. In this process, a radioactive nuclide emits  $\gamma$ -rays when it undergoes nuclear transitions from excited state to ground state, subsequently these  $\gamma$ -rays are resonantly absorbed by identical nuclei since identical nuclei have equal transition energy between the excited and ground states [92]. However, "free" nuclei experiences recoil during nuclear transitions and the Mössbauer effect cannot occur e.g. if a nucleus gives off  $\gamma$ -rays, it must recoil in the same way that a rifle recoils when a bullet is fired out of it, the resulting energy of the emitted  $\gamma$ -ray is therefore given by  $E_\gamma = E_0 - E_R$  (where  $E_0$  is the energy of the nuclear transition and  $E_R$  is the energy of the recoil. Likewise, the absorbing nucleus of an isolated atom can absorb the  $\gamma$ -ray from the emitting nucleus and recoil, the resulting energy of the photon is given by  $E_\gamma = E_0 + E_R$ . The centres of the emission and absorption spectra are displaced by  $2E_R$  as illustrated in Figure 4.6. In this case, a nuclear resonant emission-absorption process cannot be observed because the recoil energy of both

the source and emitter are relatively large for "free" nuclei [92].

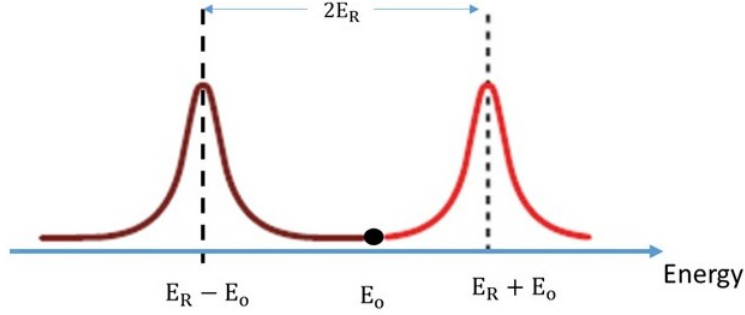


**Figure 4.6:** Diagram showing emission spectrum (brown) and absorption spectrum (red) of  $\gamma$ -ray process [97].

The resonant emission-absorption process can only be achieved if the energy of the emitted  $\gamma$ -ray is precisely equal to the nuclear transition energy according to:

$$E_\gamma = E_0 \quad (4.8)$$

For an isolated and initially at rest atom, conservation of momentum requires that it must recoil with momentum  $\vec{p}_{nucleus} = -\vec{p}_\gamma$ , in the process acquiring a recoil energy,  $E_R$ , given by Dyar et al. [92]:

$$E_R = \frac{(\vec{p}_{nucleus})^2}{2m} = \frac{(\vec{p}_\gamma)^2}{2m} = \frac{E_\gamma^2}{2mc^2} \quad (4.9)$$

Due to this recoil, the process of recoilless emission and resonant absorption will not occur for free nuclei. However, In 1957, Rudolf Mössbauer discovered that if the emitting and absorbing nuclei are strongly bound in crystalline solids, recoilless emission and resonant absorption of  $\gamma$ -rays can occur since the recoil energy is absorbed by the whole lattice rather than a single nucleus. The mass  $m$  in equation 4.9 is replaced by the mass of the whole solid  $M$  such that  $E_R$  is negligibly small [92, 96].

### Hyperfine Interactions

The interactions between the positively charged Mössbauer nucleus and the electric and magnetic fields created by the Mössbauer atom itself and other atoms in the local environment results in the shift and/or splitting of the nuclear energy of the Mössbauer nucleus [98]. These interactions are generally referred as hyperfine interactions. Important information regarding the chemical and physical properties of the sample can be obtained from three hyperfine interactions i.e. isomer shift (IS), quadrupole hyperfine splitting (QS), and hyperfine magnetic field ( $B_{hf}$ ). Therefore Mössbauer spectra are described using these three parameters whose interactions are governed by the Hamiltonian  $\mathcal{H}$  [98]:

$$\mathcal{H} = \mathcal{H}(e0) + \mathcal{H}(e2) + \mathcal{H}(m1) \quad (4.10)$$

where  $\mathcal{H}(e0)$ ,  $\mathcal{H}(e2)$ , and  $\mathcal{H}(m1)$  relates to the Coulombic interactions between the Mössbauer nucleus and its surrounding electrons, interaction between nuclear quadrupole moment and electric field gradient, and the interaction between the Mössbauer nucleus and any magnetic field neighbourhood, respectively. The  $e0$  interaction shifts the position of the Mössbauer lines while the  $e2$  and the  $m1$  interactions induce splitting of the Mössbauer lines [98]. The three Mössbauer parameters are discussed below.

### Isomer Shift (IS)

The isomer shift (IS or  $\delta$ ) arises from the difference in  $s$ -electron density between the source and the absorber nucleus. Furthermore, the nuclear radii of the excited  $R_e$  and ground  $R_g$  states are not equal which manifests itself as a shift of the nuclear levels giving by [98, 99]:

$$\delta = IS = \frac{2}{5}\pi Ze^2 \left[ |\psi(0)|_{(A)}^2 - |\psi(0)|_{(S)}^2 \right] \left[ R_e^2 - R_g^2 \right] \quad (4.11)$$

where  $Z$  is the atomic number,  $e$  electron charge,  $e\psi(0)|_{(A)}^2$  is the electronic charge density in the absorber nucleus, and  $e\psi(0)|_{(S)}^2$  is the electronic charge density in the source nucleus. Figure 4.7 is a graphical representation of the isomer shift in a Mössbauer spectrum when the source and absorber nucleus are in different chemical environments. The measurement of the isomer shift provides information about the valance and oxidation state of the (Mössbauer) atom [92, 98, 99]. The isomer shift is given with respect to a suitable reference material,  $^{57}\text{Fe}$  isomer shifts are often reported relative to the centroid of the magnetically split spectrum of metallic  $\alpha$ -iron [98].

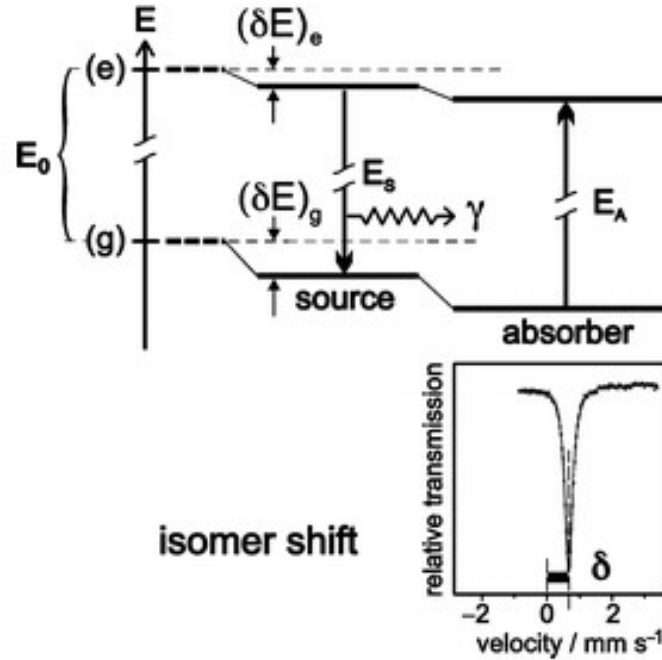


**Figure 4.7:** Schematic representation of the isomer shift [96].

#### 4.2.4 Quadrupole Hyperfine Splitting (QS)

Quadrupole hyperfine splitting (QS or  $\Delta E_Q$ ) arises due to interaction between electric quadrupole moment of the Mössbauer nucleus and electric field gradient (EFG) generated by the electrons in the sample. All nuclei with nuclear spin that is  $I > \frac{1}{2}$  possess nuclear quadrupole moment ( $eQ$ ) and the interaction of  $eQ$  with the EFG splits the nuclear energy levels which is usually observed as a doublet in a (Mössbauer) spectrum as illustrated in Figure 4.8. The electric quadrupole inter-

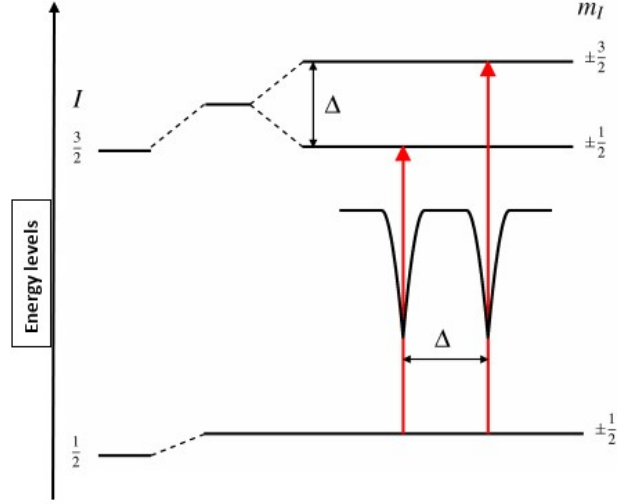


**Figure 4.8:** Schematic representation of quadrupole splitting [96].

action splits the  $I = \frac{3}{2}$  level into two sub-levels ( $m_I = \pm\frac{3}{2}, \pm\frac{1}{2}$ ) that are two-fold degenerate while the  $I = \frac{1}{2}$  level remains unsplit. This results into two observed transitions which are separated by [100]:

$$QS = \Delta E_Q = \frac{1}{2}eQV_{zz}\left(1 + \frac{\eta^2}{3}\right)^{\frac{1}{2}} \quad (4.12)$$

where  $\eta$  is called the asymmetry parameter which takes the form:

$$\eta = \frac{|V_{xx} - V_{yy}|}{V_{zz}} \quad (4.13)$$

In a simple case where EFG is axially symmetric i.e.  $\eta = 0$ , the energy difference between the two sub-levels is given by:

$$\Delta E_Q = \frac{eQV_{zz}}{2} \quad (4.14)$$

#### Magnetic Hyperfine Splitting

A nucleus with nuclear spin  $I > 0$  possess a magnetic dipole moment. The magnetic moment ( $\mu$ ) of the nucleus then interacts with the internal magnetic field created by the sample to further split the nuclear levels and this known as magnetic hyperfine



splitting. The interaction of  $\mu$  and magnetic field is governed by the Hamiltonian  $\mathcal{H}$  [98]:

$$\hat{\mathcal{H}}_m = -\hat{\vec{\mu}} \cdot \hat{\vec{B}} \quad (4.15)$$

$$\hat{\vec{B}} = -g_N \mu_N \hat{\vec{I}} \cdot \hat{\vec{B}} \quad (4.16)$$

where  $\mu_N$  is the nuclear magneton, and  $g_N$  is the nuclear Landé factor. It immediately follows that the eigenvalues  $E_M(m_I)$  of the Hamiltonian that governs the magnetic hyperfine interaction are given by:

$$E_M(m_I) = -\frac{\mu_B M_I}{I} \quad (4.17)$$

$$= -g_N \mu_N M_I \quad (m_I = I, I-1, \dots, -I) \quad (4.18)$$

Nucleus with spin  $I$  splits into  $2I+1$  states e.g. the excited state ( $I = 3/2$ ) will split into four substates ( $+\frac{3}{2}, +\frac{1}{2}, -\frac{1}{2}, -\frac{3}{2}$ ) and the ground state ( $I = 1/2$ ) will split into two substates ( $+\frac{1}{2}, -\frac{1}{2}$ ). This gives rise to six transition energies and these six

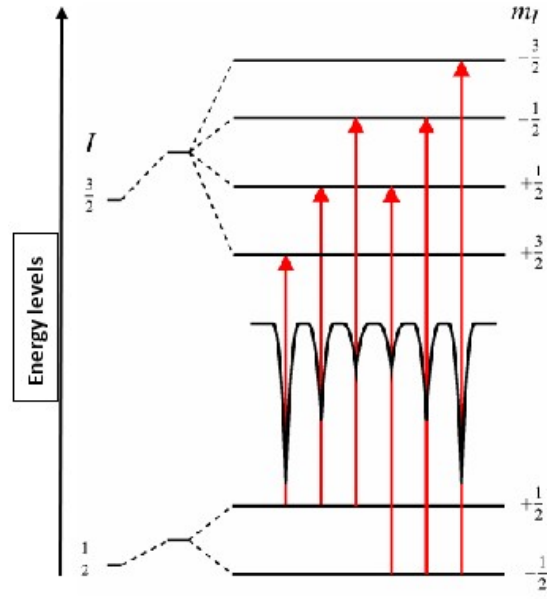


**Figure 4.9:** Energy levels transition to show a sextet hyperfine splitting of an MS spectra[96].

energy transition lines corresponds to a sextet Mössbauer spectrum as illustrated in Figure 4.9.

#### 4.2.5 Mössbauer Experimental Set-up

Figure 4.10 shows a typical set-up used to record Mössbauer spectrum. The set-up consists of the following main components: (i) The Mössbauer source ( $^{57}\text{Co}$ ) and absorber (sample), (ii) the collimator whose function is to produce parallel beam of  $\gamma$ -rays, (iii) the Mössbauer drive which moves the source relative to the sample,



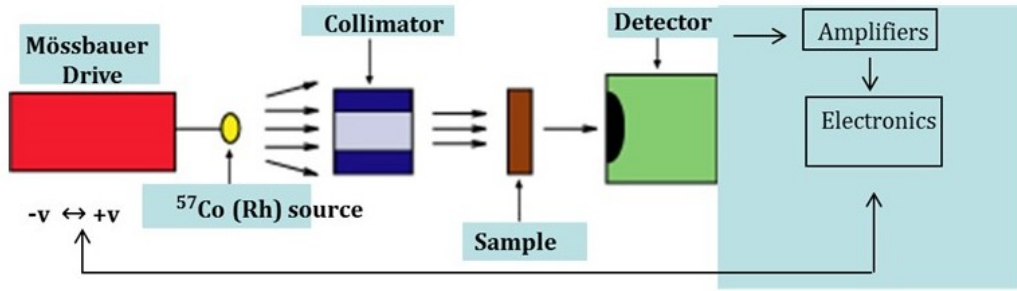


**Figure 4.10:** Schematic of the apparatus used in a Mössbauer spectroscopy (ref. Dyar).

a process that varies the emission energy, and (iv) the detector which records the number of transmitted  $\gamma$ -rays [101] as shown in Figure 4.10.

It was discussed in section (4.2.3) that resonance absorption occurs when the emission and absorption spectrum of the emitting and adsorbing nuclei overlaps. This is achieved by embedding the source and absorbing nuclei in solids to have recoilless emission and resonant absorption of the  $\gamma$ -rays. The process involved in recording of a Mössbauer spectrum is demonstrated in Figure 4.11. At first (very top of Fig. 4.11) there is no overlap between the emission and absorption spectrum. As the source is moved towards the absorber, its velocity changes hence its energy, the emission and absorption spectrum gradually change from no overlap to full overlap (middle of Fig. 4.11, and as the source moves pass the absorber this situation moves back to no overlap and a full spectrum is recorded (bottom of Fig. 4.11) [96, 101]. In the process a Mössbauer transmitted spectrum is recorded (blue), and

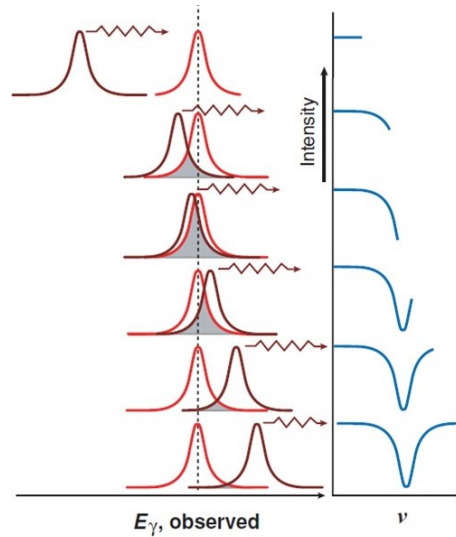


**Figure 4.11:** Schematic showing the recording of a Mössbauer spectrum using Doppler effect: emission spectrum (brown), absorption spectrum (red), and transmitted spectrum (blue) [96].

the Mössbauer parameters can be derived from this transmitted spectrum.

### 4.2.6 Vibrating-Sample Magnetometer

The vibrating-sample magnetometer has been in use for routine magnetic measurements as a function of temperature and field of ferromagnetic, ferrimagnetic, anti-ferromagnetic, paramagnetic and diamagnetic materials for many years[102, 103]. All magnetic induction measurements involve observations of the voltage induced in a detection coil by a flux change when the applied magnetic field, coil position or sample position is changed [102–104]. VSM permits precise magnetic moment measurements to be made in a uniform magnetic field as a function of temperature, magnetizing field, and crystallographic orientation [105]. It is a technique that measures the magnetic properties of a material based on Faraday’s Law of Induction. In a VSM, the sample is magnetized by constant applied magnetic field, producing what is sometimes called stray magnetic fields. As the sample is moved up and down i.e. vibrates along the  $z$ -axis it produces varying magnetic flux in the coils which in turn generates electric current in the coils according to Faraday’s law of induction [102]. The induced current in the pick-up coils is proportional to the magnetization of the sample [102]. Figure 4.12 demonstrates the operating principle of a vibrating sample magnetometer. The electromagnets provide the applied constant magnetic field  $H$ , the sample stage consists of the vibrator which moves the sample up and down along the  $z$ -axis producing varying magnetic fields with time, and the magnetic moment of the sample is determined from the induced current in the pick-up coils [102].

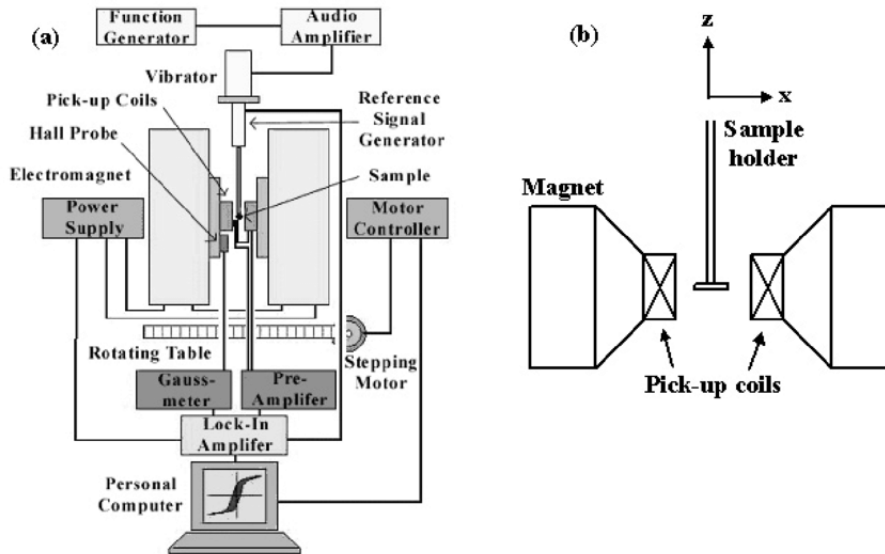


**Figure 4.12:** (a) System diagram of a Vibrating Sample Magnetometer. (b) External close up view of the alignment sample with the magnetic field [106].

## 4.3 Experimental Procedure

### 4.3.1 Materials Synthesis

The experimental setup of the sample synthesis is shown in Figure 4.13. The prepared aqueous solutions of magnetic salts were titrated with a precipitating agent (NaOH) with approximately one drop per 15 s under a monitored pH range and continued vigorous stirring. The solutions precipitate immediately partially changed colour after the addition of a drop of the precipitant and are brought to reaction temperature before washing, drying, and annealing. Three ferrite nanoparticles i.e.

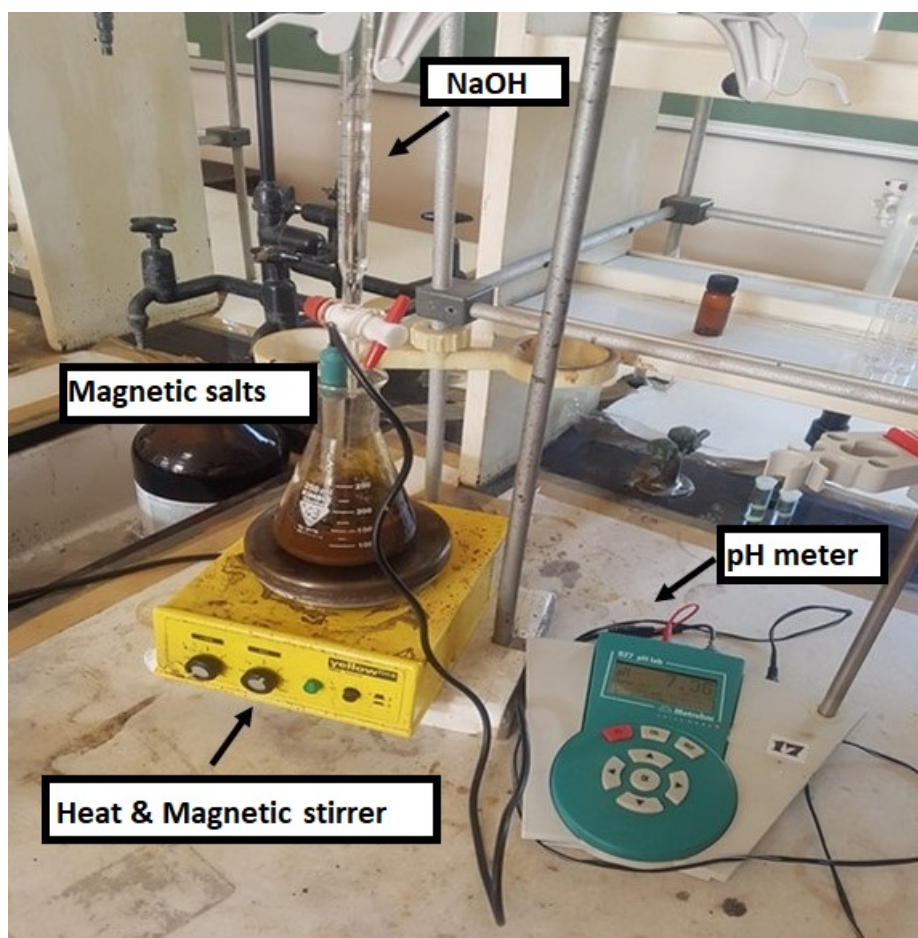


**Figure 4.13:** Schematic assembly of experimental synthesis in the laboratory.

Magnetite ( $\text{Fe}_3\text{O}_4$ ), Cobalt-ferrite ( $\text{CoFe}_2\text{O}_4$ ), and Nickel-ferrite ( $\text{NiFe}_2\text{O}_4$ ) were synthesized using a method of co-precipitation in the presence of an appropriate salt and a base [107]. A 3.00 M solution of the base, sodium hydroxide (NaOH), was prepared by vigorously stirring 3.00 g of NaOH granules in 25.0 mL of de-ionized water for 5 min at room temperature. An aqueous solution of cobalt-chloride hexahydrate ( $\text{CoCl}_2 \cdot 6\text{H}_2\text{O}$ ) (1.189 g, 25.0 mL), ferrous-chloride hexahydrate ( $\text{FeCl}_2 \cdot 6\text{H}_2\text{O}$ ) (1.188 g, 25.0 mL), and nickel-chloride hexahydrate ( $\text{NiCl}_2 \cdot 6\text{H}_2\text{O}$ ) (1.188 g, 25.0 mL) were left to stir for 5 min, before the addition of aqueous solution of ferric-chloride anhydrous ( $\text{FeCl}_3$ ) (1.622 g, 25.0 mL) to each salt, respectively. The resulting aqueous

solutions were left to stir for 15 min. While stirring, NaOH was added drop-wisely to the salts to achieve a pH of the range 11 - 12. Thereafter, 3 drops of surfactant (Oleic acid) were added and the reaction was left to stir further for 1 h at 80 °C. The obtained precipitate was washed thoroughly with ethanol and de-ionized water, then dried in oven at 90 °C for 24 h before annealing at 600 °C for 10 h.

The wet-chemical (co-precipitation) synthesis route yielded successful results of the samples to be characterized. Figure 4.14, shows the powdered samples where (a)

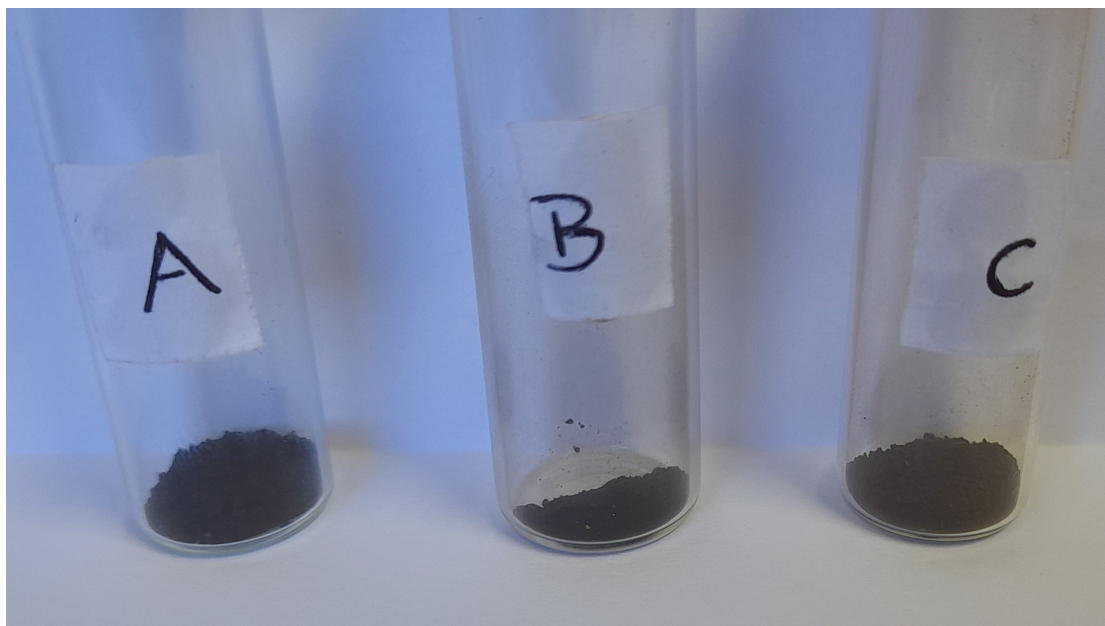


**Figure 4.14:** Synthesized powdered samples (a) Magnetite, (b) Cobalt-ferrite, and (c) Nickel-ferrite.

magnetite and (b) cobalt-ferrite are black and (c) nickel-ferrite is dark brown. The colour of the final product of the samples matched that observed during the synthesis addition of the precipitant, additionally, the colour matched well with those synthesized in the literature [56, 108, 109].

### 4.3.2 Characterization

**X-ray Diffraction:** The structural properties and phase identification of the three samples were investigated by X-ray diffraction (XRD) using a D8 Advance Diffractometer with a copper tube (Cu) of wavelength  $\lambda = 1.5306 \text{ \AA}$  and tube voltage 40 kV. Phase identification performed using the software (ICDD: PDF database 1999 data evaluation: EVA software from Bruker). Crystallites sizes were estimated from XRD data using the Williamson-Hall plot method.

**Transmission Electron Microscopy:** The particle size and morphology were investigated by TEM measurements using were performed using a JEOL 1400 operated at 200 kV electron accelerating voltage for a conventional transmission electron microscope (TEM) imaging and a JEOL-TEM 2100 operated at 200 kV for a high-resolution TEM imaging. Furthermore, EDX measurements were performed on the

JEOL-TEM 2100 equipped with STEM and EDX detectors for elemental composition analysis. TEM samples were prepared by dispersing a small amount of finely crushed powder in acetone followed by ultrasonication. Then, a drop of the dispersed solution was placed on a carbon coated copper TEM grid.

**Mössbauer Spectroscopy:** Magnetic state of the samples were evaluated using  $^{57}\text{Co}/\text{Rh}$  Mössbauer Spectroscopy (MS) operated at room temperature. A metallic iron foil was used to calibrate the velocity scale of the equipment and all isomer shifts are reported relative to  $\alpha\text{-Fe}$ . The Mössbauer spectra were analysed using Recoil analysis software that can model the Mössbauer spectra by a combination of paramagnetic doublets and sextets based on Lorentzian line-profile shape. Information about the Mössbauer parameters (isomer shift, quadrupole splitting, magnetic hyperfine field) were then obtained from the fitted spectra. All fitted spectra were plotted on Origin 9.1 graphing software.

**Vibrating Sample Magnetometer:** Saturation magnetization, remenance magnetization, and coercivity were obtained from field dependent M-H magnetization curves. Magnetic hysteresis loops (M-H curves) were collected at temperatures of 10, 50, 100, and 300 K in an external applied magnetic field ranged from  $\pm 2 \times 10^4$  Oe with PPMS-12T vibrating sample magnetometer (VSM). Temperature dependent magnetization measurements were recorded with an applied field of  $H = 500$  Oe in zero-field-cooled (ZFC) and field-cooled (FC) condition in the temperature range 4 - 300 K.

# Chapter 5

## Results and Discussion

### 5.1 Magnetite Nanoparticles

#### 5.1.1 X-ray Diffraction

The synthesized  $\text{Fe}_3\text{O}_4$  sample was first characterized by XRD for phase identification, and the XRD pattern of the sample is shown in Figure 5.1. The XRD pattern shows that the sample is well crystallized with a face-centered cubic spinel  $\text{Fe}_3\text{O}_4$  structure as reported by Szotek et al.[12]. The sample exhibited 8 distinct peaks corresponding to the (220), (311), (400), (422), (511), (440), (620), and (533) XRD reflection planes. This results are also in good agreement with the reflection planes for  $\text{Fe}_3\text{O}_4$  according to the standard JCP2\_19-0629 ICDD database. The XRD pattern shows significantly broad peaks compared to the bulk  $\text{Fe}_3\text{O}_4$ , indicating the formation of nanocrystallites in the sample. According to Scherrer's equation, the broadening of the XRD peak is mainly due to the small size of the crystallites, the smaller is the crystallites, the broader is the XRD peak. The XRD pattern was

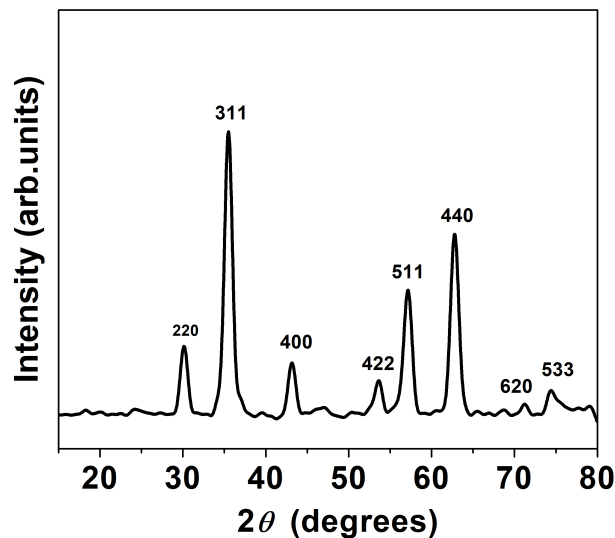
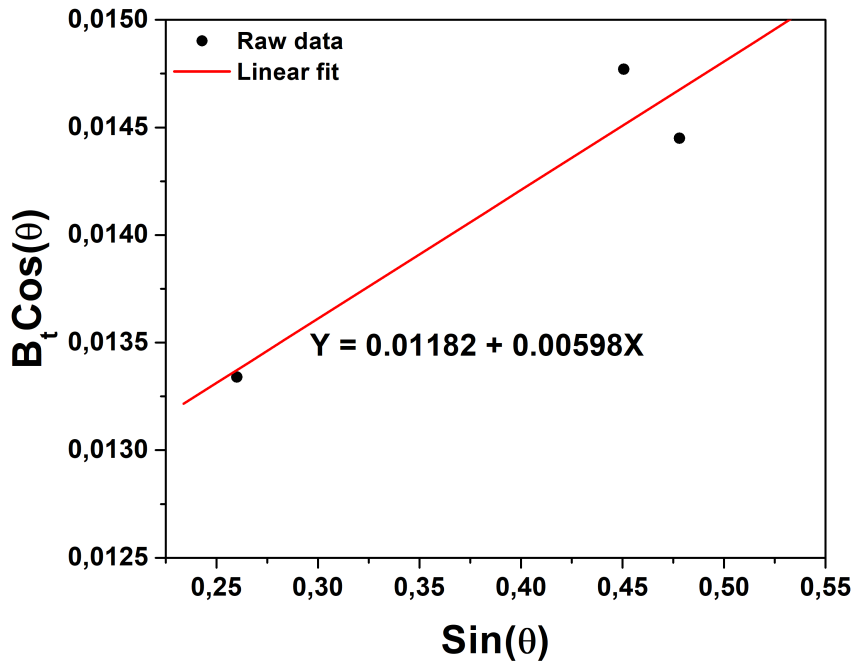


Figure 5.1: XRD pattern of a powdered  $\text{Fe}_3\text{O}_4$  sample.



used to estimate the crystallite size using the Williamson-Hall (W-H) plot method according to Equation (4.7). Figure 5.2 shows (W-H) plot for the  $\text{Fe}_3\text{O}_4$  sample obtained from XRD results. The goodness of the linear fit was determined by the correlation coefficient,  $R$ , the value of  $R$  must be close to unity but any value greater than 0.8 is generally considered as strong, and  $R$  value less than 0.5 is described as weak correlation [72]. For this particular sample, the (W-H) plot yielded a good correlation coefficient of  $R = 0.946$ . The plots' parameters  $y$ -intercept and gradient were used to determine the mean crystallite size of  $D = 11.7$  nm and the dimensionless intrinsic micro-strain  $\epsilon = 1.42 \times 10^{-3}$ , respectively. As expected from the broaden XRD peaks, the mean crystallite size is significantly small, close to the 10 nm crystallite size where  $\text{Fe}_3\text{O}_4$  becomes superparamagnetic. A positive micro-strain is reportedly to indicate lattice expansion while negative micro-strain indicates lattice compression, the observed positive micro-strain in this sample would suggests the expansion of lattice in the  $\text{Fe}_3\text{O}_4$  nanoparticles. It is noteworthy noticing that the fitted straight line did not intercepts all the points on the (W-H) plot, an indication of non-uniform crystallite size distribution and micro-strain in the sample. It has been reported that a best line fit i.e. a straight line that is a best approximation of the given set of data on the (W-H) plot indicates that the sample has homogeneous particle size distribution and micro-strain [110]. The outlier points were handled in Origin-Lab by masking these data points.



**Figure 5.2:** Williamson-Hall plot for Magnetite nanoparticles for mean crystallite size and micro-strain determination.

### 5.1.2 Transmission Electron Microscope

The morphology and particle size distribution of magnetite nanoparticles were examined using TEM measurements. Figure 5.3 (a) shows a bright field (BF) TEM image of the sample and Figure 5.3 (b) presents the corresponding particle size distribution histogram determined from the BF TEM image. A large number of  $\text{Fe}_3\text{O}_4$  nanoparticles with some degree of agglomeration in spherical shape were observed, agglomeration has been associated with the small size of the particles and high surface energy [111]. The nanoparticles in this work were less agglomerated compared to these reported by Yazdani and Edrissi [111], this is due the addition of oleic acid ( $\text{C}_{18}\text{H}_{34}\text{O}_2$ ) as a surfactant during the synthesis of the nanoparticles in this work. Because of their electrostatic repulsion and steric hindrance properties, surfactants are believed to play a significant role in reducing agglomeration of magnetic nanoparticles [112].

Particle size analysis on the BF TEM image was performed using ImageJ software. Areas of non-agglomerated particles were selected from the BF TEM image and particle size was estimated by manually measuring individual particles using line tool on ImageJ. A number of individual particles were measured, and the particle size distribution histogram with a Gaussian fit is presented in Figure 5.3 (b). The results shows nanoparticles with a mean particle size of 14.20 nm, which is in good agreement with the crystallite size determined from the (W-H) plot method. The agreement between crystallite size obtained from the (W-H) plot method using XRD data and particle size obtained from TEM suggests that each measured individual nanoparticle from the TEM image is made of single crystallite. The estimated particle size from both XRD and TEM for the  $\text{Fe}_3\text{O}_4$  nanoparticles is smaller than the reported critical domain size ( $d_{SD}$ ) of approximately 25 to 80 nm for  $\text{Fe}_3\text{O}_4$  nanoparticles [61], indicating a single-domain structure for all the particles in this sample.



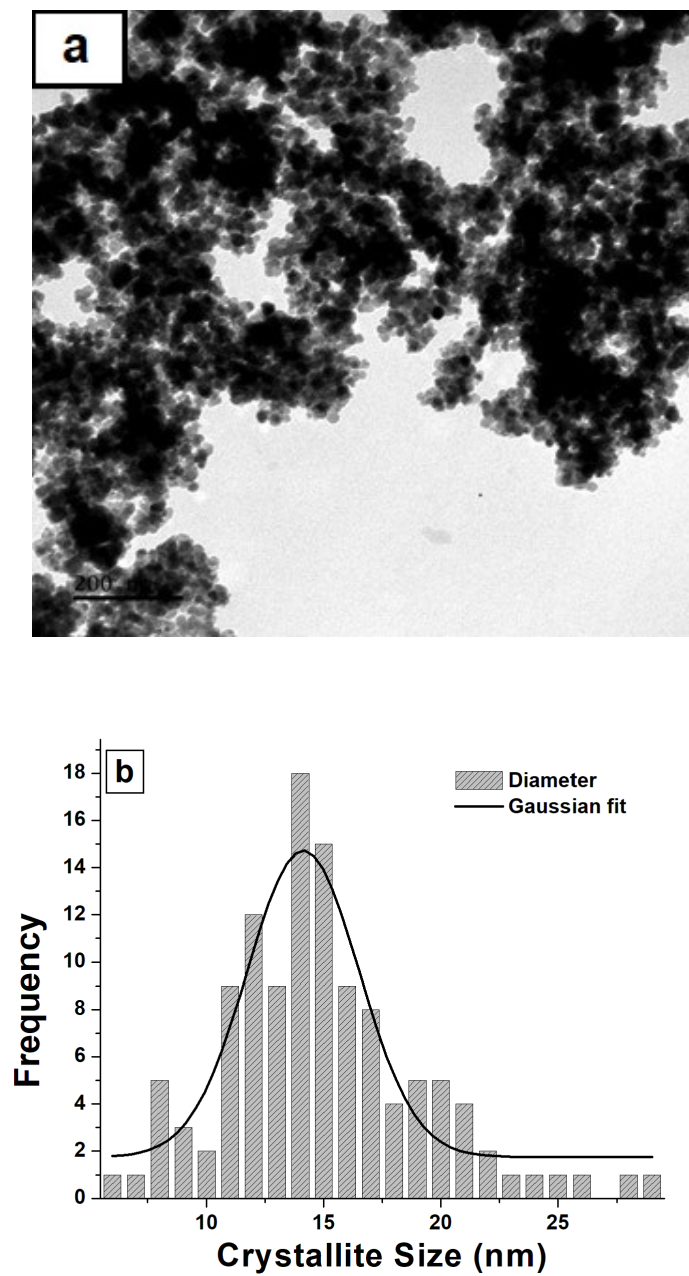


**Figure 5.3:** (a) Magnetite nanoparticles from TEM and (b) the mean diameter distribution.

### 5.1.3 Mössbauer Spectroscopy

The magnetic state of the synthesized magnetite nanoparticles was analysed by Mössbauer spectroscopy (MS). Room temperature Mössbauer spectrum of  $\text{Fe}_3\text{O}_4$  nanoparticles with fittings is presented in Figure 5.4. The spectrum shows a magnetically ordered state with two superimposed sextets due to the contribution of iron ions (divalent ( $\text{Fe}^{2+}$ ) and trivalent ( $\text{Fe}^{3+}$ ) in different crystallographic (A and B) sites. The MS spectrum was accordingly fitted with two Lorentzian sextets corresponding to tetrahedral A-sites occupied by  $\text{Fe}^{3+}$  ions and octahedral B-sites occupied by half of  $\text{Fe}^{3+}$  and  $\text{Fe}^{2+}$  ions. In Figure 5.4, the outer sextet was attributed to  $\text{Fe}^{3+}$  in tetrahedral sites and the inner sextet was assigned to  $\text{Fe}^{3+}$  and  $\text{Fe}^{2+}$  in octahedral sites. The Mössbauer parameters from this fit are listed in Table 5.1. The results are consistent with that of pure magnetite previously reported in literature [113].

It was expected that the Mössbauer spectrum for our sample would at least show some form of superparamagnetic behaviour because ferro- or ferrimagnetic nanoparticles of particle sizes in the range 10-20 nm exhibit superparamagnetic behaviour above blocking temperature,  $T_B$  [114]. However, the room temperature MS spectrum of the sample studied in this work showed a slow relaxation time of magnetization i.e. blocked state as evidenced by the Zeeman sextet. It is not uncommon to observe magnetically ordered state for nanoparticles even below 10 nm e.g. Winsett et al. [115] reported a Mössbauer spectrum in a completely magnetically ordered state for magnetite and maghemite nanoparticles with particle size of 7 nm. The observation of a magnetically blocked state over superparamagnetic state for their sample was explained as a result of coupling of magnetic moments of individual nanoparticles.

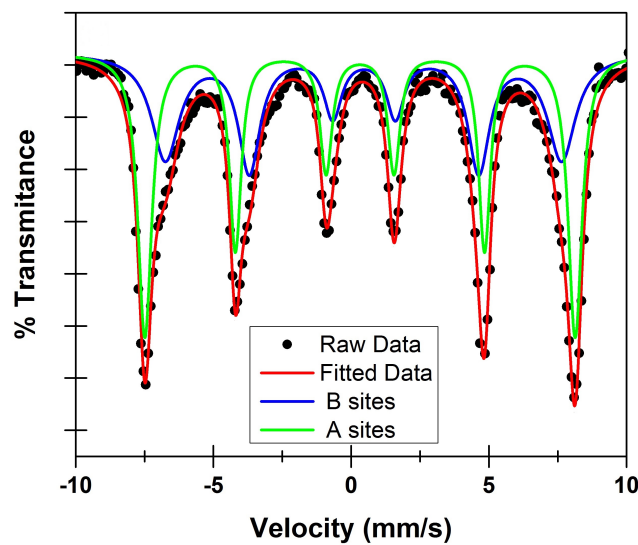


**Figure 5.4:**  $\text{Fe}_3\text{O}_4$  nanoparticles MS spectrum at room temperature.

**Table 5.1:** Mössbauer parameters obtained from the fit of the  $\text{Fe}_3\text{O}_4$  MS spectrum.

Sextet	IS (mm/s)	QS (mm/s)	$B_{hf}$ ( $\times 10^4$ Oe)	A (%)
A-sites	0.321	-0.0095	48.44	57.3
B-sites	0.463	-0.00066	44.60	43.4

### 5.1.4 Vibrating-Sample Magnetometer

The magnetic properties of the  $\text{Fe}_3\text{O}_4$  nanoparticles were further studied using the VSM technique. Depicted in Figure 5.5 is the temperature dependence of the zero-field cooled ( $M_{ZFC}$ ) and field cooled ( $M_{FC}$ ) magnetization of the sample recorded in an applied magnetic field  $H = 500$  Oe in the temperature range 4-300 K. In the  $M_{ZFC}$  procedure, the sample is first cooled down to 4 K in the absence of an applied field (zero field cooling), leaving the magnetic moments of each particle frozen in a random direction, hence the lowest magnetization is recorded (see  $M_{ZFC}$  curve in Fig. 5.5). At 4 K, a small magnetic field is then applied but it is still not enough to align the magnetic moments in the direction of the field, and magnetization remains at lowest. The magnitude of the resultant magnetization will depend on the anisotropy of the system, highly anisotropic system will have small resultant magnetization compared to less anisotropic system because the small applied field will not be sufficient to rotate the spins in the direction of the applied field [116]. Magnetization starts to build up in the sample upon heating the sample in the presence of the field, and an increase in  $M_{ZFC}$  magnetization with increase in temperature is observed until  $M_{ZFC}$  shows a broad maximum (cusp) at centered around 225 K followed by a small decrease in magnetization. This is a typical behaviour for soft magnetic materials [117]. The temperature where the  $M_{ZFC}$  curve is a maximum is known as the blocking temperature ( $T_B$ ) (this temperature is clearly shown by the inset to Fig. 5.5 for the  $\text{Fe}_3\text{O}_4$  sample). In typical superparamagnetic systems, the  $M_{ZFC}$  curve shows a well pronounced local magnetization maximum or a cusp at ( $T_B$ ) (see Fig. 2 (b) in reference to Peddis et al. [118]). The presence of the cusp on the  $M_{ZFC}$  curve for this sample therefore reveal the typical superparamagnetic behaviour.

In the  $M_{FC}$  protocol, the sample was cooled in the presence of the same applied field,  $H = 500$  Oe. As expected,  $M_{FC}$  magnetization was observed to increase with decreasing temperature. Another important observation from Figure 5.5 is thermomagnetic irreversibility behaviour in the  $M_{ZFC}/M_{FC}$  curves. Irreversibility behaviour is caused by the blocking and unblocking of magnetic moments in nanoparticles as a result of variation in thermal energy [119]. This results and Mössbauer findings suggests the coexistence of ferrimagnetic and superparamagnetic state in the sample. The  $M_{ZFC}$  and  $M_{FC}$  curves bifurcated from each other at around 285 K, and the temperature where the  $M_{ZFC}$  and  $M_{FC}$  curves separates is called irreversibility temperature ( $T_{irr}$ ) [119, 120]. For a system of mono-dispersed nanoparticles,  $T_B$  and  $T_{irr}$  coincides, and in this case the two temperatures are

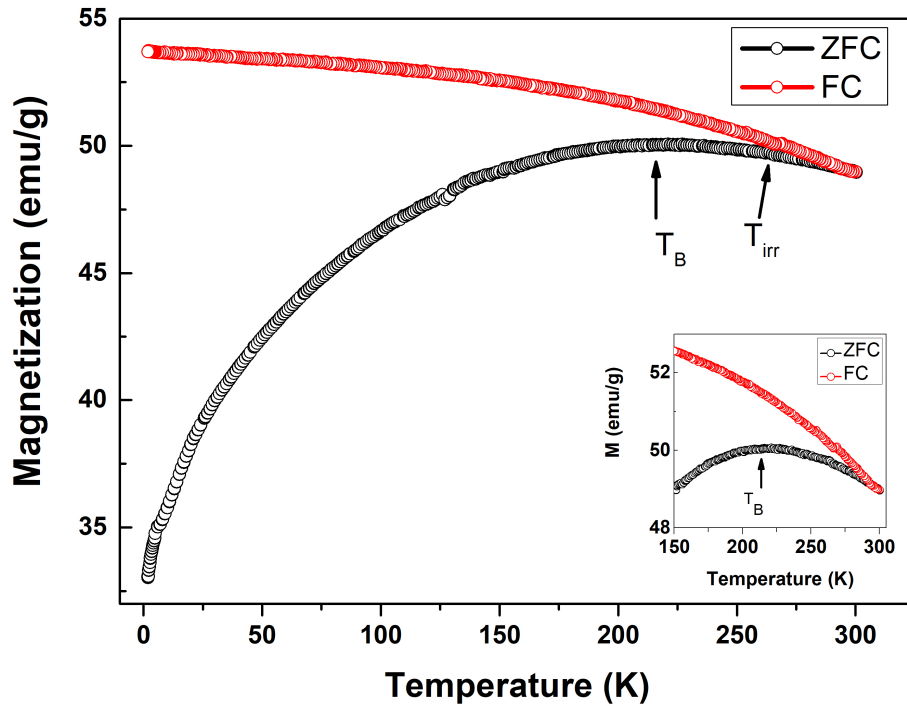


**Figure 5.5:** ZFC/FC magnetization curves measured in an applied field  $H = 500$  Oe for  $\text{Fe}_3\text{O}_4$  nanoparticles.

different, indicating a distribution of particle sizes in the sample in agreement with TEM results. The temperature,  $T_{irr} = 285$  K, corresponds to the blocking of the largest particles in the sample [118].

Field dependent magnetization ( $M$ - $H$ ) data was measured to obtain values of the saturation magnetization ( $M_s$ ), remanence magnetization ( $M_r$ ), and coercivity ( $H_c$ ) for the  $\text{Fe}_3\text{O}_4$  nanoparticles. The ( $M$ - $H$ ) curves recorded in the range  $\pm 2$  T at 10, 50, 100, and 300 K are reported in Figure 5.6. It was observed that all loops were hysteretic and symmetric in the whole temperature range 10–300 K. The hysteretic behaviour shows a ferrimagnetic state of the sample. Furthermore, the "closing" (i.e. reduction in coercivity field) of the loops as temperature is decreased points to the existence of some superparamagnetic behaviour. Exchange interaction between spin moments is reduced as temperature is increased, as a result of additional thermal activation energy [71]. It should be mentioned that a sample that has got all its particles in a superparamagnetic state will show an  $M$  vs  $H$  curve with the absence of both coercivity ( $H_c = 0$ ) and remanent magnetization ( $M_r = 0$ ) i.e. an  $M$  vs  $H$  that does not exhibit hysteresis and passes through the origin [121, 122]. The small loop even at room temperature and the "opening" of the loop with decrease in temperature also indicated the presence of particles in both "blocked" and "unblocked" state in the  $\text{Fe}_3\text{O}_4$  sample considered in this work.

The Singular Point Detection (SPD) method was used to determine whether the loops were major (saturated) or minor (unsaturated) [123]. The method seeks to detect singularities (i.e. a singular point where the two branches overlap) by analyzing the successive derivatives  $d^n M/d^n H$  (where  $n = 1, 2, \dots$ ). A loop is then said to be saturated if such singularity exists. In this work, the derivatives  $dM/dH$  were taken and the results are presented in Figure 5.7. In all cases (10–300 K), the ascending and descending branches for negative fields overlap, indicating that all loops were saturated. The coercivity, saturation magnetization, and the remanence decrease with increasing temperature as reported in Table 5.2.  $H_c$  values were observed to vary between 102 and 35 Oe in the temperature range 10–300 K, typical values for soft magnets. The saturation magnetization values ( $M_s$ ) increased up to approximately 100 emu/g at 10 K from 89 emu/g at 300 K. These  $M_s$  values are close to that of bulk magnetite which is reported in literature to be in the range 86 emu/g [124] to 92 - 100 emu/g [60]. It is well known that the  $M_s$  values in iron oxide nanoparticles are much lower than their bulk counterparts, but recent studies have shown nanoparticles  $M_s$  values close to or equal to that of bulk counterparts e.g. reported by Daoush et al. [125] and Kemp et al. [124].

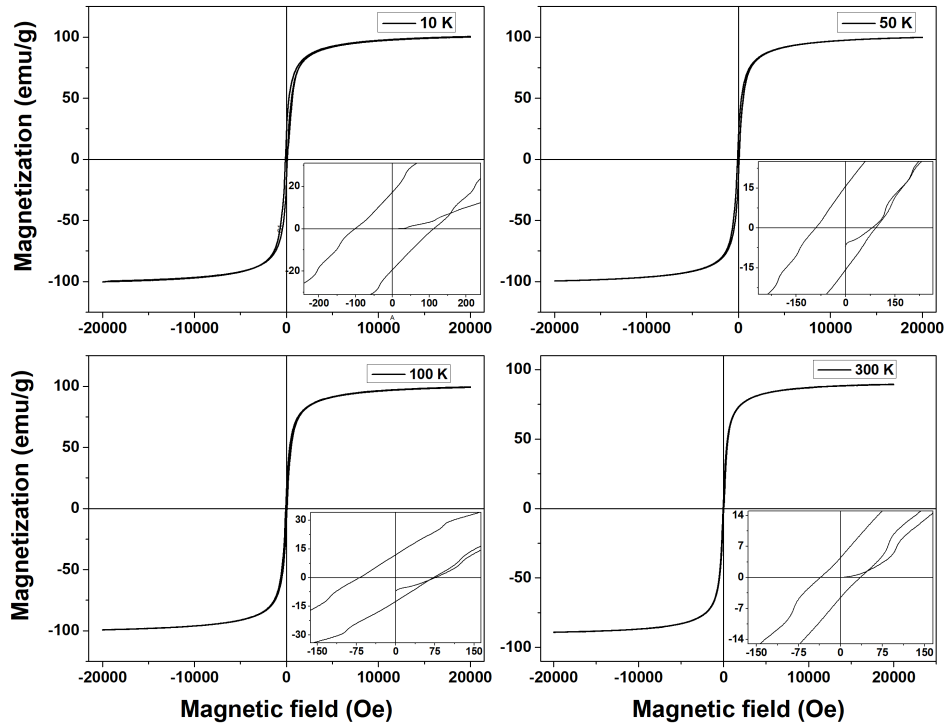
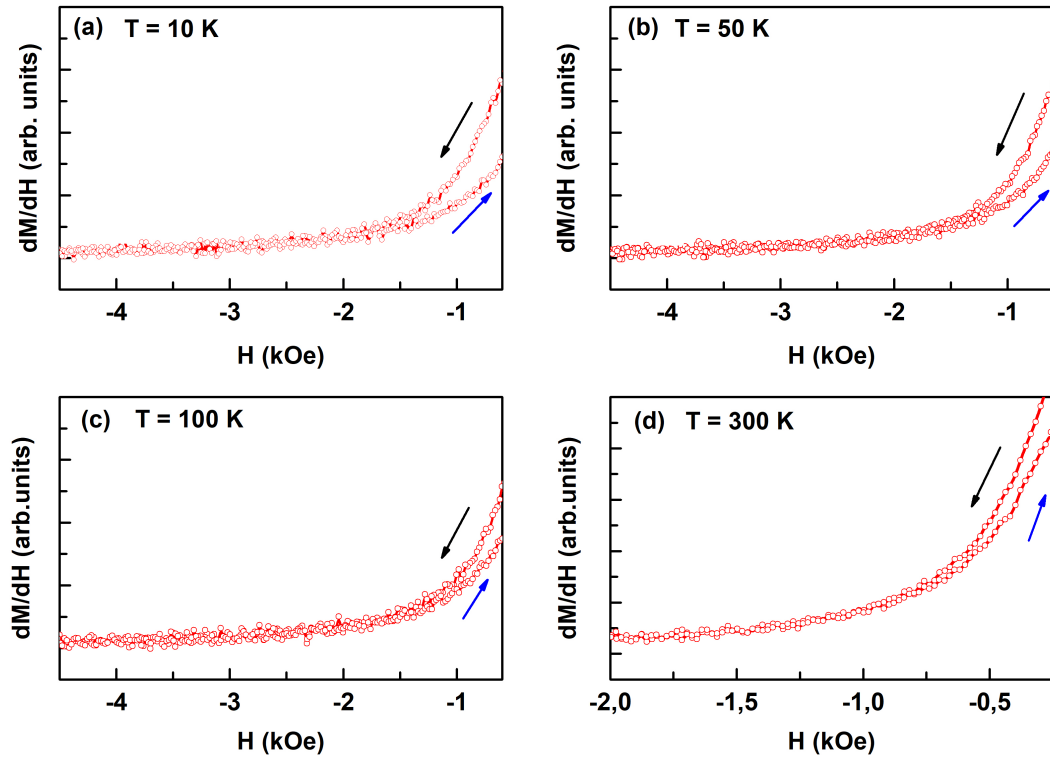


Figure 5.6: Hysteresis loops measured at 10 K - 300 K for  $\text{Fe}_3\text{O}_4$  nanoparticles.



**Figure 5.7:** Derivatives of the respective ascending (blue arrow) and descending (red arrow) branches for negative fields for the  $\text{Fe}_3\text{O}_4$  ( $M$ - $H$ ) curves measured at 10 K - 300 K.

**Table 5.2:** The hysteresis loop data for  $\text{Fe}_3\text{O}_4$  nanoparticles.

T (K)	$M_s$ (emu/g)	$M_r$ (emu/g)	$H_c$ (Oe)
10	100.1	17.18	102.3
50	99.70	15.73	90.71
100	99.41	11.90	69.26
300	89.28	4.479	35.56

## 5.2 Cobalt-ferrite Nanoparticles

### 5.2.1 X-ray Diffraction

The structure and phase composition of the  $\text{CoFe}_2\text{O}_4$  nanoparticles were also investigated using X-ray diffraction technique. The XRD pattern for the sample recorded over the  $2\theta$  range  $20 - 80^\circ$  is reported in Figure 5.8. The observed pattern exhibit the characteristic XRD pattern of  $\text{CoFe}_2\text{O}_4$  (JCP2.79-1744 ICDD database) and it is in good agreement with some of the XRD patterns reported in literature [126]. The XRD peaks were indexed with the inverse spinel structure of  $\text{CoFe}_2\text{O}_4$  (space group:  $Fd\bar{3}m$ ) [50] corresponding to the (111), (220), (311), (400), (422), (511), (440), (620), and (533) planes. The peak broadening of the XRD pattern indicates

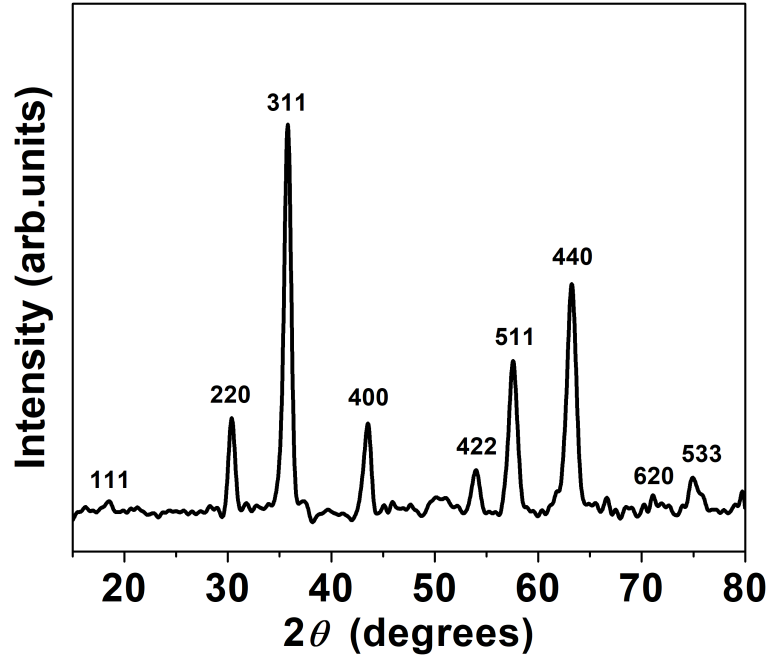


Figure 5.8: XRD pattern of a  $\text{CoFe}_2\text{O}_4$  powdered sample.

the significantly small size of the resulting crystallites compared to bulk magnetite. Similarly to  $\text{Fe}_3\text{O}_4$ , the XRD data of  $\text{CoFe}_2\text{O}_4$  was used to estimate its crystallites size and micro-strain using the (W-H) plot method (Equ. 4.7). The (W-H) plot is reported in Figure 5.9, and a mean crystallite size of  $D = 23.6$  nm and micro-strain  $\epsilon = 3.09 \times 10^{-3}$  were determined from the plot.

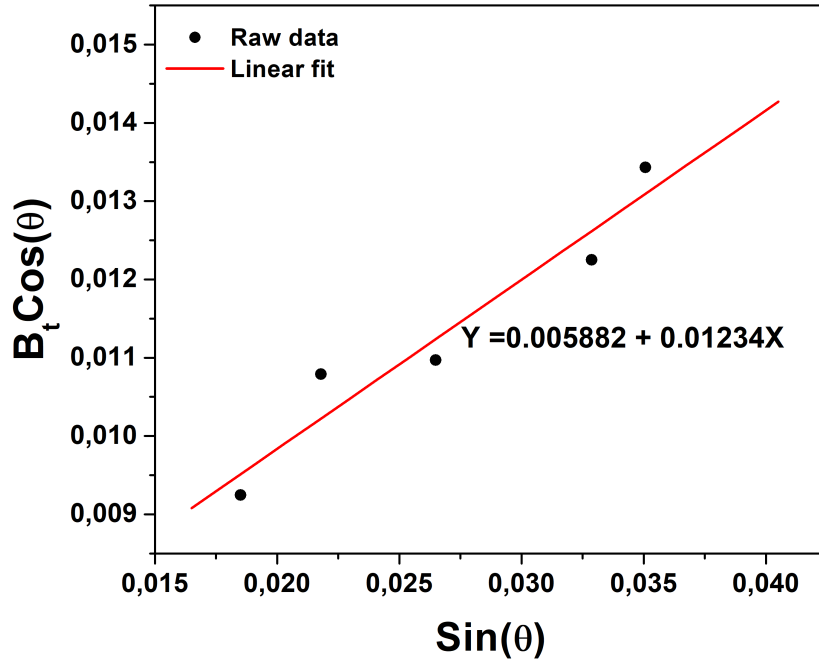


Figure 5.9: (W-H) plot of the  $\text{CoFe}_2\text{O}_4$  sample.

### 5.2.2 Transmission Electron Microscope

Figure 5.10 (a) shows a bright field transmission electron microscope of the  $\text{CoFe}_2\text{O}_4$  sample. Analysis of the TEM image reveals that the nanoparticles have spherical shape with a wide range of particle size distribution. Furthermore, the significant presence of agglomeration of the nanoparticles is observed. However, the TEM image also shows areas with less degree of agglomeration to even separated particles. The agglomeration of nanoparticles was also observed for the  $\text{Fe}_3\text{O}_4$  nanoparticles. Particle size distribution (PSD) information is crucial for the analysis of nanoparticles and PSD histogram for this sample is reported in Figure 5.10 (b). The histogram shows that particle's sizes ranges from 10 nm to 35 nm and the Gaussian fit suggests that it is centered around 19.13 nm. This results are consistent with the crystallite size obtained from XRD data. It is important to note that the calculated particle size for this sample is well below the critical diameter of the magnetic domain for the  $\text{CoFe}_2\text{O}_4$  system, which is experimentally and theoretically reported to be  $d_{SD} = 40$  nm and  $d_{SD} = 100$  nm, respectively [50]. This means that all the particles in the sample have a magnetic single-domain structure.

The crystallinity and crystal structure of the  $\text{CoFe}_2\text{O}_4$  sample was further evaluated using the selected area electron diffraction (SAED) technique. SAED is a one of the TEM modes of operation that allows the observation of a diffraction pattern. The inset to the bright field TEM image in Figure 5.11 represents the SAED pattern for  $\text{CoFe}_2\text{O}_4$ . The diffraction pattern shows the polycrystalline nature of the sample with six ring patterns corresponding to (111), (220), (311), (400), (440), and (511)



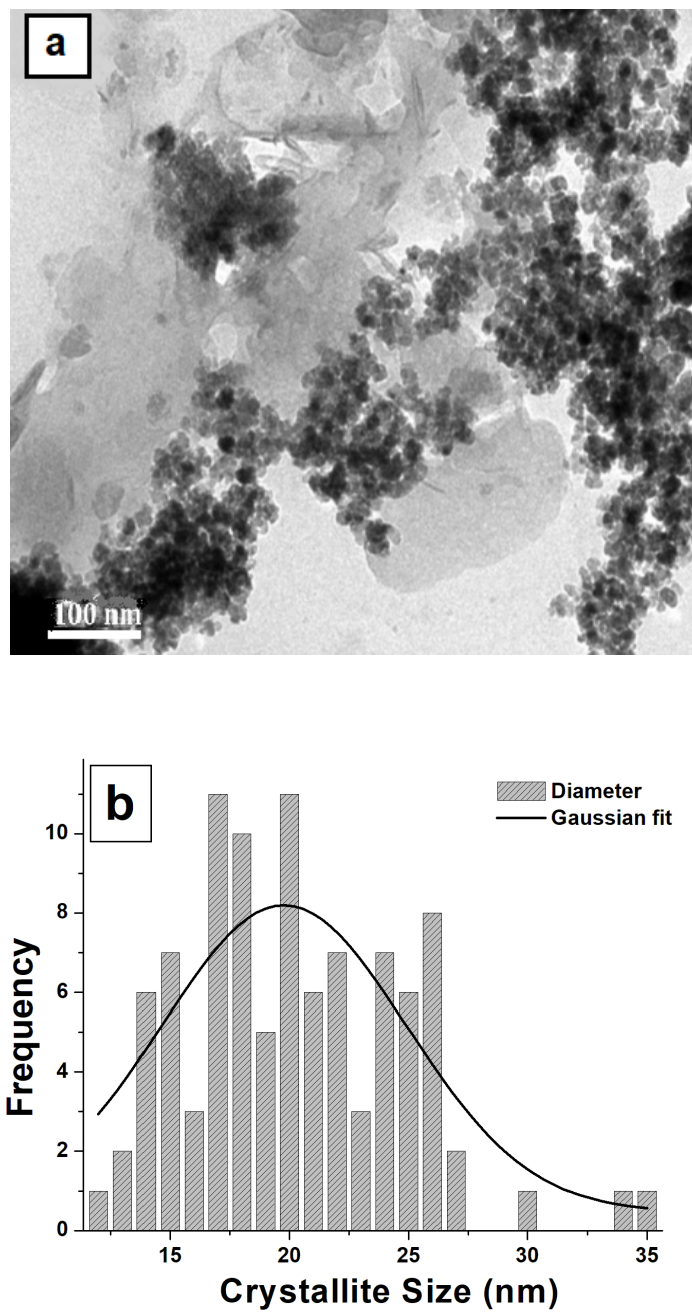


**Figure 5.10:** (a)  $\text{CoFe}_2\text{O}_4$  TEM nanoparticles and (b) mean diameter distribution.

planes, based on calculated  $d$ -spacing, these results are consistent with previously reported XRD results for Co-substituted  $\text{Fe}_3\text{O}_4$  [127].

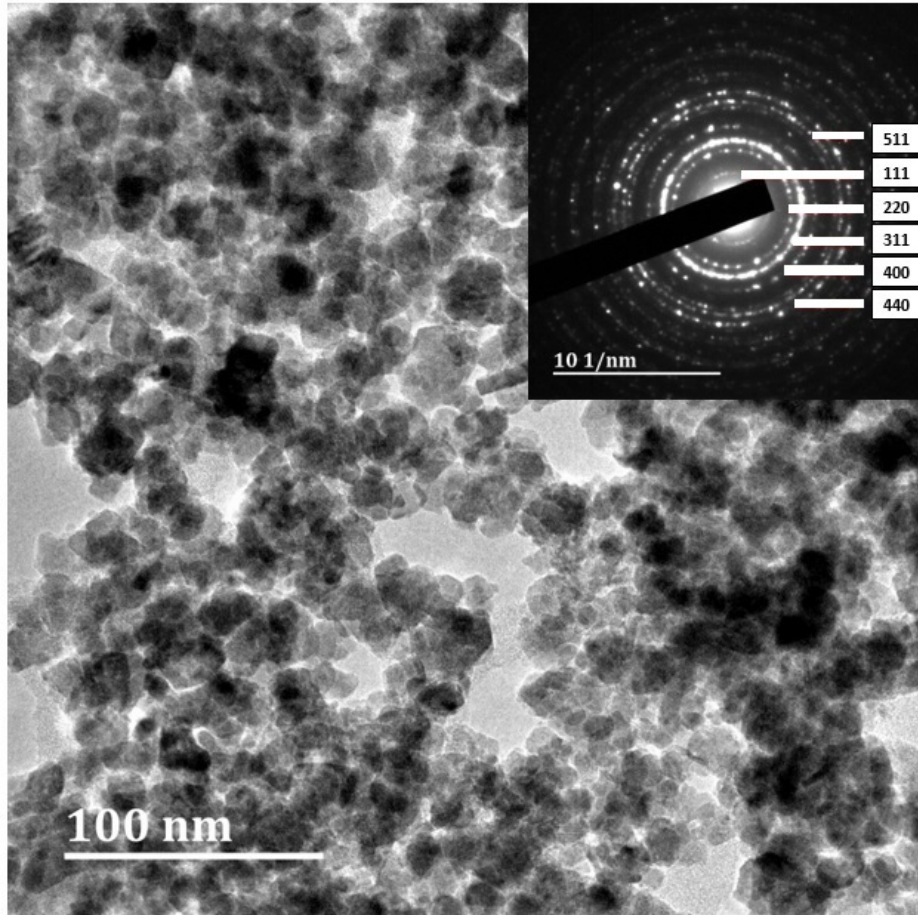


**Figure 5.11:** Bright field  $\text{CoFe}_2\text{O}_4$  TEM images with inset, showing the SAED.

Depicted in Figure 5.12 (a) is the high-resolution transmission electron microscopy (HR-TEM) image of the  $\text{CoFe}_2\text{O}_4$  nanoparticles. The HR-TEM image confirms that the nanoparticles are well crystallized with the lattice fringes clearly visible in Fig. 5.12 (b). The  $d$ -spacing was calculated from the lattice fringes using ImageJ software. Briefly, a fast Fourier transform (FFT) was taken from Fig. 5.12 (b), the brightest spot from the FFT was then selected to re-calculate the lattice fringes. Figure 5.12 (c) shows the re-constructed lattice fringes from Fig. 5.12 (b). The purpose of re-constructing the lattice fringes was to produce clearly visible lattice fringes with high intensity. In the final step, a profile of the lattice fringes from Fig. 5.12 (c) is plotted in Fig. 5.12 (d), where the crests and troughs represents bright and dark fringes, respectively. The  $d$ -spacing is then calculated by dividing the total distance (nm) by the total number of lattice fringes. The determined  $d$ -spacing for the lattice fringes represented in Fig. 5.12 (c) was  $d = 0.473$  nm, which corresponds to the (111) planes. The HR-TEM results are consistent with SAED and XRD which both showed reflections from the (111) planes.

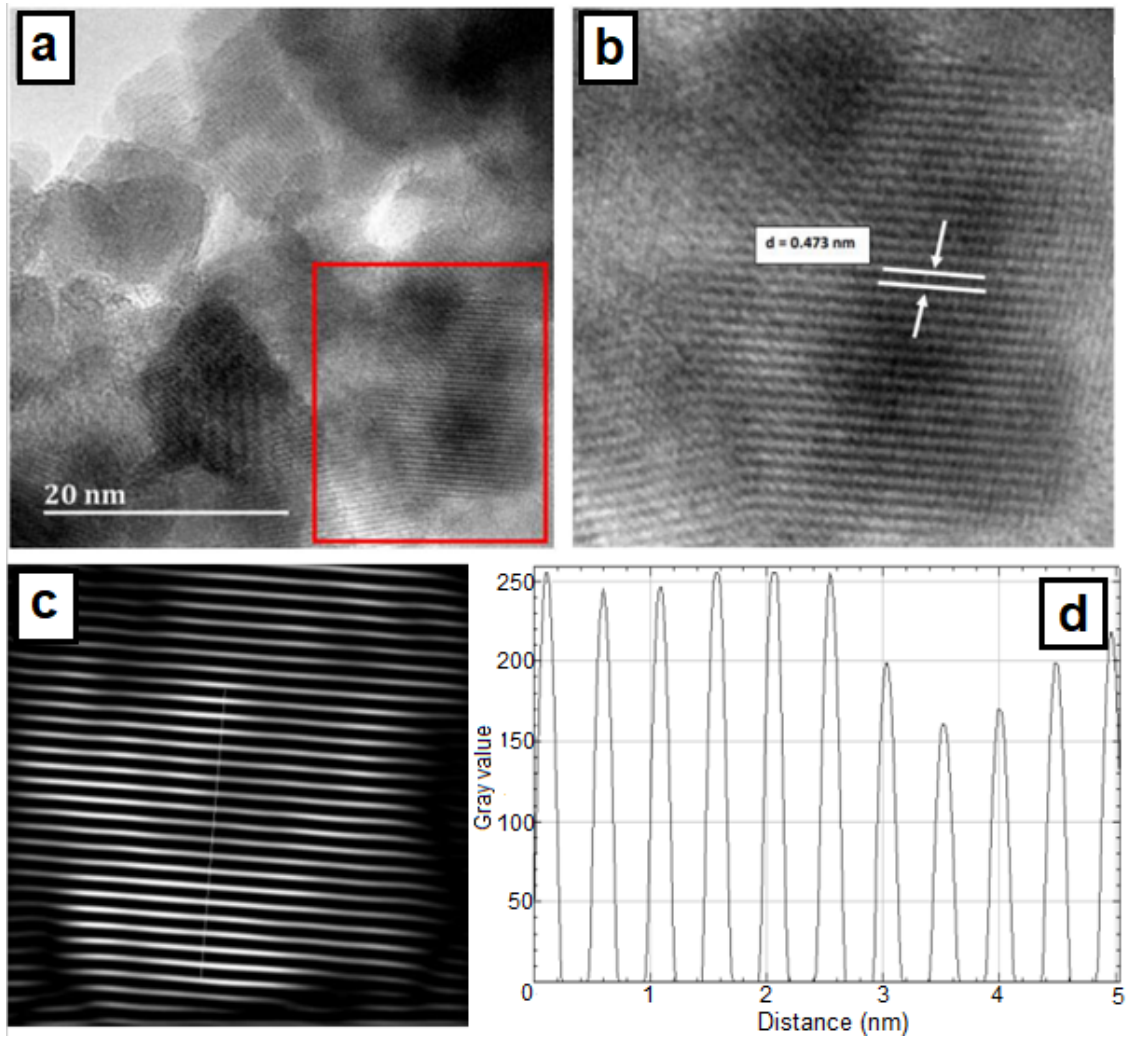


**Figure 5.12:** (a) HR-TEM micrograph of cobalt-ferrite nanoparticles showing lattice fringes, (b) enlarged image of the lattice fringes marked with a red rectangle, (c) re-constructed lattice fringes from (b), and (d) profile of the lattice fringes in (c).

In order to confirm the elemental composition of  $\text{CoFe}_2\text{O}_4$  nanoparticles, energy dispersive x-ray spectroscopy analysis was performed. Presented in Figure 5.13 is the EDX spectrum of the sample showing elemental composition of one of the several areas measured. The inset shows a selected area where the EDX spectrum was measured, and the presence of the main elements Fe (red), O (blue), and Co (green) is clearly observed. Quantitative analysis reveals that the sample is composed of Fe, O, and Co with 46.35 wt%, 27.79 wt%, and 25.86 wt%, respectively (see Table 5.3). The experimentally observed wt% of the sample is in close agreement with the theoretically stoichiometric ratio of 47.06 wt% Fe, 27.28 wt% O, and 25.12 wt% Co for  $\text{CoFe}_2\text{O}_4$ . The obtained results are consistent with the stoichiometric and crystalline  $\text{CoFe}_2\text{O}_4$  phase confirmed by XRD. Additionally, impurities such as Si, Cu, and C were also detected. The copper and carbon signals originated from the carbon coated TEM grid, and the Si signal is due to beam detector screen. As the silicon screen for beam detector was used to convert the electron image to a visible form or scintillator for a charged-coupled device (CCD) camera.

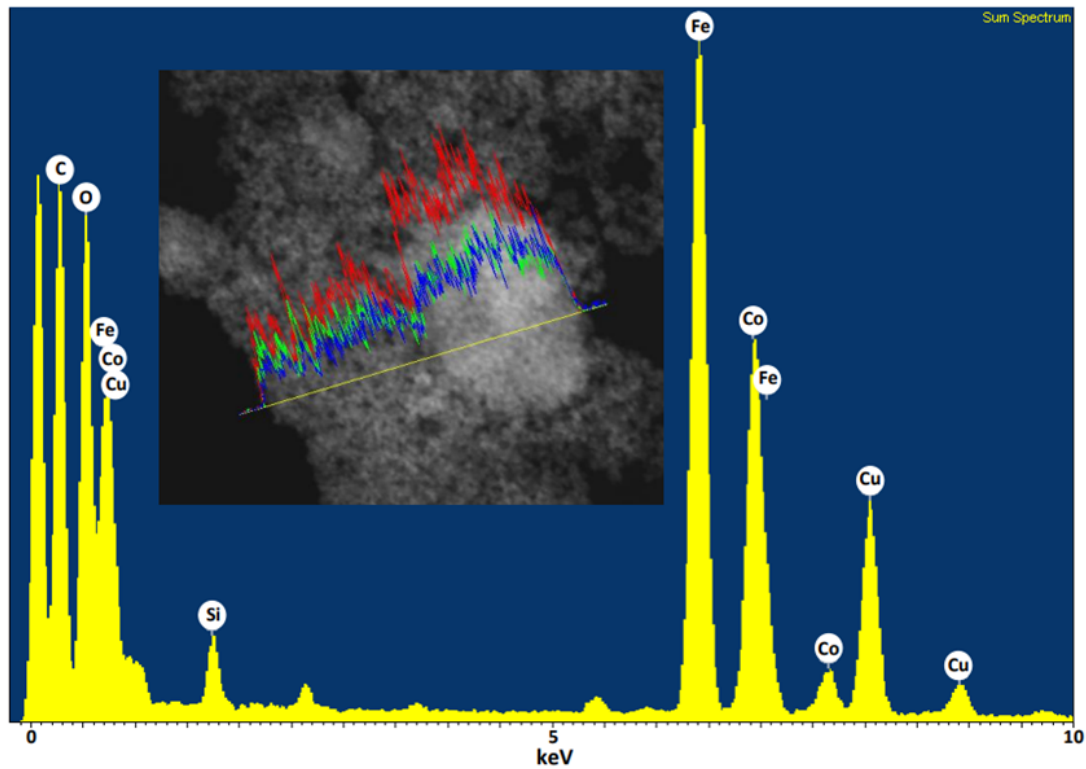


**Figure 5.13:** EDX spectrum of the  $\text{CoFe}_2\text{O}_4$  sample.

**Table 5.3:** The EDX data for  $\text{CoFe}_2\text{O}_4$  nanoparticles.

Area	Element	Weight %
1	Fe	45.38
	O	29.69
	Co	24.93
2	Fe	44.72
	O	28.53
	Co	26.75
3	Fe	48.94
	O	22.14
	Co	28.92
<b>Average</b>	Fe	46.35
	O	26.79
	Co	26.87

Chemical mapping using Scanning Transmission Electron Microscopy (STEM) EDX was performed in order to investigate the elemental distribution in the specimen. This was performed in a TEM operated in STEM mode which uses the beam scanning capabilities and a high-efficiency X-ray detector of the instrument to produce high-spatial-resolution compositional maps [128]. In the STEM EDX procedure, the electron beam is focused to a fine probe which is then raster scanned across the specimen. Atoms in the specimen are excited in the process and X-rays are generated and recorded at each probe position. The EDX spectrum is then used to construct an elemental map [129]. Elemental maps of Fe, Co, and O generated using Fe  $K_\alpha$ , Co  $K_\alpha$ , and O  $K_\alpha$  emission lines for the  $\text{CoFe}_2\text{O}_4$  sample are presented in Figure 5.14. The maps shows a homogeneous distribution of Fe, Co, and O throughout the specimen.

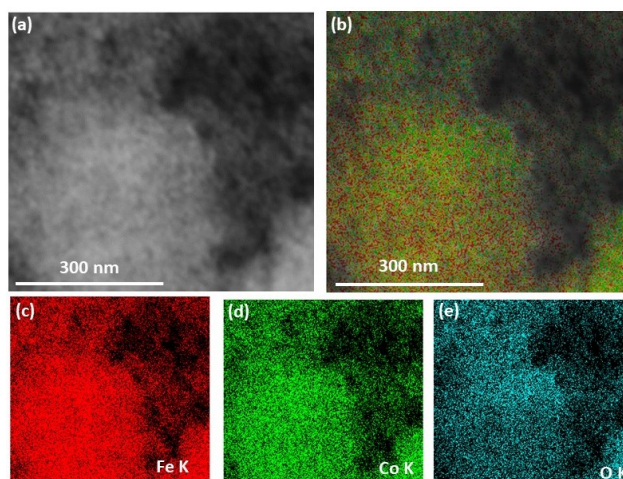


**Figure 5.14:** Surface elemental mapping for  $\text{CoFe}_2\text{O}_4$  nanoparticles. (a) STEM image, (b) elemental map showing distribution of all the elements in the specimen, (c)-(e) individual elemental maps for Fe, Co, and O, respectively.



### 5.2.3 Mössbauer Spectroscopy

The magnetic properties of  $\text{CoFe}_2\text{O}_4$  nanoparticles have been studied by Mössbauer spectroscopy and magnetization measurements. Mössbauer spectrum of the sample recorded at room temperature together with the fitted subspectra is presented in Figure 5.15. The spectrum reveals a mainly magnetically ordered state at room temperature. However, fitting of the spectrum using Recoil analysis software showed that best fit can be achieved by superposition of two sextets due to iron cations in A-sites ( $\text{Fe}^{3+}$ ) and B-sites ( $\text{Fe}^{3+}$ ,  $\text{Co}^{2+}$ ), and a central doublet attributed to a superparamagnetic state. The superparamagnetic behaviour was expected for this sample since XRD and TEM results showed that some particles had sizes that are smaller than the superparamagnetic critical size 10-20 nm to exhibit superparamagnetic behaviour [114]. The Mössbauer spectrum was accordingly fitted with two sextets

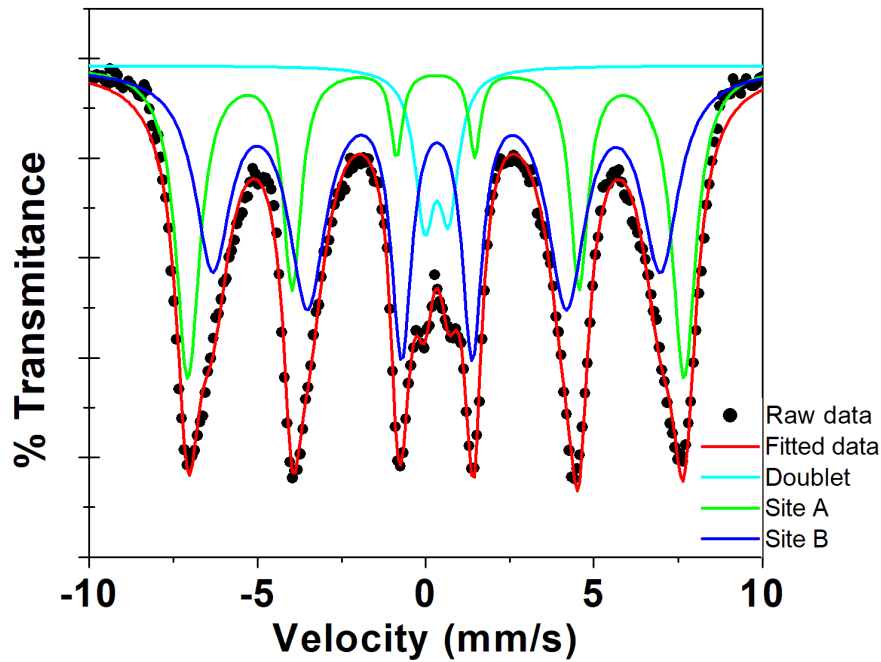


**Figure 5.15:** Mössbauer spectrum of the  $\text{CoFe}_2\text{O}_4$  sample recorded at room temperature.

having isomer shifts (0.2956, 0.3247)  $\text{mm s}^{-1}$ , epsilon (0.000, -0.0078)  $\text{mm s}^{-1}$ , hyperfine field (45.73, 41.27) T. The central doublet was fitted with isomer shift of 0.3272 and quadrupole splitting of 0.7184, which corresponds to high-spin  $\text{Fe}^{3+}$  ions [130] (see results listed in Table 5.4). This results are in very good agreement with Mössbauer parameters reported by [131]. It is noted that the isomer shifts for the A-and B-sites for the  $\text{CoFe}_2\text{O}_4$  system are almost equal and both corresponds to  $\text{Fe}^{3+}$ . It is important to mention that the octahedral B-sites for  $\text{CoFe}_2\text{O}_4$  are different from the  $\text{Fe}_3\text{O}_4$  B-sites since the  $\text{Fe}^{2+}$  ions in  $\text{CoFe}_2\text{O}_4$  are substituted with  $\text{Co}^{2+}$  ions to form  $(\text{Fe}^{3+})^{\text{A}}[\text{Co}^{2+}, \text{Fe}^{3+}]^{\text{B}}_2\text{O}_4$ . However, it has been reported that the  $\text{Co}^{2+}$  ions are often distributed over both the tetrahedral A-sites and octahedral

B-sites [50]. This should be the reason why the B-sites for pure  $\text{Fe}_3\text{O}_4$  have high isomer shifts ( $\sim 0.64 \text{ mm s}^{-1}$ ) [113] compared to the B-sites ( $\sim 0.3247 \text{ mm s}^{-1}$ ) for  $\text{CoFe}_2\text{O}_4$ .

**Table 5.4:** Room temperature Mössbauer hyperfine parameters of the  $\text{CoFe}_2\text{O}_4$  sample.

Sites	IS (mm/s)	QS (mm/s)	$B_{hf}$ ( $\times 10^4$ Oe)	A (%)
A-sites	0.2956	0.0000	45.73	34.15
B-sites	0.3247	- 0.0078	41.27	58.33
Doublet	0.3272	0.7184	—	7.524

### 5.2.4 Vibrating Sample Magnetometer

Presented in Figure 5.16 is the temperature dependence of low field ( $H = 500$  Oe)  $M_{ZFC}$  and  $M_{FC}$  magnetization recorded in the temperature range 4 – 300 K for the  $\text{CoFe}_2\text{O}_4$  sample. There was no clear cusp observed on the  $M_{ZFC}$  curve of this sample, and the maximum temperature of the measurement seem to coincides with the onset of cusp. This indicates that  $T_B$  is at  $\sim 300$  K or above, which is also the same temperature where  $M_{ZFC}$  and  $M_{FC}$  bifurcated from each other.

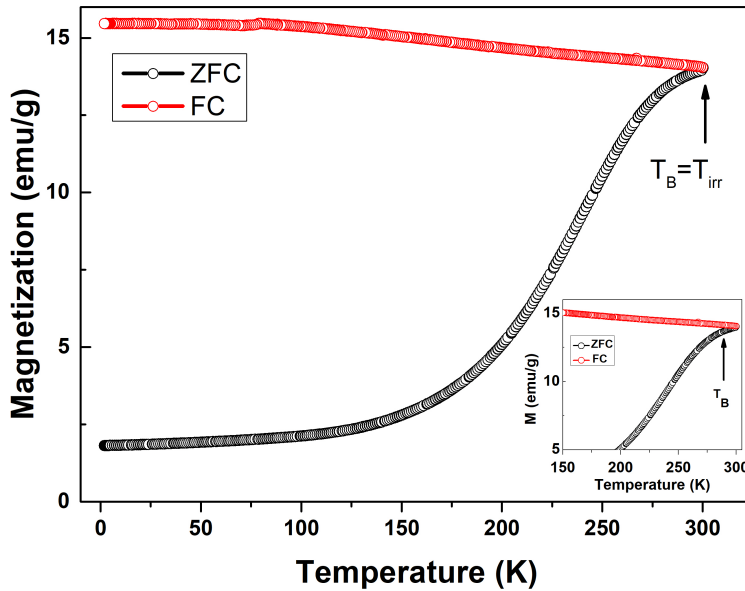


**Figure 5.16:** Magnetization FC and ZFC curves as function of temperature in an applied field ( $H$ ) for  $\text{CoFe}_2\text{O}_4$  nanoparticles.

Mahhoute et al. reported similar value of  $T_B$  for their  $\text{CoFe}_2\text{O}_4$  nanoparticles with average particle size of 11.2 nm [71]. The transition of nanoparticles from the ferrimagnetic to a superparamagnetic state of blocked to unblocked magnetic moments is in good agreement with XRD, TEM, and Mössbauer results.

The field dependence ( $M$ - $H$ ) magnetization measurements for the  $\text{CoFe}_2\text{O}_4$  sample performed up to 20 kOe at 10 K - 300 K are reported in Figure 5.17. It is observed that all the magnetization curves exhibit hysteresis. An S-shaped loop was observed for the  $M$ - $H$  curve measured at 300 K while all three  $M$ - $H$  curves measured at 10, 50, and 100 K revealed wasp-waist hysteresis loops. A wasp-waist hysteresis loop is a loop that is constricted in the middle but is wider above and below the middle [132, 133]. For this sample, a narrowing of the hysteresis loop along the field axis at low applied field is clearly visible on the  $M$ - $H$  curves recorded at 10, 50, 100 K. The SPD method described in subsection 5.1.4 was employed to determine if the loops achieved saturation magnetization with the maximum applied field  $H = 20$  kOe. The plots of the derivatives  $dM/dH$  vs  $H$  for the negative fields are reported in Figure 5.18. It is noted that the descending and ascending branches for the 10, 50, and 100 K loops did not overlap up to the maximum applied field. This is an indication that these  $M$ - $H$  curves did not achieve saturation magnetization with the maximum applied magnetic field (20 kOe). Since the SPD method pointed out that the loops were minor loops, the narrowing of the loop along the field axis could be attributed to minor loop effects. The saturation magnetization ( $M_s$ ) values were then estimated from the relationship reported by Marquez et al [121, 134]

$$M = M_s(1 - \beta/H) \quad (5.1)$$

where  $\beta$  is a magnetic field-independent parameter. By considering only high field data, plots of  $M$  vs  $1/H$  were obtained and the values of  $M_s$  were determined by extrapolating  $1/H$  to zero field in the experimental data  $M$  vs  $1/H$ . The values of  $M_s$ ,  $M_r$  and  $H_c$  obtained from the hysteresis loops are listed in Table 5.5. The low temperature loops presented high  $H_c$  values up to  $\sim 2.7$  kOe and saturation magnetization up to  $\sim 54$  emu/g. Noticeably, the coercivity field of the Co-doped sample is quite higher than that of pure  $\text{Fe}_3\text{O}_4$ . This indicates the higher anisotropic character of  $\text{Co}^{2+}$  compared to  $\text{Fe}^{2+}$ . The  $\text{Co}^{2+}$  substitution provides a higher degree of anisotropy relative to  $\text{Fe}^{2+}$  and  $\text{Fe}^{3+}$  [16, 112].

In contrast, the 300 K loop reached saturation magnetization and the recorded values of the saturation magnetization and coercivity were  $M_s = 36.86$  emu/g and  $H_c = 116.7$  Oe, respectively. The small coercivity field value at 300 K compared to the large coercivity field obtained from the  $M$ - $H$  curves recorded at low temperatures was expected. This is caused by the decrease in the exchange interaction between spin moments at 300 K as a result of additional thermal activation energy [71]. As the temperature is decreased, the growth of magnetic anisotropy is enhanced and it aligns magnetic moments in a preferred direction. Large magnetic anisotropy will inhibit the alignment of the moment in an applied field [135] hence the large coercivity recorded at low temperatures. The saturation magnetization obtained at 300 K and lower temperatures for this sample were much lower than the saturation



magnetization of 80 emu/g for the bulk  $\text{CoFe}_2\text{O}_4$  system [136]. The small values of  $M_s$  for nanoparticles compared to their bulk counterparts is known and it is often attributed to the magnetic moment disorder at the particle surface [71] and [79]. In the case of the  $\text{CoFe}_2\text{O}_4$  sample in this study, both Mössbauer spectroscopy and VSM measurements revealed the presence of particles in both ferrimagnetic and superparamagnetic state. The reduction in  $M_s$  is attributed to surface disorder of the smaller superparamagnetic particles. The magnetic properties parameters obtained from the hysteresis loops are reported in Table 5.5.

In addition, the magnetic moment,  $\mu_B$  (per formula unit) was calculated from the formula [58, 135]:

$$\mu_B = \frac{M \times M_s}{5585} \quad (5.2)$$

Where  $M$  is molecular weight of  $\text{CoFe}_2\text{O}_4$ . The magnetic properties parameters obtained from the hysteresis loops are reported in Table 5.5.

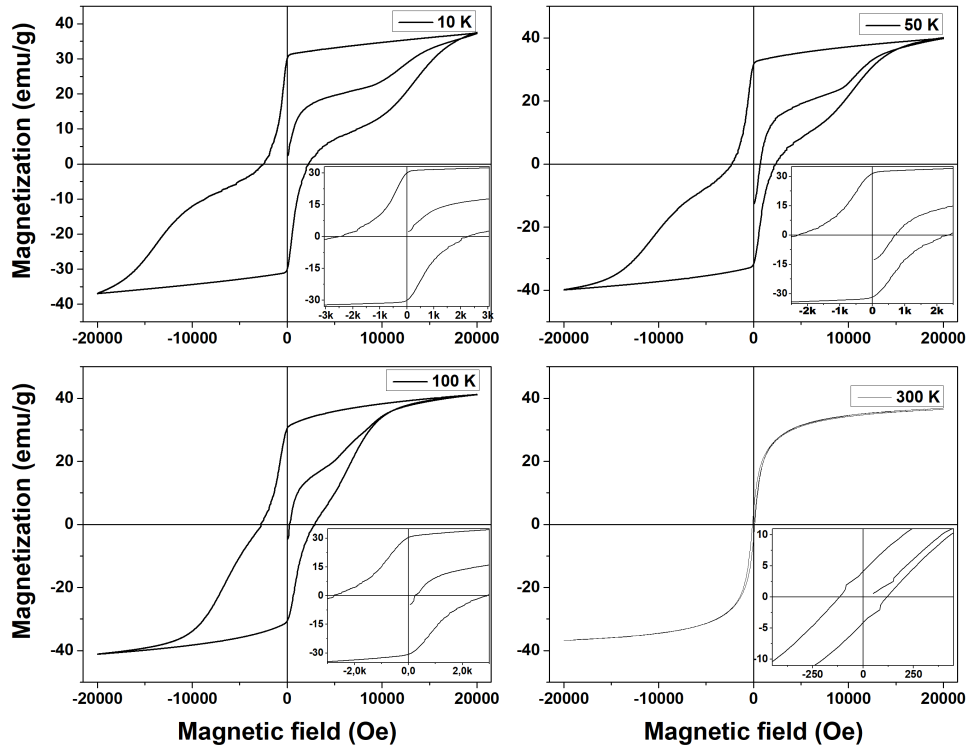


**Figure 5.17:**  $\text{CoFe}_2\text{O}_4$  hysteresis loop, showing the behaviour of magnetization and coercivity at lower and higher temperatures (10 - 300)K

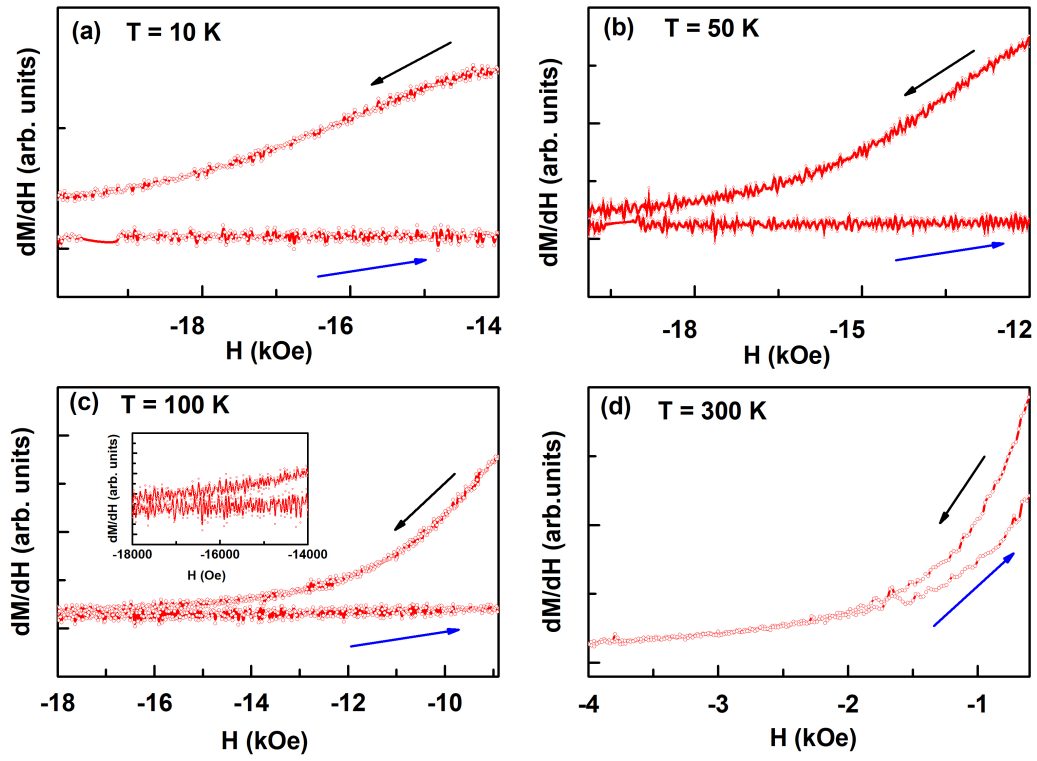


**Figure 5.18:** Derivatives of the respective descending and ascending branches for negative fields for the  $\text{CoFe}_2\text{O}_4$   $M$ - $H$  curves at 10 K - 300 K.

**Table 5.5:** The hysteresis loop data for  $\text{CoFe}_2\text{O}_4$  nanoparticles.

T (K)	$M_s$ (emu/g)	$M_r$ (emu/g)	$H_c$ (Oe)	$\mu_B$
10	51.33	29.93	2 437	1.30
50	53.91	31.48	2 281	1.30
100	47.63	30.49	2 755	1.29
300	36.86	4.146	116.7	1.11

## 5.3 Nickel-ferrite Nanoparticles

### 5.3.1 X-ray Diffraction

Powder X-ray diffraction (XRD) measurements were carried out to investigate the structure and phase composition of the Ni-doped ferrite ( $\text{NiFe}_2\text{O}_4$ ) nanoparticles. Depicted in Figure 5.19 is the measured XRD pattern for the  $\text{NiFe}_2\text{O}_4$  sample. The XRD pattern showed broad XRD peaks, similarly to the  $\text{Fe}_3\text{O}_4$  and  $\text{CoFe}_2\text{O}_4$  XRD patterns presented in sections 5.1.1 and 5.2.1, respectively. The position of the XRD peaks for the sample matched well with the standard XRD pattern for  $\text{NiFe}_2\text{O}_4$  with JCP2 card No. 10-0325, and it is in good agreement with XRD results previously reported by Joshi et al. [137] for  $\text{NiFe}_2\text{O}_4$  nanoparticles. The XRD peaks were therefore indexed to the (111), (220), (311), (222), (400), (422), (511), (440), (620), (533), and (622) reflection planes in a cubic spinel crystal structure belonging to the space group:  $Fd\bar{3}m$  [137].

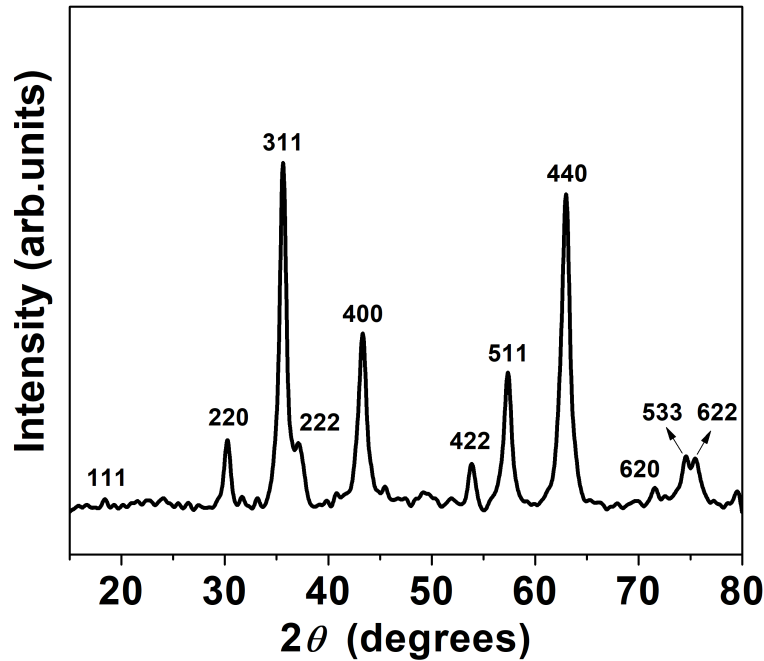


Figure 5.19: XRD pattern of  $\text{NiFe}_2\text{O}_4$  nanoparticles.

The average crystallite size for the  $\text{NiFe}_2\text{O}_4$  sample was also estimated using the (W-H) plot method based on equation 4.7, which considers the broadening of the XRD peaks to be due to both crystallite size and micro-strain effects. Williamson-Hall plot obtained from XRD data of the sample with a good correlation coefficient,  $R = 0.9896$ , is illustrated in Figure 5.20. An average crystallite size  $D = 16.4$  nm and a micro-strain  $\epsilon = 2.34 \times 10^{-3}$  was calculated from the (W-H) plot.

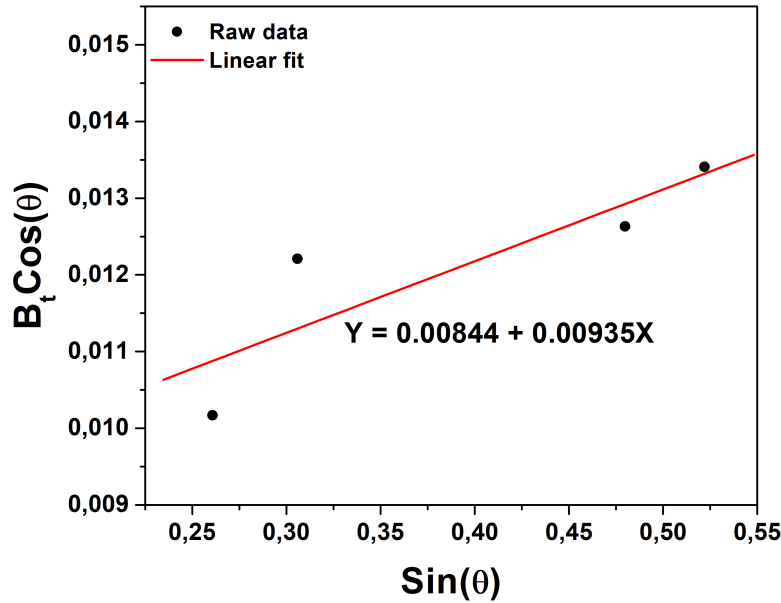
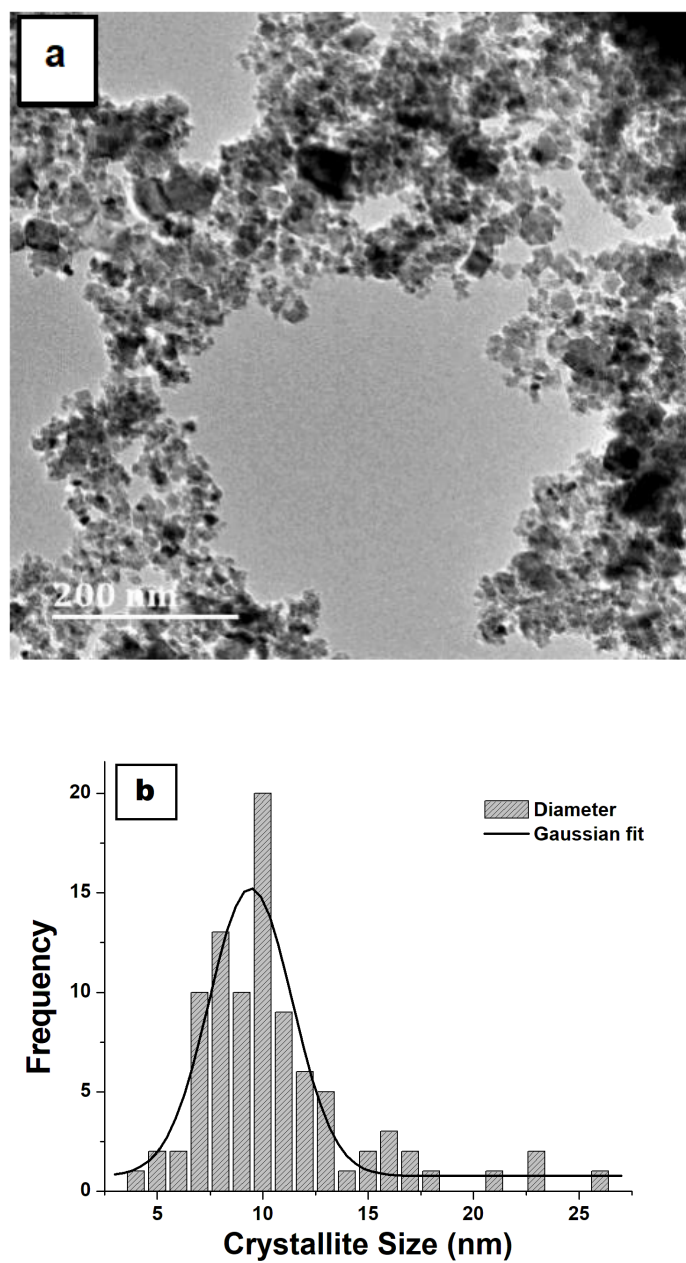


Figure 5.20: Williamson-Hall plot for the  $\text{NiFe}_2\text{O}_4$  nanoparticles.

### 5.3.2 Transmission Electron Microscope

The morphology and particle size distribution of the  $\text{NiFe}_2\text{O}_4$  sample were subjected to a TEM investigation. A bright field TEM image and histogram of particle size for the sample are reported in Figure 5.21 (a) and (b), respectively. The nanoparticles were observed to be approximately spherical in shape with particle sizes in the range 4 – 27 nm. The average particle size diameter derived from the Gaussian fit was approximately 9.2 nm. The average crystallite size estimated from XRD data is well within the range calculated from TEM measurements. The particle size obtained from both TEM and XRD for this sample is well below the reported critical single domain size ( $d_{SD}$ ) of  $\sim 50$  nm for the  $\text{NiFe}_2\text{O}_4$  system [16], confirming that all the particles in the sample have single magnetic domain structure. In addition, the average particle size measured from TEM is below the critical particle size ( $d_{SPM}$ ) of 10 nm where  $\text{NiFe}_2\text{O}_4$  becomes superparamagnetic [79].

Similarly to  $\text{CoFe}_2\text{O}_4$ , selected area electron diffraction (SAED) technique was employed to investigate the crystallinity of  $\text{NiFe}_2\text{O}_4$  sample. A SAED pattern taken from a selected area of the bright field TEM image (Fig. 5.22) is shown as an inset to the figure. The poly-oriented structure of the sample is clearly visible in the SAED ring pattern (Fig. 5.22, inset). It is known that ring patterns are formed when the crystallites in a polycrystalline material are randomly oriented, this happens when the randomly oriented crystallites are illuminated with the electron beam, and their diffraction patterns superimpose forming an image of concentric rings [138]. The  $d$ -spacing of each plane was determined by measuring the distance of each ring from the central bright spot, and associated with each calculated  $d$ -spacing were the following (111), (220), (311), (222), (440), (422), and (511) Bragg reflections planes.



**Figure 5.21:** (a) Bright field TEM image of  $\text{NiFe}_2\text{O}_4$  nanoparticles, (b) Histogram of particle size distribution.

The SAED results are in good agreement with XRD findings from this study and XRD results reported in literature by Joshi et al [137] and Lazarova et al [16].

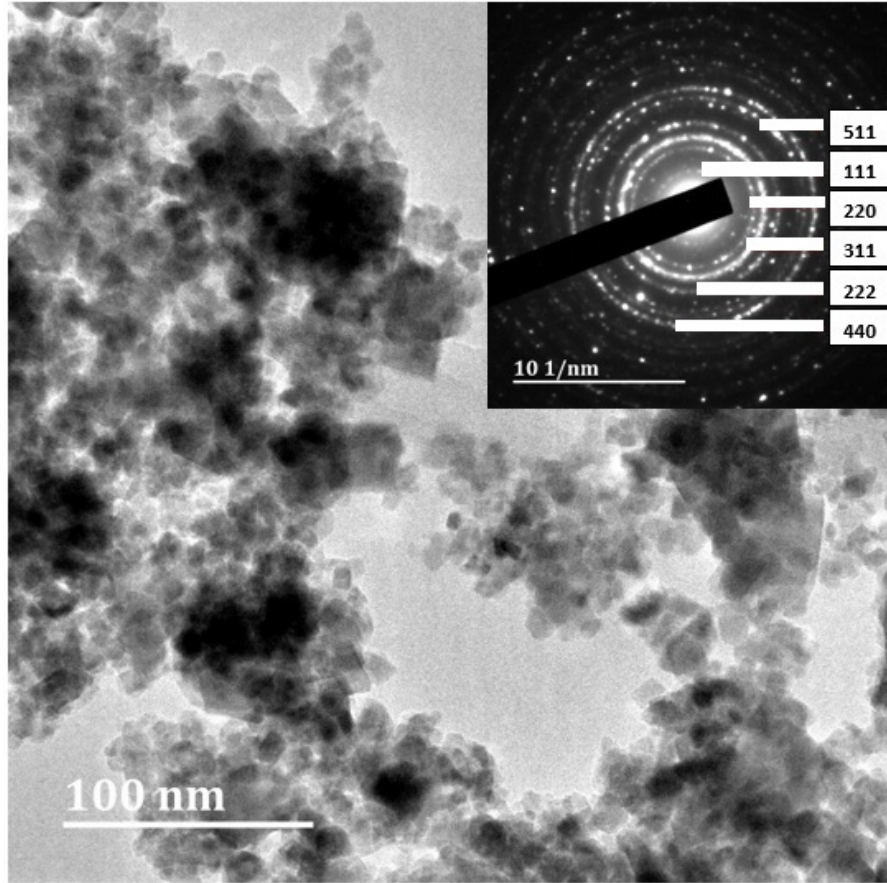


**Figure 5.22:** Bright field TEM image and indexed SAED pattern (inset) of the  $\text{NiFe}_2\text{O}_4$  sample.

HR-TEM micrograph of the sample is presented in Figure 5.23 (a). Lattice fringes from different randomly oriented crystallites are observed. The  $d$ -spacings of the lattice fringes including the one marked with a red rectangle were calculated following the method described on page 49, section: 5.2.2. The images ((b) - (d)) represents the real lattice fringes, re-constructed lattice fringes (inverse FFT), and calculated profile of the fringes, respectively. The lattice  $d$ -spacing is determined from the profile plot and was found to be 0.478 nm and 0.248 nm which corresponded to the (111) and (311) planes for the two set of lattice fringes considered from the HR-TEM image of the  $\text{CoFe}_2\text{O}_4$  sample. The HR-TEM analysis confirms the spinel type crystal structure for the sample, with the two reflection planes i.e. (111) and (311) belonging to  $\text{NiFe}_2\text{O}_4$ .

Elemental analysis by energy dispersive X-Ray spectroscopy (EDX) was used to study the elemental composition of the  $\text{NiFe}_2\text{O}_4$  nanoparticles. Depicted in Figure 5.24 is the EDX spectrum of the sample, with the inset showing the STEM image and corresponding EDX line-scan profile of the main elements Fe (red), O (blue), and Ni



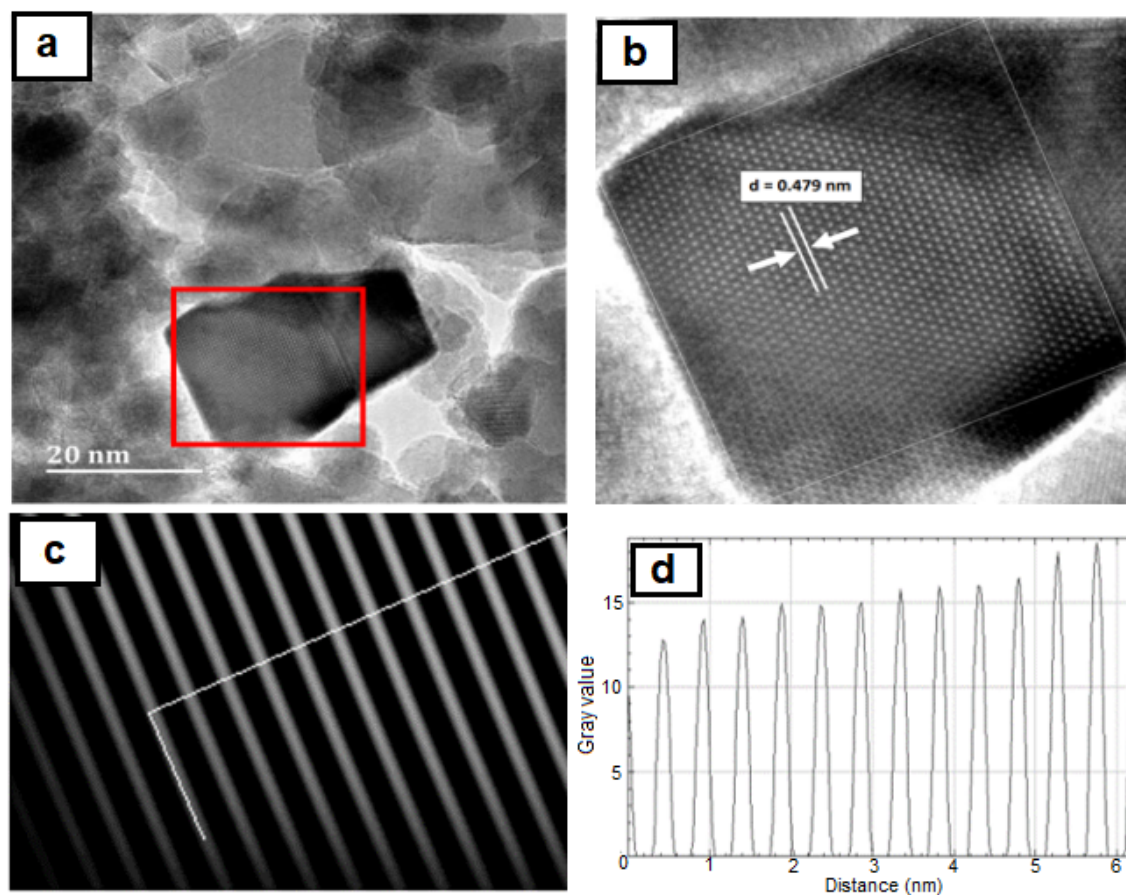


**Figure 5.23:** (a) HR-TEM micrograph of  $\text{NiFe}_2\text{O}_4$  nanoparticles, (b) enlarged image of the lattice fringes marked with a red rectangle in (a), (c) inverse FFT, and (d) profile plot of the inverse FFT.

(green). The EDX spectrum shows the existence of Fe, O, and Ni with an average of 47.02 wt%, 27.27 wt%, and 24.75 wt%, respectively. The EDX quantitative results are listed in Table 5.6. The experimentally calculated wt% is in close agreement with the theoretical weight percent of 47.65 wt% Fe, 27.31 wt% O, and 25.04 wt% Ni for stoichiometric  $\text{NiFe}_2\text{O}_4$ . Indeed, this is consistent with XRD results which confirmed the existence of stoichiometric  $\text{NiFe}_2\text{O}_4$  phase on the sample without additional phases. Additionally, impurities such as Si, Cu, and C were also detected from the sample. The copper and carbon signals originated from the carbon coated copper TEM grid, and the Si signal as discussed on page 51 of section 5.2.2, the electron beam interaction with the silicon contained screen, the sensitivity of HR-TEM equipped with EDX resulted to a minimal amount of Si being picked up. Further evidence of the presence and distribution of elements on the the sample was

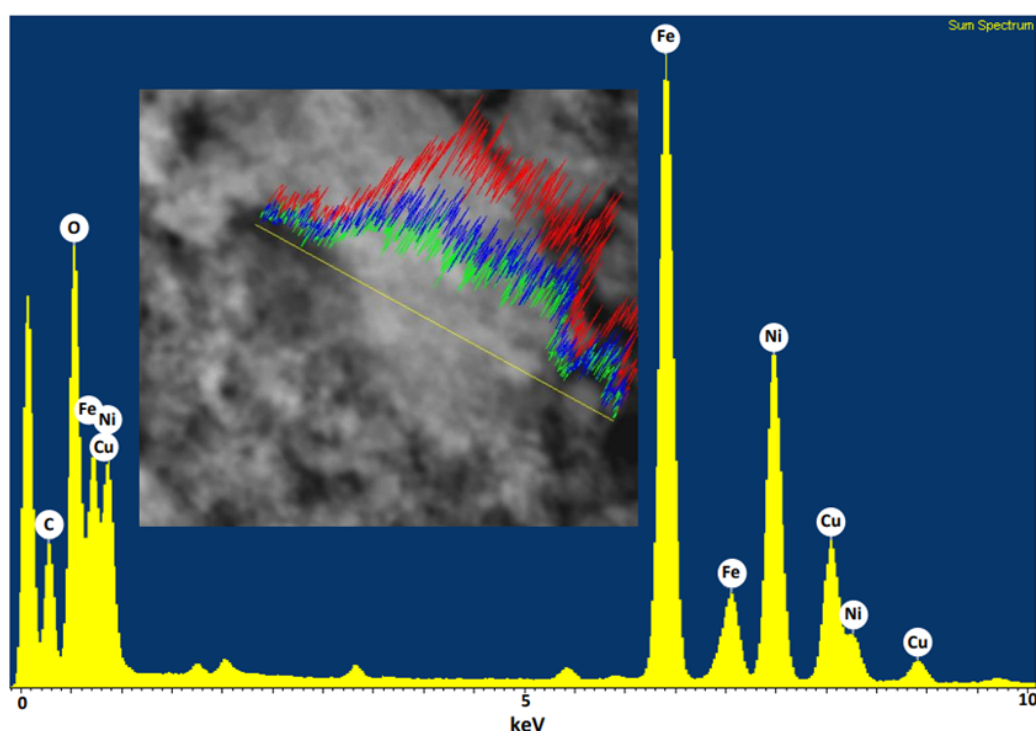


**Figure 5.24:** EDX spectrum of the  $\text{NiFe}_2\text{O}_4$  sample for elemental composition analysis.

obtained from STEM EDX mapping. Figure 5.25 shows representative STEM image and EDX maps for the  $\text{NiFe}_2\text{O}_4$  nanoparticles. The existence of elements Fe, O, and Ni could be observed. Furthermore, the Fe, O, and Ni atoms are homogeneously dispersed on the surface of sample, as it is clearly seen in the STEM-EDX mapping.



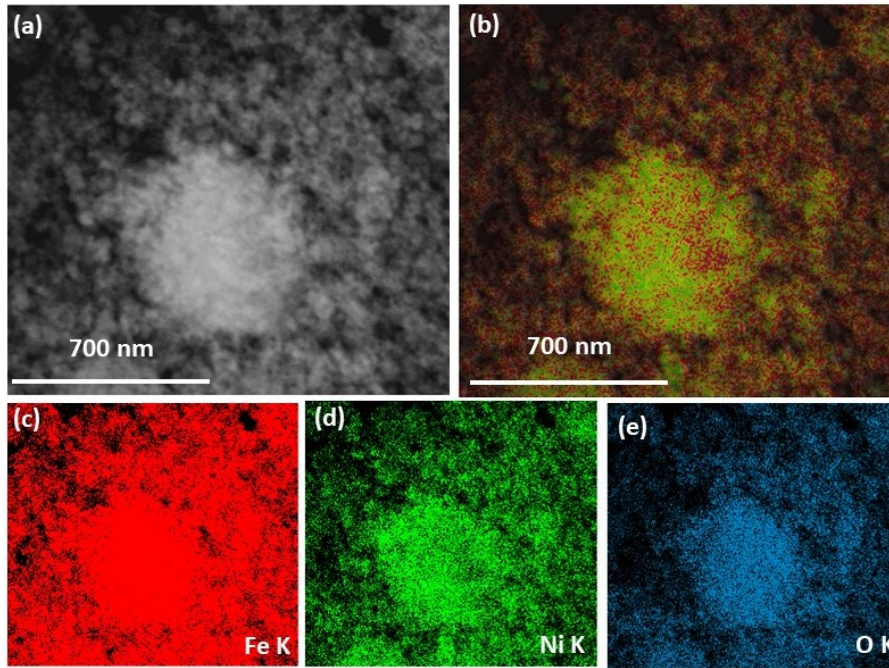


**Figure 5.25:** STEM image and EDX maps for the  $\text{NiFe}_2\text{O}_4$  nanoparticles.

**Table 5.6:** The EDX data for  $\text{NiFe}_2\text{O}_4$  nanoparticles.

Area	Element	Weight %
1	Fe	48.85
	O	28.09
	Ni	23.06
2	Fe	45.19
	O	28.38
	Ni	26.44
Average	Fe	47.02
	O	27.27
	Ni	24.75

### 5.3.3 Mössbauer Spectroscopy

The zero field  $^{57}\text{Fe}$  Mössbauer spectrum of the sample recorded at room temperature together with the fitted subspectra is reported in Figure 5.26. The main feature of the spectrum is the magnetically split sextet and a well pronounced superparamagnetic doublet. This features are due to two different particle fractions behaving ferri-magnetically and superparamagnetic-ally, respectively. It was observed from XRD and TEM measurements that all the particles have a single-domain structure and a fraction of the particles have particle size below the critical particle size ( $d_{SPM}$ ) where  $\text{NiFe}_2\text{O}_4$  becomes superparamagnetic.

The deconvolution of the magnetically split sextet shows two superimposed sextets

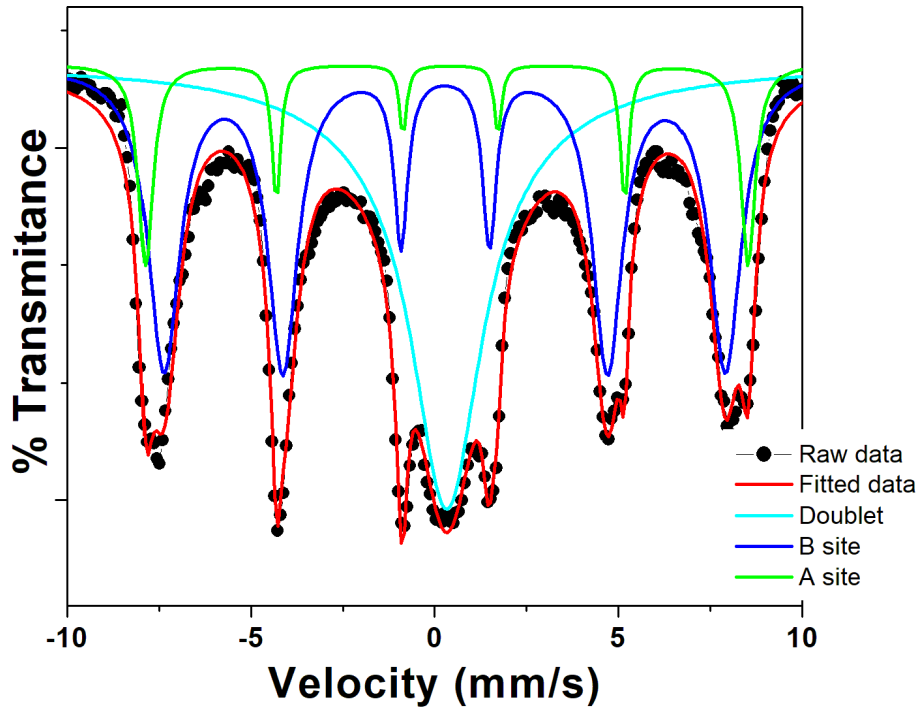


**Figure 5.26:** MS spectrum of the  $\text{NiFe}_2\text{O}_4$  nanoparticles recorded at room temperature.

due to iron cations in two different crystallographic sites (tetrahedral A-sites and octahedral B-sites) and a central doublet due to superparamagnetism. The spectrum was well fitted with two sextets having isomer shift (0.3784, 0.2761) mm/s, quadrupole splitting (-0.0511, -0.0097) mm/s, hyperfine field (50.82, 47.37) T, and a superparamagnetic doublet with isomer shift 0.3249 mm/s and quadrupole splitting 0.0045 mm/s. The isomer shifts from the two sextets and doublet indicates the presence of  $\text{Fe}^{3+}$  as expected since the structure of a well crystallized Ni-doped phase can be described as  $(\text{Fe}^{3+})^{\text{A}}[\text{Ni}^{2+}, \text{Fe}^{3+}]_2^{\text{B}}\text{O}_4$  [16], where the  $\text{Fe}^{2+}$  ions in pure  $(\text{Fe}^{3+})^{\text{A}}[\text{Fe}^{2+}, \text{Fe}^{3+}]_2^{\text{B}}\text{O}_4$  are substituted with  $\text{Ni}^{2+}$  ions. However, literature reports

suggests that the  $\text{Ni}^{2+}$  ions can be distributed over both the A-sites and B-sites [16]. The spectral area of 43.62 % for the doublet indicates that superparamagnetic behaviour will have significant contribution on the magnetic properties of the sample. Table 5.7 summarizes the Mössbauer parameters, IS, QS, and  $B_{hf}$  obtained from the fitting of the room temperature spectrum.

**Table 5.7:** Room temperature Mössbauer hyperfine parameters of the  $\text{NiFe}_2\text{O}_4$  sample.

Sites	IS (mm/s)	QS (mm/s)	$B_{hf}$ ( $\times 10^4$ Oe)	A (%)
A-sites	0.3784	- 0.0511	50.82	10.18
B-sites	0.2761	- 0.0097	47.37	46.20
Doublet	0.3249	0.0045	—	43.62

### 5.3.4 Vibrating Sample Magnetometer

To study the "blocked" and superparamagnetic state of the  $\text{NiFe}_2\text{O}_4$  nanoparticles, the sample was subjected to temperature-dependent zero-field-cooled (ZFC) and field-cooled (FC) magnetization measurements.  $M_{ZFC}$  and  $M_{FC}$  thermomagnetic curves for the sample recorded in an applied field  $H = 500$  Oe are reported in Figure 5.27. The  $M_{FC}$  curve was observed to gradually decrease with an increase in temperature. On the other hand, the  $M_{ZFC}$  curve showed a significant increase in magnetization with increasing temperature until a broad maximum or a cusp at  $\sim 228$  K, followed by a decrease in magnetization as temperature was further increased. The cusp is typical of superparamagnetic behaviour and it corresponds to the blocking temperature ( $T_B$ ) of the sample. This observation is consistent with Mössbauer study which revealed that a fraction of the particles behaved superparamagnetically.

The field dependence M vs H magnetization curves for the sample recorded at 10, 50, 100, and 300 K are reported in Figure 5.28. Similarly to the other two samples studied in this project, the Ni-doped ferrite also display magnetic properties characteristic of both ferrimagnetic and superparamagnetic state. At 300 K the particles are observed to be in the transition regime between superparamagnetic and a blocked state. This is evident by the almost "close" hysteresis loop at 300 K. As the temperature is decreased, the loops are "opening", indicating the "blocking" of these particles which were in an "unblocked" superparamagnetic state at room temperature. The observed increase in coercivity and saturation magnetization as temperature decreases indicates an increase in exchange interaction between spin moments as thermal activation energy is suppressed at lower temperatures which is attributed to superparamagnetism. This is an observation which is consistent with a lowering of the energy barrier for magnetization reversal that leads to faster relaxation by thermal fluctuations as discussed in section 2.2.4. Indeed, this finding

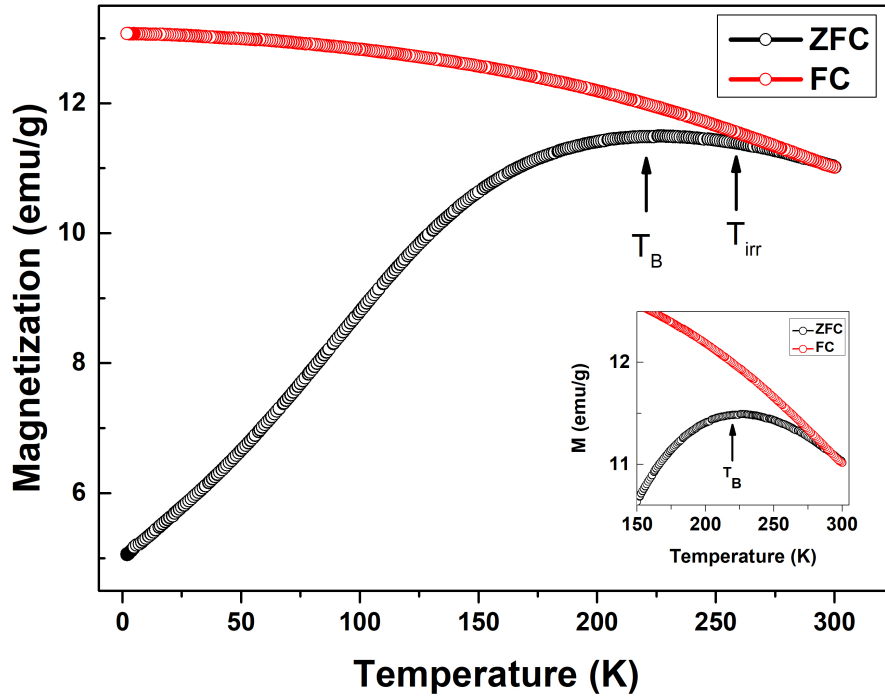


**Figure 5.27:** FC and ZFC magnetization curves as a function of temperature in an applied field ( $H$ ) for  $\text{NiFe}_2\text{O}_4$  nanoparticles.

is supported by the  $M_{ZFC}$  and  $M_{FC}$  measurements which showed the blocking and unblocking of nanoparticles around  $T_B = 228$  K.

Examination of the hysteresis loops using the SPD method revealed that all the loops achieved saturation magnetization with the maximum applied magnetic field of 20 kOe. This is shown by the overlapping of the ascending and descending curves in the plots of the derivatives  $dM/dH$  vs  $H$  for the negative fields as illustrated in Figure 5.29. At 300 K, the values of the coercivity, saturation magnetization and remanent magnetization are  $H_c = 69.59$  Oe,  $M_s = 26.32$  emu/g, and  $M_r = 2.624$  emu/g, respectively. A slight increase in saturation magnetization and a significant increase in coercivity by almost six times was observed when the temperature was reduced from 300 K to 10 K. Again this pointed out to the enhancement of magnetic anisotropy growth at low temperatures inhibiting the alignment of the moment in an applied field [135].

In the whole temperature range (10 - 300 K), low values of  $M_s$  were measured as compared to bulk values of  $M_s$  for  $\text{NiFe}_2\text{O}_4$  (50.4 emu/g) [75]. It is widely reported that the reduced  $M_s$  values in magnetic nanoparticles is caused by canted surface spins which impedes the alignment of magnetic moments along the direction of applied magnetic field [79]. It has been independently established by Mössbauer spectroscopy and VSM measurements that the sample considered in this study consists

of both ferrimagnetic and superparamagnetic particles. The smaller superparamagnetic particles are responsible for the reduction in saturation magnetization. The results from M vs H magnetic measurements for the  $\text{NiFe}_2\text{O}_4$  nanoparticles are listed in Table 5.8. The Bohr magneto ( $\mu_B$ ) for the sample was calculated with equation 5.2, where M is molecular weight of  $\text{NiFe}_2\text{O}_4$ . The magnetic parameters such as coercivity, saturation magnetization and remanent magnetization were small for the Ni-doped sample compared to the Co-doped sample because nickel ferrite being a relatively soft ferrite is known to have a low values of  $H_c$  and  $M_s$  [79].

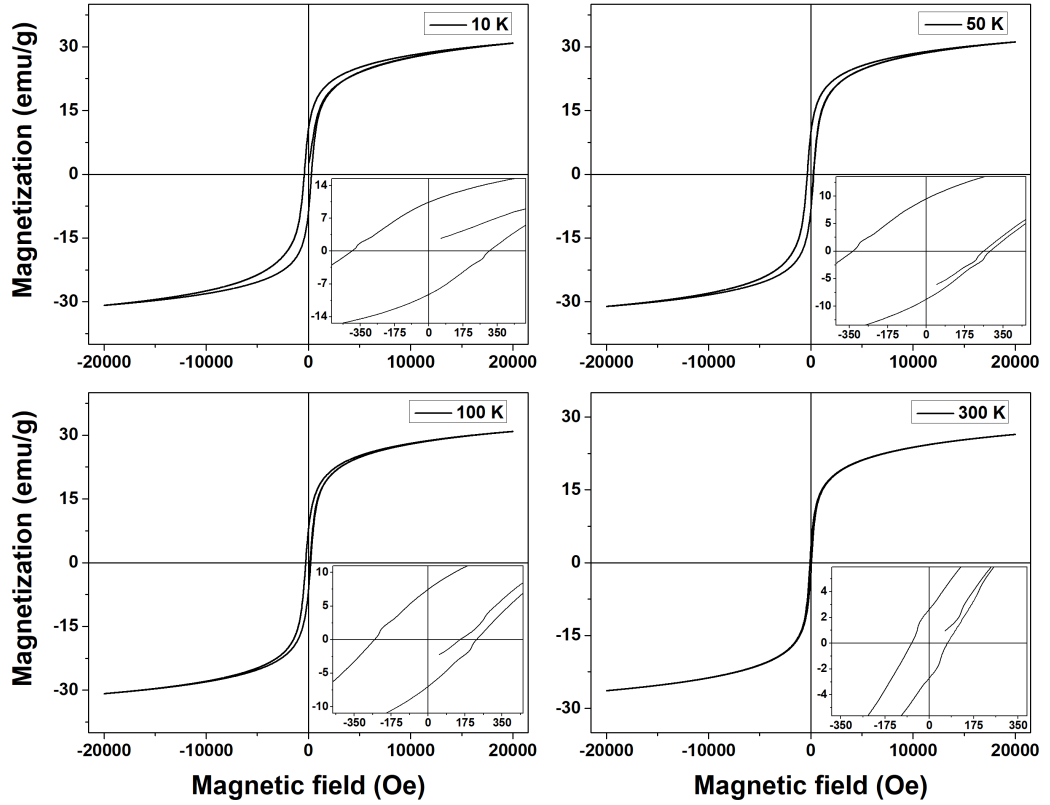


**Figure 5.28:**  $\text{NiFe}_2\text{O}_4$  hysteresis loop showing the magnetization and coercivity behaviour at low and high temperatures (10 - 300)K

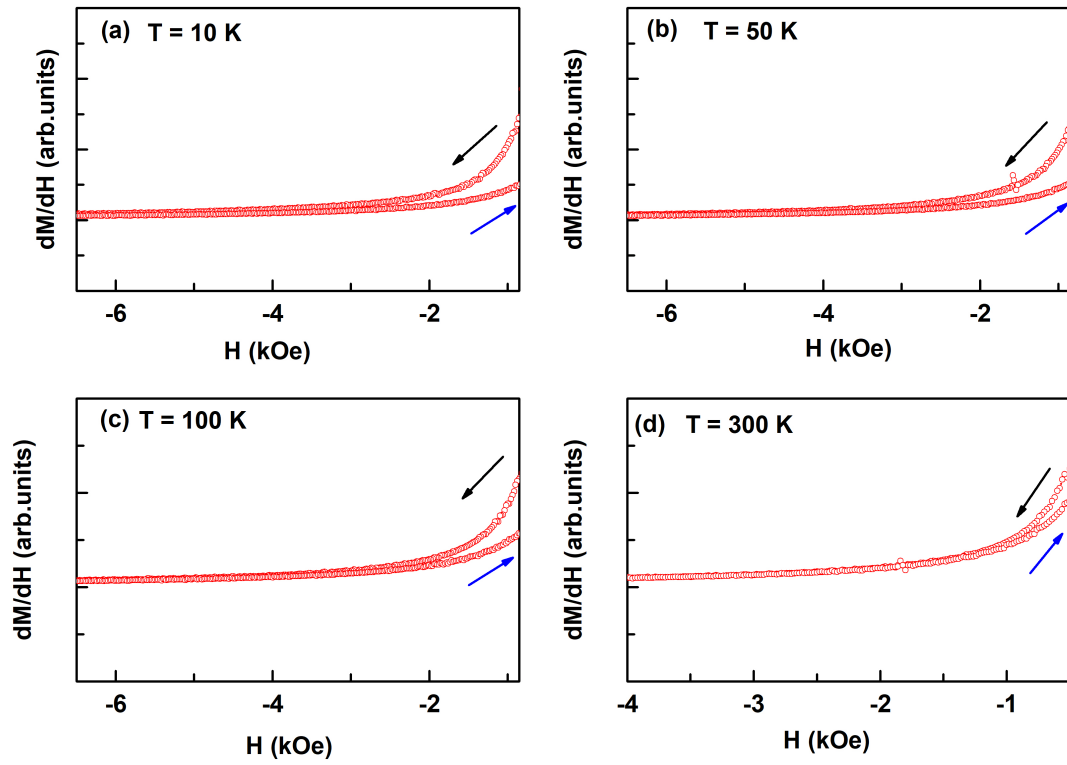


**Figure 5.29:** Derivatives of the respective descending and ascending branches for negative fields for the  $\text{NiFe}_2\text{O}_4$   $M$ - $H$  curves at 10 K - 300 K.

**Table 5.8:** The hysteresis loop data for  $\text{NiFe}_2\text{O}_4$  nanoparticles.

T (K)	$M_s$ (emu/g)	$M_r$ (emu/g)	$H_c$ (Oe)	$\mu_B$
10	30.86	10.34	391.9	1.30
50	31.06	9.382	332.1	1.30
100	30.80	7.46	253.3	1.29
300	26.32	2.624	69.59	1.10

# Chapter 6

## General Conclusion & Recommendations

This dissertation has reported work on the synthesis and characterization of ferrite nanoparticles. Three ferrite samples i.e.  $\text{Fe}_3\text{O}_4$ ,  $\text{CoFe}_2\text{O}_4$ , and  $\text{NiFe}_2\text{O}_4$  were successfully synthesized by co-precipitation method and their magnetic properties were studied. The structure, morphology, and elemental composition for the as-prepared samples were characterized by XRD, TEM, and EDX, techniques. Experimental XRD patterns for the three samples matched standard XRD patterns for stoichiometric  $\text{Fe}_3\text{O}_4$ ,  $\text{CoFe}_2\text{O}_4$ , and  $\text{NiFe}_2\text{O}_4$ , with no impurity phase observed, indicating the high purity of the synthesized nanoparticles. The particle sizes 11.7 nm, 23.6 nm, and 16.4 nm estimated from XRD for  $\text{Fe}_3\text{O}_4$ ,  $\text{CoFe}_2\text{O}_4$ , and  $\text{NiFe}_2\text{O}_4$ , respectively, was found to be well below the critical domain sizes ( $d_{SD}$ ) for all three ferrite samples considered in this work. This results confirmed the magnetic single domain structure of the nanoparticles in all three samples. In addition, the particle size histogram for the three samples showed fraction of the particles with particle size below the critical particle size ( $d_{SPM}$ ) to achieve superparamagnetism.

As revealed by TEM, all three samples were composed of uniform nanoparticles of spherical morphology with broad size distribution. The nanocrystalline nature of the samples was further revealed by the presence of lattice fringes on the HR-TEM images of the nanoparticles. For the Co- and Ni-substituted samples, the observed lattice fringes had an interplanar spacing of 0.473 nm and 0.248 nm corresponding to the (111) and (311) reflection planes, respectively. EDX spectrum and EDX maps revealed the presence and homogeneous distribution of the main elements Fe, O, Co, and Ni for the substituted samples. The stoichiometry of the substituted ferrites was further confirmed by quantitative EDX results where the experimentally observed wt% of these samples were closely equal to the values of the theoretical calculated wt% i.e. Fe = 46.35 wt%, O = 26.79 wt%, and Co = 26.87 wt%, and Fe = 47.02 wt%, O = 27.27 wt%, and Ni = 24.75 wt%, for  $\text{CoFe}_2\text{O}_4$ , and  $\text{NiFe}_2\text{O}_4$ , respectively.

Room temperature 57-Fe Mössbauer spectroscopy for the  $\text{Fe}_3\text{O}_4$  sample showed a ferromagnetically ordered spectrum which was a superposition of two sextets attributed to the A-sites and B-sites in magnetite. For the  $\text{CoFe}_2\text{O}_4$  and  $\text{NiFe}_2\text{O}_4$  samples, a well-defined Zeeman pattern was also observed. Both spectra were deconvoluted into

two sextets representing the tetrahedrally coordinated Fe cations (A-sites) and octahedrally coordinated Fe cations (B-sites), and a central paramagnetic doublet due to superparamagnetism. These results suggested that the two substituted samples had a fraction of particles behaving ferrimagnetically and another fraction exhibiting superparamagnetic behaviour. It is noteworthy mentioning that for the substituted samples, the isomer shifts for the A-sites were approximately equal to the isomer shifts for the B-sites as a result of substituting the  $\text{Fe}^{2+}$  ions with  $\text{Co}^{2+}$  and  $\text{Ni}^{2+}$  ions in the B-sites, for the Co- and Ni-substituted samples, respectively. Mössbauer spectroscopy is element specific, in the case of 57-Fe Mössbauer spectroscopy, it was only "seeing"  $\text{Fe}^{3+}$  in both the A- and B-sites for the substituted samples —hence the same isomer shift values for the two different crystallographic sites.

Temperature dependence zero-field-cooled (ZFC) and field-cooled (FC) magnetization measurements were recorded in an applied field  $H = 500$  Oe to study the transition from ferrimagnetic to superparamagnetic state above the blocking temperature  $T_B$ . The coexistence of ferrimagnetic and superparamagnetic behaviour were observed in all three samples.  $M_{ZFC}$  curves for all three samples exhibited a maximum (cusp), typical of superparamagnetic behaviour. The cusp correspond to the temperature  $T_B$ , this is a transition temperature between ferrimagnetic and superparamagnetic state. Above this temperature the nanoparticles becomes "unblocked" in a superparamagnetic state and below it they become "blocked" in ferrimagnetic state. The blocking temperatures for the three samples were approximately around 225 K, 300 K, and 228 K, for the  $\text{Fe}_3\text{O}_4$ ,  $\text{CoFe}_2\text{O}_4$ , and  $\text{NiFe}_2\text{O}_4$ , respectively. For the Co-substituted sample, the blocking temperature  $T_B$  coincided with the bifurcation temperature  $T_{irr}$  (the blocking temperature of the larger particles in the sample). And for the pure magnetite and Ni-substituted samples,  $T_B$  and  $T_{irr}$  did not coincides with  $T_{irr}$  close to 300 K for the two samples.

The field dependence of the magnetization was investigated at temperatures 10, 50, 100, and 300 K. The M-H curves for the  $\text{Fe}_3\text{O}_4$ ,  $\text{NiFe}_2\text{O}_4$  nanoparticles revealed the soft magnetic nature of these samples. Symmetrically S-shaped hysteresis loops were observed for the two samples. At 300 K both samples show almost "closed" loop which did not display significant  $H_c$  and  $M_r$  values, an indication of the presence of superparamagnetic behaviour in these samples. However, the non-zero coercive field and remanence magnetization at 300 K also shows that a fraction of these nanoparticles were in an ordered ferrimagnetic state. Further evidence of the superparamagnetic behaviour was obtained from the "opening" of the hysteresis loops when temperature was reduced from 300 K to 10 K, sharp increases in coercivity from  $\sim 70$  Oe to  $\sim 392$  Oe and  $\sim 36$  Oe to  $\sim 102$  Oe were recorded for the  $\text{Fe}_3\text{O}_4$  and  $\text{NiFe}_2\text{O}_4$ , respectively. Furthermore, the influence of the  $\text{Ni}^{2+}$  substitution resulted in a sharp increase in coercivity of the  $\text{NiFe}_2\text{O}_4$  sample compared to the pure  $\text{Fe}_3\text{O}_4$  phase, showing the high anisotropic character of  $\text{Ni}^{2+}$  compared to  $\text{Fe}^{2+}$ .

In contrast, M-H curves for the  $\text{CoFe}_2\text{O}_4$  sample displayed much higher coercivity compared to the other two samples. Indeed, Co-substituted ferrite is known as a hard magnetic material because  $\text{Co}^{2+}$  is highly anisotropic. At 300 K, the sample



showed the S-shaped hysteric loop with a relatively small coercivity of 116 Oe and remanence magnetization 4 emu/g. Upon cooling, wasp-waist hysteresis loops were observed and a substantial increase in coercivity up to  $\sim 2.7$  kOe was recorded. The observation of a typical soft magnetic loop at room temperature and hard magnetic loops at low temperatures (100 - 10 K) shows the significant contribution of the superparamagnetic behaviour in the  $\text{CoFe}_2\text{O}_4$  sample. Saturation magnetization increased from 37 to 51 emu/g when temperature was reduced from 300 to 10 K. The observed  $M_s$  values are lower than the bulk  $M_s$  value of 80 emu/g for  $\text{CoFe}_2\text{O}_4$ . An effect attributed to surface disorder, the disordered spins present at the surface of the particles prevents core spin from aligning to the field direction.

The results from this work clearly demonstrate that the magnetic properties of  $\text{Fe}_3\text{O}_4$  can be tuned by substituting the  $\text{Fe}^{2+}$  ions with other divalent ions such as  $\text{Co}^{2+}$  and  $\text{Ni}^{2+}$ . Substituting with high anisotropic cobalt results in a hard magnetic material with large coercivity, while substitution with nickel results in a "soft" magnetic material. Different applications requires nanomaterials with specific magnetic properties e.g. for application such as magnetic hyperthermia for cancer treatment nanoparticles must have high saturation magnetization and low coercivity. On the other hand, high coercivity and moderate magnetization is a requirement for magnetic recording applications and for such applications  $\text{CoFe}_2\text{O}_4$  will be an obvious choice. These specific requirements can be achieved by modifying the magnetic properties of  $\text{Fe}_3\text{O}_4$  by inclusion of  $\text{Co}^{2+}$  and  $\text{Ni}^{2+}$  ions and controlling the particle size and cationic distributions.

All the as-prepared samples in this work showed some degree of particle agglomeration. This is often an undesirable feature and it can be minimised by using a surfactant. The experimental conditions and the amount of the surfactant used should be optimised to produce mono-dispersed nanoparticles.

# Bibliography

- 1 Narendra Kulkarni and Uday Muddapur. Biosynthesis of metal nanoparticles: a review. *Journal of Nanotechnology*, 2014, 2014.
- 2 Daliya S Mathew and Ruey-Shin Juang. An overview of the structure and magnetism of spinel ferrite nanoparticles and their synthesis in microemulsions. *Chemical engineering journal*, 129(1-3):51–65, 2007.
- 3 TP Raming, Aloysius JA Winnubst, 1C M van Kats, and AP Philipse. The synthesis and magnetic properties of nanosized hematite ( $\alpha$ -Fe<sub>2</sub>O<sub>3</sub>) particles. *Journal of Colloid and Interface Science*, 249(2):346–350, 2002.
- 4 Mahnaz Amiri, Masoud Salavati-Niasari, and Ahmad Akbari. Magnetic nanocarriers: evolution of spinel ferrites for medical applications. *Advances in colloid and interface science*, 265:29–44, 2019.
- 5 Safia Anjum, Rabia Tufail, Khalid Rashid, Rehana Zia, and S Riaz. Effect of cobalt doping on crystallinity, stability, magnetic and optical properties of magnetic iron oxide nano-particles. *Journal of Magnetism and Magnetic Materials*, 432:198–207, 2017.
- 6 Felisa Reyes-Ortega, Ángel V Delgado, and Guillermo R Iglesias. Modulation of the magnetic hyperthermia response using different superparamagnetic iron oxide nanoparticle morphologies. *Nanomaterials*, 11(3):627, 2021.
- 7 Burghard Thiesen and Andreas Jordan. Clinical applications of magnetic nanoparticles for hyperthermia. *International journal of hyperthermia*, 24(6):467–474, 2008.
- 8 Amyn S Teja and Pei-Yoong Koh. Synthesis, properties, and applications of magnetic iron oxide nanoparticles. *Progress in crystal growth and characterization of materials*, 55(1-2):22–45, 2009.
- 9 Z. Szotek, W. M. Temmerman, D. Ködderitzsch, A. Svane, L. Petit, and H. Winter. Electronic structures of normal and inverse spinel ferrites from first principles. *Phys. Rev. B*, 74:174431, Nov 2006. doi: 10.1103/PhysRevB.74.174431. URL <https://link.aps.org/doi/10.1103/PhysRevB.74.174431>.
- 10 YH Hou, YJ Zhao, ZW Liu, HY Yu, XC Zhong, WQ Qiu, DC Zeng, and LS Wen. Structural, electronic and magnetic properties of partially inverse spinel CoFe<sub>2</sub>O<sub>4</sub>: a first-principles study. *Journal of Physics D: Applied Physics*, 43(44):445003, 2010.

- 11 K Bouferrache, Z Charifi, H Baaziz, AM Alsaad, and Ahmad Telfah. Electronic structure, magnetic and optic properties of spinel compound  $\text{NiFe}_2\text{O}_4$ . *Semiconductor Science and Technology*, 35(9):095013, 2020.
- 12 Z Szotek, WM Temmerman, D Ködderitzsch, A Svane, L Petit, and H Winter. Electronic structures of normal and inverse spinel ferrites from first principles. *Physical Review B*, 74(17):174431, 2006.
- 13 Y Cedeño-Mattei and O Perales-Pérez. Synthesis of high-coercivity cobalt ferrite nanocrystals. *Microelectronics Journal*, 40(4-5):673–676, 2009.
- 14 Y Cedeño-Mattei, O Perales-Pérez, and ONC Uwakweh. Synthesis of high-coercivity non-stoichiometric cobalt ferrite nanocrystals: Structural and magnetic characterization. *Materials Chemistry and Physics*, 132(2-3):999–1006, 2012.
- 15 Sheenu Jauhar, Japinder Kaur, Ankita Goyal, and Sonal Singhal. Tuning the properties of cobalt ferrite: a road towards diverse applications. *RSC advances*, 6(100):97694–97719, 2016.
- 16 Tsvetomila Lazarova, Milena Georgieva, Dimitar Tzankov, Dimitrinka Voykova, Lyubomir Aleksandrov, Zara Cherkezova-Zheleva, and Daniela Kovacheva. Influence of the type of fuel used for the solution combustion synthesis on the structure, morphology and magnetic properties of nanosized  $\text{NiFe}_2\text{O}_4$ . *Journal of Alloys and Compounds*, 700:272–283, 2017.
- 17 Frances Hellman, Axel Hoffmann, Yaroslav Tserkovnyak, Geoffrey SD Beach, Eric E Fullerton, Chris Leighton, Allan H MacDonald, Daniel C Ralph, Dario A Arena, Hermann A Dürr, et al. Interface-induced phenomena in magnetism. *Reviews of modern physics*, 89(2):025006, 2017.
- 18 Charles Kittel. Introduction to solid state physics eighth edition. 2021.
- 19 John MD Coey. *Magnetism and magnetic materials*. Cambridge university press, 2010.
- 20 Rolf E Hummel. Magnetic phenomena and their interpretation—classical approach. In *Electronic Properties of Materials*, pages 312–337. Springer, 2001.
- 21 Gregory A Landrum and Richard Dronskowski. The orbital origins of magnetism: from atoms to molecules to ferromagnetic alloys. *Angewandte Chemie International Edition*, 39(9):1560–1585, 2000.
- 22 Malcolm H Levitt. *Spin dynamics: basics of nuclear magnetic resonance*. John Wiley & Sons, 2013.
- 23 Gareth P Hatch and Richard E Stelter. Magnetic design considerations for devices and particles used for biological high-gradient magnetic separation (hgms) systems. *Journal of magnetism and magnetic materials*, 225(1-2):262–276, 2001.

- 24 Amikam Aharoni et al. *Introduction to the Theory of Ferromagnetism*, volume 109. Clarendon Press, 2000.
- 25 Alex Goldman. *Handbook of modern ferromagnetic materials*, volume 505. Springer Science & Business Media, 2012.
- 26 Nicola A Spaldin. *Magnetic materials: fundamentals and applications*. Cambridge university press, 2010.
- 27 The Editors of Encyclopaedia Britannica. "Curie point". <https://www.britannica.com/science/Curie-point>, 2016.
- 28 Jonas De Clercq. *Modelling antiferromagnetic interfaces with MuMax3*. PhD thesis, Ghent University, 2017.
- 29 Tao Sang, Shouheng Zhang, Guoxia Zhao, Cunzhen Geng, Zhejun Jin, Weihua Zong, Derang Cao, Jie Xu, Xia Wang, Guo-Xing Miao, et al. Magnetic moment configuration: One of decisive factors to enhance the optical mode resonance in interlayer exchange coupled trilayers. *Journal of Alloys and Compounds*, 875: 159881, 2021.
- 30 KHJ Buschow and FR de Boer. The magnetically ordered state. In *Physics of Magnetism and Magnetic Materials*, pages 19–42. Springer, 2003.
- 31 l. Magnetic Properties: Types of Magnetism - Definition. <https://material-properties.org/types-of-magnetism-definition/>.
- 32 Stephen Elliott. *The physics and chemistry of solids*. Wiley, 1998.
- 33 Sōshin Chikazumi and Chad D Graham. *Physics of ferromagnetism*. Number 94. Oxford university press, 1997.
- 34 Linus Pauling. A theory of ferromagnetism. *Proceedings of the National Academy of Sciences*, 39(6):551–560, 1953.
- 35 SR Barman, S Banik, AK Shukla, C Kamal, and Aparna Chakrabarti. Martensitic transition, ferrimagnetism and fermi surface nesting in mn2niga. *EPL (Europhysics Letters)*, 80(5):57002, 2007.
- 36 Diandra L Leslie-Pelecky and Reuben D Rieke. Magnetic properties of nanostructured materials. *Chemistry of materials*, 8(8):1770–1783, 1996.
- 37 Manuel Benz. Superparamagnetism: theory and applications. *Superparamagnetism Theory Appl*, pages 1–27, 2012.
- 38 Ihab M Obaidat, Bashar Issa, and Yousef Haik. Magnetic properties of magnetic nanoparticles for efficient hyperthermia. *Nanomaterials*, 5(1):63–89, 2015.
- 39 N Sethulakshmi, Avanish Mishra, Pulickel M Ajayan, Yoshiyuki Kawazoe, Ajit K Roy, Abhishek K Singh, and Chandra Sekhar Tiwary. Magnetism in two-dimensional materials beyond graphene. *Materials today*, 27:107–122, 2019.

- 40 Takahiro Moriyama, Michinari Kamiya, Kent Oda, Kensho Tanaka, Kab-Jin Kim, and Teruo Ono. Magnetic moment orientation-dependent spin dissipation in antiferromagnets. *Physical Review Letters*, 119(26):267204, 2017.
- 41 Costica Caizer. Nanoparticle size effect on some magnetic properties. *Handbook of Nanoparticles*, page 475, 2016.
- 42 KH Jürgen Buschow. *Handbook of magnetic materials*. Elsevier, 2003.
- 43 Universidad Zaragoza; Gerardo F. Goya. Superparamagnetism, The collapse of domain walls. [https://www.unizar.es/gfgoya/index\\_files/superparamagnetism.htm](https://www.unizar.es/gfgoya/index_files/superparamagnetism.htm), 2020.
- 44 SS Yattinahalli, SB Kapatkar, NH Ayachit, and SN Mathad. Synthesis and structural characterization of nanosized nickel ferrite. *International Journal of Self-Propagating High-Temperature Synthesis*, 22(3):147–150, 2013.
- 45 Ibrahim Sharifi, Hooman Shokrollahi, and S Amiri. Ferrite-based magnetic nanofluids used in hyperthermia applications. *Journal of magnetism and magnetic materials*, 324(6):903–915, 2012.
- 46 Kishwar Khan, Sarish Rehman, Hafeez Ur Rahman, and Qasim Khan. Synthesis and application of magnetic nanoparticles. *Gonzalez Estevez JM. Nanomagnetism. One Central Press (OCP): UK*, 2014.
- 47 Bashar Issa, Ihab M Obaidat, Borhan A Albiss, and Yousef Haik. Magnetic nanoparticles: surface effects and properties related to biomedicine applications. *International journal of molecular sciences*, 14(11):21266–21305, 2013.
- 48 Yen Pin Yew, Kamyar Shameli, Mikio Miyake, Nurul Bahiyah Bt Ahmad Khairudin, Shaza Eva Bt Mohamad, Takeru Naiki, and Kar Xin Lee. Green biosynthesis of superparamagnetic magnetite  $\text{Fe}_3\text{O}_4$  nanoparticles and biomedical applications in targeted anticancer drug delivery system: A review. *Arabian Journal of Chemistry*, 13(1):2287–2308, 2020.
- 49 Yaser Hadadian, Hajar Masoomi, Ali Dinari, Chiseon Ryu, Seong Hwang, Seok-jae Kim, Beong ki Cho, Jae Young Lee, and Jungwon Yoon. From low to high saturation magnetization in magnetite nanoparticles: The crucial role of the molar ratios between the chemicals. *ACS omega*, 2022.
- 50 Evgeny A Gorbachev, Ekaterina S Kozlyakova, Lev A Trusov, Anastasia E Sleptsova, Mikhail A Zykin, and Pavel E Kazin. Design of modern magnetic materials with giant coercivity. *Russian Chemical Reviews*, 90(10):1287, 2021.
- 51 Giulia Mirabello, Jos JM Lenders, and Nico AJM Sommerdijk. Bioinspired synthesis of magnetite nanoparticles. *Chemical Society Reviews*, 45(18):5085–5106, 2016.
- 52 YY Byong and SS Kwak. Assembly of magnetite nanoparticles into spherical mesoporous aggregates with a 3-d wormhole-like porous structure. *J. Mater. Chem*, 20:8320–8328, 2010.

- 53 Martha Compeán, Facundo Ruiz, J.R. Martinez, and Alberto Herrera-Gomez. Magnetic properties of magnetite nanoparticles synthesized by forced hydrolysis. *Materials Letters - MATER LETT*, 62:4248–4250, 10 2008. doi: 10.1016/j.matlet.2008.06.053.
- 54 Heru Setyawan and W Widiyastuti. Progress in the preparation of magnetite nanoparticles through the electrochemical method. *KONA Powder and Particle Journal*, page 2019011, 2019.
- 55 Do Kyung Kim, Maria Mikhaylova, Yu Zhang, and Mamoun Muhammed. Protective coating of superparamagnetic iron oxide nanoparticles. *Chemistry of Materials*, 15(8):1617–1627, 2003.
- 56 Mahnaz Mahdavi, Mansor Bin Ahmad, Md Jelas Haron, Farideh Namvar, Behzad Nadi, Mohamad Zaki Ab Rahman, and Jamileh Amin. Synthesis, surface modification and characterisation of biocompatible magnetic iron oxide nanoparticles for biomedical applications. *Molecules*, 18(7):7533–7548, 2013.
- 57 VN Petrov and AB Ustinov. Magnetic properties of  $\text{Fe}_3\text{O}_4$  surface. *Journal of Surface Investigation. X-ray, Synchrotron and Neutron Techniques*, 4(3):395–400, 2010.
- 58 T Prabhakaran and J Hemalatha. Chemical control on the size and properties of nano  $\text{NiFe}_2\text{O}_4$  synthesized by sol–gel autocombustion method. *Ceramics International*, 40(2):3315–3324, 2014.
- 59 Li Sun, Ru Zhang, Zhenduo Wang, Lin Ju, Ensi Cao, and Yongjia Zhang. Structural, dielectric and magnetic properties of  $\text{NiFe}_2\text{O}_4$  prepared via sol–gel auto-combustion method. *Journal of Magnetism and Magnetic Materials*, 421: 65–70, 2017.
- 60 Rochelle M Cornell, Udo Schwertmann, et al. *The iron oxides: structure, properties, reactions, occurrences, and uses*, volume 664. Wiley-vch Weinheim, 2003.
- 61 Victoria Reichel, András Kovács, Monika Kumari, Éva Bereczk-Tompa, Emanuel Schneck, Patrick Diehle, Mihály Pósfai, Ann M Hirt, Martial Duchamp, Rafal E Dunin-Borkowski, et al. Single crystalline superstructured stable single domain magnetite nanoparticles. *Scientific reports*, 7(1):1–8, 2017.
- 62 HY Hah, S Gray, CE Johnson, JA Johnson, V Kolesnichenko, P Kucheryavy, and G Goloverda. Mössbauer spectroscopy of superparamagnetic  $\text{Fe}_3\text{O}_4$  nanoparticles. *Journal of Magnetism and Magnetic Materials*, 539:168382, 2021.
- 63 Julia Mürbe, Annett Rechtenbach, and Jörg Töpfer. Synthesis and physical characterization of magnetite nanoparticles for biomedical applications. *Materials Chemistry and Physics*, 110(2-3):426–433, 2008.
- 64 SP Yadav, SS Shinde, Pramod Bhatt, SS Meena, and KY Rajpure. Distribution of cations in  $\text{Co}_1\text{-xMn}_x\text{Fe}_2\text{O}_4$  using xrd, magnetization and mössbauer spectroscopy. *Journal of Alloys and Compounds*, 646:550–556, 2015.

- 65 KS Rao, GSVRK Choudary, KH Rao, and Ch Sujatha. Structural and magnetic properties of ultrafine  $\text{CoFe}_2\text{O}_4$  nanoparticles. *Procedia Materials Science*, 10:19–27, 2015.
- 66 Shusen Zhao, Dongxu Ma, and Wanqin Jin. Preparation of  $\text{CoFe}_2\text{O}_4$  nanocrystallites by solvothermal process and its catalytic activity on the thermal decomposition of ammonium perchlorate. *Journal of Nanomaterials*, 2010:28, 2010.
- 67 Alex Goldman. *Modern ferrite technology*. Springer Science & Business Media, 2006.
- 68 Qing Song and Z John Zhang. Shape control and associated magnetic properties of spinel cobalt ferrite nanocrystals. *Journal of the American Chemical Society*, 126(19):6164–6168, 2004.
- 69 Mohammed S Al Maashani, Kadhim A Khalaf, Abbasher M Gismelseed, and Imaddin A Al-Omari. The structural and magnetic properties of the nano- $\text{CoFe}_2\text{O}_4$  ferrite prepared by sol-gel auto-combustion technique. *Journal of Alloys and Compounds*, 817:152786, 2020.
- 70 Sam Jin Kim, Seung Wha Lee, and Chul Sung Kim. Mössbauer studies on exchange interactions in  $\text{CoFe}_2\text{O}_4$ . *Japanese Journal of Applied Physics*, 40(8R):4897, 2001.
- 71 Z Mahhouti, H El Moussaoui, T Mahfoud, M Hamedoun, M El Marssi, A Lahmar, A El Kenz, and A Benyoussef. Chemical synthesis and magnetic properties of monodisperse cobalt ferrite nanoparticles. *Journal of Materials Science: Materials in Electronics*, 30(16):14913–14922, 2019.
- 72 Jan Smit. Ferrites. *Philips Technical Laboratory*, pages 278–280, 1959.
- 73 K Thanigai Arul, E Manikandan, PP Murmu, J Kennedy, and MJJoA Henini. Enhanced magnetic properties of polymer-magnetic nanostructures synthesized by ultrasonication. *Journal of Alloys and Compounds*, 720:395–400, 2017.
- 74 Michael Hoppe. *Magnetic, structural, and electronic properties of  $\text{NiFe}_{1-x}\text{O}_x$  ultrathin films*. Number FZJ-2016-01885. Elektronische Eigenschaften, 2016.
- 75 K Maaz, S Karim, A Mumtaz, SK Hasanain, J Liu, and JL Duan. Synthesis and magnetic characterization of nickel ferrite nanoparticles prepared by coprecipitation route. *Journal of Magnetism and Magnetic Materials*, 321(12):1838–1842, 2009.
- 76 Sukhleen Bindra Narang and Kunal Pubby. Nickel spinel ferrites: a review. *Journal of Magnetism and Magnetic Materials*, 519:167163, 2021.
- 77 Nitish Gupta, Pranat Jain, Ravindra Rana, and Sanjay Shrivastava. Current development in synthesis and characterization of nickel ferrite nanoparticle. *Materials Today: Proceedings*, 4(2):342–349, 2017.

- 78 Sam Jin Kim, Woo Chul Kim, Chul Sung Kim, and Seung Wha Lee. Mössbauer studies of superexchange interactions in nife 2 o 4. *Journal of the Korean physical society*, 36(6):430–434, 2000.
- 79 Ramesh B Kamble, Vaibhav Varade, KP Ramesh, and V Prasad. Domain size correlated magnetic properties and electrical impedance of size dependent nickel ferrite nanoparticles. *AIP Advances*, 5(1):017119, 2015.
- 80 P Sivakumar, R Ramesh, A Ramanand, S Ponnusamy, and C Muthamizhchelvan. Synthesis and characterization of nickel ferrite magnetic nanoparticles. *Materials Research Bulletin*, 46(12):2208–2211, 2011.
- 81 Andrei A Bunaciu, Elena Gabriela UdriŞtioiu, and Hassan Y Aboul-Enein. X-ray diffraction: instrumentation and applications. *Critical reviews in analytical chemistry*, 45(4):289–299, 2015.
- 82 BRUKER. The D8 ADVANCE: A single solution for XRD, PDF and SAXS. <https://www.bruker.com/en/products-and-solutions/diffractometers-and-scattering-systems/x-ray-diffractometers/d8-advance-family/d8-advance.html>, 2022.
- 83 Helmholtz Zentrum Berlin Dr. Francisco Garcia-Moreno. Synchrotron Radiation Diffraction, XRD. [https://www.helmholtz-berlin.de/forschung/oe/ce/materialforschung/methoden/xrd\\_en.html](https://www.helmholtz-berlin.de/forschung/oe/ce/materialforschung/methoden/xrd_en.html), 2016.
- 84 Brent Fultz and James Howe. High-resolution stem and related imaging techniques. In *Transmission Electron Microscopy and Diffractometry of Materials*, pages 587–615. Springer, 2013.
- 85 Abdul Razak Bushroa, RG Rahbari, Haji Hassan Masjuki, and Muhamad Rasat Muhamad. Approximation of crystallite size and microstrain via xrd line broadening analysis in tisin thin films. *Vacuum*, 86(8):1107–1112, 2012.
- 86 K Maniammal, G Madhu, and V Biju. X-ray diffraction line profile analysis of nanostructured nickel oxide: shape factor and convolution of crystallite size and microstrain contributions. *Physica E: Low-dimensional Systems and Nanostructures*, 85:214–222, 2017.
- 87 Jyung-Dong Lin and Jenq-Gong Duh. The use of x-ray line profile analysis to investigate crystallite size and microstrain for zirconia powders. *Journal of materials science*, 32(21):5779–5790, 1997.
- 88 B David Williams and C Carter Barry. Transmission electron microscopy: A textbook for materials science, 2009.
- 89 Oxford Instruments. Inca, 2006.
- 90 Joseph I Goldstein, Dale E Newbury, Joseph R Michael, Nicholas WM Ritchie, John Henry J Scott, and David C Joy. *Scanning electron microscopy and X-ray microanalysis*. Springer, 2017.



- 91 Jana Drbohlavova, Radim Hrdy, Vojtech Adam, Rene Kizek, Oldrich Schneeweiss, and Jaromir Hubalek. Preparation and properties of various magnetic nanoparticles. *Sensors*, 9(4):2352–2362, 2009.
- 92 M Darby Dyar, David G Agresti, Martha W Schaefer, Christopher A Grant, and Elizabeth C Sklute. Mössbauer spectroscopy of earth and planetary materials. *Annu. Rev. Earth Planet. Sci.*, 34:83–125, 2006.
- 93 Gary J Long and Fernande Grandjean. *Mössbauer spectroscopy applied to magnetism and materials science*, volume 1. Springer Science & Business Media, 2013.
- 94 Richard L Cohen. *Applications of Mössbauer spectroscopy*. Academic Press, 2013.
- 95 Ruchita Shandilya, Arpit Bhargava, Neha Bunkar, Rajnarayan Tiwari, Irina Yu Goryacheva, and Pradyumna Kumar Mishra. Nanobiosensors: Point-of-care approaches for cancer diagnostics. *Biosensors and Bioelectronics*, 130:147–165, 2019.
- 96 Norman Neill Greenwood. *Mössbauer spectroscopy*. Springer Science & Business Media, 2012.
- 97 Gunther K Wertheim. *Mössbauer effect: principles and applications*. Academic Press, 2013.
- 98 Philipp Gütlich, Eckhard Bill, and Alfred X Trautwein. *Mössbauer spectroscopy and transition metal chemistry: fundamentals and applications*. Springer Science & Business Media, 2010.
- 99 Gunther K Wertheim. Mössbauer effect in chemistry and solid-state physics: Recoil-free emission and resonant scattering of nuclear gamma rays provide a new tool for the study of solids. *Science*, 144(3616):253–259, 1964.
- 100 Leopold May. *An introduction to Mössbauer spectroscopy*. Springer Science & Business Media, 2012.
- 101 Tzonka Mineva, Ivana Matanovic, Plamen Atanassov, Moulay-Tahar Sougrati, Lorenzo Stievano, Martin Clémancey, Amélie Kochem, Jean-Marc Latour, and Frédéric Jaouen. Understanding active sites in pyrolyzed fe–n–c catalysts for fuel cell cathodes by bridging density functional theory calculations and 57fe mossbauer spectroscopy. *ACS Catalysis*, 9(10):9359–9371, 2019.
- 102 BR Kirupakar, BA Vishwanath, M Padma Sree, et al. Vibrating sample magnetometer and its application in characterisation of magnetic property of the anti cancer drug magnetic microspheres. *International Journal of Pharmaceutics and Drug Analysis*, pages 227–233, 2016.
- 103 V Lopez-Dominguez, Adrián Quesada, JC Guzmán-Mínguez, L Moreno, M Lere, J Spottorno, F Giacomone, JF Fernández, Antonio Hernando, and

- MA García. A simple vibrating sample magnetometer for macroscopic samples. *Review of Scientific Instruments*, 89(3):034707, 2018.
- 104 A Niazi, P Poddar, and AK Rastogi. A precision, low-cost vibrating sample magnetometer. *CURRENT SCIENCE-BANGALORE*-, 79(1):99–109, 2000.
- 105 Fausto Fiorillo. Measurements of magnetic materials. *Metrologia*, 47(2):S114, 2010.
- 106 Kumar Srinivasan. L1(0) iron-platinum on nanocrystalline hitperm soft magnetic underlayers for perpendicular recording media. 01 2004.
- 107 K Petcharoen and AJMS Sirvat. Synthesis and characterization of magnetite nanoparticles via the chemical co-precipitation mehod. *Materials Science and Engineering: B*, 177(5):421–427, 2021.
- 108 Subramanian Nithiyanantham, Selvaraj Viviliya, Somasundaram Anandhan, and Sreepathi Mahalakshmi. Synthesis and characterization of cobalt ferrite through co-precipitation technique. *Lett Appl NanoBioScience*, 10:1871–1876, 2020.
- 109 Suresh Sagadevan, Zaira Zaman Chowhurry, and Rahman F Rafique. Preparation and characterization of nickel ferrite nanoparticles via co-precipitation method. *Materials Research*, 21, 2018.
- 110 NS Gonçalves, JA Carvalho, ZM Lima, and JM Sasaki. Size–strain study of nio nanoparticles by x-ray powder diffraction line broadening. *Materials Letters*, 72:36–38, 2012.
- 111 F Yazdani and M Edrissi. Effect of pressure on the size of magnetite nanoparticles in the coprecipitation synthesis. *Materials Science and Engineering: B*, 171(1-3):86–89, 2010.
- 112 Kittipon Sangsuriyonk, Nophawan Paradee, Kornkanok Rotjanasuworapong, and Anuvat Sirivat. Synthesis and characterization of coxfe1- xfe2o4 nanoparticles by anionic, cationic, and non-ionic surfactant templates via co-precipitation. *Scientific Reports*, 12(1):1–11, 2022.
- 113 MA Shipilin, IN Zakharova, AM Shipilin, and VI Bachurin. Mössbauer studies of magnetite nanoparticles. *Journal of Surface Investigation. X-ray, Synchrotron and Neutron Techniques*, 8(3):557–561, 2014.
- 114 Dale L Huber. Synthesis, properties, and applications of iron nanoparticles. *Small*, 1(5):482–501, 2005.
- 115 Jeremy Winsett, Aric Moilanen, Keshav Paudel, Saeed Kamali, Keying Ding, Warner Cribb, Dereje Seifu, and Suman Neupane. Quantitative determination of magnetite and maghemite in iron oxide nanoparticles using mössbauer spectroscopy. *SN Applied Sciences*, 1(12):1–8, 2019.

- 116 PA Joy, PS Anil Kumar, and SK Date. The relationship between field-cooled and zero-field-cooled susceptibilities of some ordered magnetic systems. *Journal of physics: condensed matter*, 10(48):11049, 1998.
- 117 PA Joy and SK Date. Comparison of the zero-field-cooled magnetization behavior of some ferromagnetic and ferrimagnetic systems. *Journal of magnetism and magnetic materials*, 218(2-3):229–237, 2000.
- 118 Davide Peddis, Carla Cannas, Anna Musinu, and Giorgio Piccaluga. Magnetism in nanoparticles: beyond the effect of particle size. *Chemistry–A European Journal*, 15(32):7822–7829, 2009.
- 119 D Ravi Kumar, Syed Ismail Ahmad, Ch Abraham Lincoln, and D Ravinder. Structural, optical, room-temperature and low-temperature magnetic properties of mg–zn nanoferrite ceramics. *Journal of Asian Ceramic Societies*, 7(1): 53–68, 2019.
- 120 Marin Tadic, Vladan Kusigerski, Dragana Markovic, Irena Milosevic, and Vojislav Spasojevic. High concentration of hematite nanoparticles in a silica matrix: structural and magnetic properties. *Journal of magnetism and magnetic materials*, 321(1):12–16, 2009.
- 121 Marin Tadic, Matjaz Panjan, Biljana Vucetic Tadic, Jelena Lazovic, Vesna Damjanovic, Martin Kopani, and Lazar Kopanja. Magnetic properties of hematite ( $\alpha$ -Fe<sub>2</sub>O<sub>3</sub>) nanoparticles synthesized by sol-gel synthesis method: The influence of particle size and particle size distribution. *Journal of Electrical Engineering*, 70(7):71–76, 2019.
- 122 I Nurdin, MR Johan, II Yaacob, BC Ang, and A Andriyana. Synthesis, characterisation and stability of superparamagnetic maghemite nanoparticle suspension. *Materials Research Innovations*, 18(sup6):S6–200, 2014.
- 123 A Harres, M Mikhov, V Skumryev, AMH De Andrade, JE Schmidt, and J Geshchev. Criteria for saturated magnetization loop. *Journal of Magnetism and Magnetic Materials*, 402:76–82, 2016.
- 124 Scott J Kemp, R Matthew Ferguson, Amit P Khandhar, and Kannan M Krishnan. Monodisperse magnetite nanoparticles with nearly ideal saturation magnetization. *RSC advances*, 6(81):77452–77464, 2016.
- 125 Walid M Daoush. Co-precipitation and magnetic properties of magnetite nanoparticles for potential biomedical applications. *J. Nanomed. Res.*, 5(3): 00118, 2017.
- 126 Ekaphan Swatsitang, Sumalin Phokha, Sitchai Hunpratub, Brian Usher, Atipong Bootchanont, Santi Maensiri, and Prinya Chindaprasirt. Characterization and magnetic properties of cobalt ferrite nanoparticles. *Journal of Alloys and Compounds*, 664:792–797, 2016.

- 127 Itziar Galarreta, Maite Insausti, Izaskun Gil de Muro, Idoia Ruiz de Larramendi, and Luis Lezama. Exploring reaction conditions to improve the magnetic response of cobalt-doped ferrite nanoparticles. *Nanomaterials*, 8(2):63, 2018.
- 128 John J Friel and Charles E Lyman. Tutorial review: X-ray mapping in electron-beam instruments. *Microscopy and Microanalysis*, 12(1):2–25, 2006.
- 129 AJ d’Alfonso, B Freitag, D Klenov, and LJ Allen. Atomic-resolution chemical mapping using energy-dispersive x-ray spectroscopy. *Physical Review B*, 81(10):100101, 2010.
- 130 LA Mercante, WWM Melo, M Granada, HE Troiani, WAA Macedo, JD Ardison, MGF Vaz, and MA Novak. Magnetic properties of nanoscale crystalline maghemite obtained by a new synthetic route. *Journal of Magnetism and Magnetic Materials*, 324(19):3029–3033, 2012.
- 131 Li Wang, Chaoqun Yang, Hongjun Jin, Yue Hu, Ji Li, Shichong Xu, and Haibo Li. Magnetic and mössbauer spectroscopy studies of coFe<sub>2</sub>O<sub>4</sub>/CoFe<sub>2</sub> nanocomposites. *Journal of Materials Science: Materials in Electronics*, 31(16):13469–13476, 2020.
- 132 Andrew P Roberts, Yulong Cui, and Kenneth L Verosub. Wasp-waisted hysteresis loops: Mineral magnetic characteristics and discrimination of components in mixed magnetic systems. *Journal of Geophysical Research: Solid Earth*, 100(B9):17909–17924, 1995.
- 133 Lawrence H Bennett and Edward Della Torre. Analysis of wasp-waist hysteresis loops. *Journal of applied physics*, 97(10):10E502, 2005.
- 134 G Márquez, V Sagredo, R Guillén-Guillén, G Attolini, and F Bolzoni. Calcination effects on the crystal structure and magnetic properties of CoFe<sub>2</sub>O<sub>4</sub> nanopowders synthesized by the coprecipitation method. *Revista mexicana de física*, 66(3):251–257, 2020.
- 135 K Maaz, Arif Mumtaz, SK Hasanain, and Abdullah Ceylan. Synthesis and magnetic properties of cobalt ferrite (CoFe<sub>2</sub>O<sub>4</sub>) nanoparticles prepared by wet chemical route. *Journal of magnetism and magnetic materials*, 308(2):289–295, 2007.
- 136 David J Smith. Characterization of nanomaterials using transmission electron microscopy. 2015.
- 137 Seema Joshi, Manoj Kumar, Sandeep Chhoker, Geetika Srivastava, Mukesh Jewariya, and VN Singh. Structural, magnetic, dielectric and optical properties of nickel ferrite nanoparticles synthesized by co-precipitation method. *Journal of Molecular structure*, 1076:55–62, 2014.
- 138 Marc De Graef. *Introduction to conventional transmission electron microscopy*. Cambridge university press, 2003.